
Photoemission Electron Microscopy for Nanoscale Imaging and Attosecond Control of Light-Matter Interaction at Metal Surfaces

Soo Hoon Chew



München 2017

Photoemission Electron Microscopy for Nanoscale Imaging and Attosecond Control of Light-Matter Interaction at Metal Surfaces

Soo Hoon Chew

Dissertation
an der Fakultät für Physik
der Ludwig-Maximilians-Universität
München

vorgelegt von
Soo Hoon Chew
aus Kuala Lumpur, Malaysia

München, den 12. März 2018

Erstgutachter: Prof. Dr. Ulf Kleineberg

Zweitgutachter: Prof. Dr. Jörg Schreiber

Tag der mündlichen Prüfung: 30. April 2018

*I do not know what I may seem to the world, but as to myself,
I seem to have been only like a boy playing on the sea-shore,
and diverting myself in now and then finding a smoother pebble
or a prettier shell than ordinary, whilst the great ocean of truth
lay all undiscovered before me.*

Sir Isaac Newton

Zusammenfassung

Elektronendynamik an Festkörperoberflächen, die von elektromagnetischen Feldern mit optischen Frequenzen getrieben wird, findet auf einer Längen- und Zeitskala im Bereich von Nanometern bzw. Attosekunden statt und ermöglicht eine Vielzahl wissenschaftlicher und technischer Anwendungen auf dem Gebiet der Nanooptik und Nanoplasmonik. Die direkte Visualisierung der Elektronen in Folge ihrer Wechselwirkung mit Licht, was eine ultrahohe räumlich-zeitliche Auflösung erfordert, ist ein sehr nützliches Instrument zum Verständnis dieser Dynamik und ihrer Kontrolle. In dieser Dissertation wird eine Kombination aus Photoemissionselektronenmikroskopie (PEEM) mit Femtosekundenlaserpulsen von wenigen Zyklen Dauer sowie extrem ultravioletten (XUV) Attosekundenpulsen erforscht, um ultraschnelle Elektronendynamik an Metalloberflächen und in Nanosystemen zu untersuchen. Diese Arbeit beinhaltet die Entwicklung und Implementierung neuer Messinstrumente und Methoden für PEEM-Experimente, insbesondere Detektion, Datenerfassung und Datenanalyse.

Der erste Ansatz für eine direkte, nichtinvasive Untersuchung nanoplasmonischer Felder an ortsfesten Nanostrukturen ist eine Kombination von PEEM mit Attosekunden-Streaking (Atto-PEEM). Als eine Voraussetzung für die Implementierung des Atto-PEEM-Konzepts wird eine PEEM-Abbildung von lithographisch hergestellten Goldstrukturen mittels 93 eV XUV Attosekundenpulsen aus einer 1 kHz Quelle für die Erzeugung hoher Harmonischer realisiert. Wegen Raumladungseffekten, die durch die niedrige Repetitionsrate der hohen Harmonischen zustande kommen, sowie chromatischer Aberrationen aufgrund der hohen Energiebandbreite der durch die XUV-Strahlung erzeugten Photoelektronen, ist die räumliche Auflösung auf ~ 200 nm begrenzt. Dennoch wird gezeigt, dass trotz dieser Schwierigkeiten eine mikrospektroskopische Abbildung von inneren Elektronen und Valenzelektronen mittels unserer energieaufgelöster PEEM möglich ist. Unsere wichtigste Erkenntnis ist, dass die schnellen Photoelektronen aus dem Valenzband, die die zeitliche Struktur der plasmonischen Felder auf der Attosekundenskala abtasten, nicht durch Raumladungseffekte beeinträchtigt werden. Die sich derzeit in Entwicklung befindenden Quellen für Attosekunden-XUV-Pulse mit Megahertz Repetitionsraten sind

daher vielversprechend für die experimentelle Realisierung von nanoplasmonischem Streaking mit ultrahoher räumlicher und zeitlicher Auflösung in naher Zukunft.

Zweitens wird PEEM mit einem stereographischen, auf Above-Threshold-Ionisation basierenden Einzelschuss-Phasenmessgerät verbunden, was eine Zuordnung (Tagging) der Träger-Einhüllenden-Phase (carrier-envelope phase, CEP) erlaubt und dadurch ermöglicht, die Kontrolle der Photoemission auf der Attosekenskala zu erforschen. Erste Experimente an Goldnanosphären auf einer Goldebene sowie an einer rauen Goldoberfläche mit wenige Zyklen kurzen Laserpulsen im Nah-Infraroten weisen ein CEP-Artefakt mit einer Modulationsperiode von π auf. Es wird gezeigt, dass dieses Artefakt durch eine Abhängigkeit sowohl der Photoelektronenspektren als auch der CEP-Messung von der Laserintensität hervorgerufen wird. Die bisherige CEP-Tagging-Technik wird deshalb um Intensitäts-Tagging erweitert, um dieses intensitätsabhängige Artefakt zu korrigieren. Als Resultat wird nach angemessenen Korrekturen basierend auf dem Intensitäts-Tagging eine schwache CEP-Modulation ($\sim 1\%$ Amplitude) der Photoemissionsergiebigkeit von einer unstrukturierten Wolframoberfläche mit einer Modulationsperiode von 2π (wie bei Festkörpern erwartet) im Above-Threshold-Photoemissionsregime erfolgreich nachgewiesen. Im Tunnelregime wächst die CEP-Modulation auf $\sim 7\%$ trotz aufkommender Raumladungseffekte aufgrund der starken Spitzenintensität der Laserpulse. Es werden ebenfalls Goldnanodreiecke mit dieser Technik untersucht, jedoch kann keine CEP-Modulation innerhalb der experimentellen Genauigkeit von $\sim 0.6\%$ gefunden werden. Dies stellt eine Obergrenze für eine mögliche CEP-Modulation an dieser Nanostruktur dar.

Abstract

Electron dynamics at solid surfaces unfold on the nanometer length and attosecond timescale when driven by electromagnetic fields at optical frequencies, enabling vast scientific and technological applications in the field of nano-optics and nanoplasmonics. Direct imaging of the electrons upon interaction with light is a highly desirable tool for understanding and control of the dynamics, which requires ultrahigh spatiotemporal resolution. This thesis explores the combination of photoemission electron microscopy (PEEM) with few-cycle femtosecond laser pulses and attosecond extreme ultraviolet (XUV) pulses for studying ultrafast electron dynamics from metallic surfaces and nanosystems. The work involves development and implementation of new experimental tools including detection, data acquisition and analysis techniques for PEEM measurements.

The first approach is using a combination of PEEM with attosecond streaking spectroscopy (atto-PEEM) for direct, non-invasive probing of nanoplasmonic fields from supported nanostructures. As a first step towards the implementation of the atto-PEEM concept, PEEM imaging on lithographically fabricated gold structures employing 93 eV attosecond XUV pulses from a 1 kHz high-harmonic generation (HHG) source is performed. The spatial resolution is limited to ~ 200 nm due to space charge effects when working with such a low-repetition-rate HHG source and chromatic aberrations caused by the large energy bandwidth of XUV-generated photoelectrons. Nevertheless, we show that microspectroscopic imaging of core-level and valence band electrons is achievable using our energy-resolved PEEM despite the aforementioned issues. Most importantly, we find that the fast photoelectrons from the valence band, which carry the attosecond temporal structure of the plasmonic field, are not affected by space charge effects. The currently developed megahertz-repetition-rate attosecond XUV sources are therefore expected to enable the experimental realization of nanoplasmonic streaking with ultrahigh spatiotemporal resolution in the near future.

Second, PEEM is coupled with a single-shot stereographic above-threshold ionization phase meter, which allows carrier-envelope phase (CEP) tagging for studying attosecond control of photoemission. First experiments performed on gold nanospheres on a gold plane and on a random rough gold surface using few-cycle near-

infrared pulses show a CEP artefact with a modulation period of π . The artefact is found to be caused by a laser intensity dependence of both the photoelectron spectra and the CEP measurement. Intensity tagging is therefore added to the current CEP tagging technique to correct this intensity-dependent artefact. As a result, a very weak CEP modulation ($\sim 1\%$ amplitude) of the photoemission yield from a bulk tungsten surface with a 2π modulation period (as expected from solids) is successfully detected in the above-threshold photoemission regime after applying appropriate corrections based on the intensity tagging. Entering the tunneling regime, the CEP modulation increases to $\sim 7\%$ despite the presence of space charge effects due to high laser peak intensity. We also apply this technique to investigate the CEP dependence on gold nanotriangles and find no apparent CEP modulation within an accuracy of $\sim 0.6\%$ as given by our experimental conditions, which constitutes an upper limit for a possible CEP modulation from this nanostructure.

Contents

Zusammenfassung	i
Abstract	iii
List of publications	vii
1 Introduction	1
2 Theoretical background and fundamentals	5
2.1 Ultrashort laser pulses	5
2.1.1 Few-cycle laser pulses and CEP	5
2.1.2 HHG and attosecond pulses	7
2.2 Photoemission from solids	11
2.2.1 Linear photoemission	11
2.2.2 Nonlinear photoemission	13
2.3 Plasmonics	15
2.3.1 SPPs and LSPs	16
2.3.2 Atto-PEEM concept for ultrafast plasmonics	19
3 Experimental setup	23
3.1 PEEM	23
3.1.1 ToF spectrometer	25
3.1.2 Energy calibration	28
3.1.3 Spatial and energy resolutions of the ToF-PEEM	30
3.2 Atto-PEEM	33
3.2.1 1 kHz few-cycle laser system	33
3.2.2 1 kHz HHG source	35
3.3 CEP-tagged PEEM	37
3.3.1 10 kHz few-cycle laser system	37
3.3.2 ATI phase meter	38
3.3.3 Single-shot CEP-tagged PEEM	40
3.4 Plasmonic samples	43
3.4.1 Chemical synthesis of NPOP	43
3.4.2 EBL	43

4	Towards atto-PEEM	47
4.1	XUV imaging with attosecond pulses	47
4.2	Microspectroscopic imaging	52
4.3	Space charge effects	54
5	Laser intensity effects in single-shot CEP-tagged PEEM	57
5.1	Nonlinear photoemission at nanostructures	58
5.2	Investigation of CEP artefact for NPOP and surface roughness	59
5.2.1	Apparent CEP modulation	59
5.2.2	Laser intensity dependence	63
5.3	CEP artefact simulations	65
6	Single-shot intensity-CEP-tagged PEEM	69
6.1	Experimental concept of intensity tagging	70
6.1.1	Intensity-resolved CEP retrieval	70
6.1.2	Laser intensity-correlated artefact in CEP retrieval	72
6.1.3	Intensity-bias technique for artefact correction	77
6.2	CEP dependence on bulk tungsten	79
6.2.1	Strong-field ATP	79
6.2.2	Attosecond control of photoemission with CEP	84
6.3	CEP dependence on gold nanostructures	89
7	Conclusions and outlook	95
	Bibliography	99
	Acknowledgments	117

List of publications

S. H. Chew *et al.* *Attosecond control of photoemission from metal surfaces in the multielectron regime.* In preparation (2018).

S. H. Chew *et al.* *Intensity-phase-tagged time of flight-photoemission electron microscopy for low carrier-envelope phase sensitivity.* In preparation (2018).

J. Schmidt, A. Guggenmos, S. H. Chew, A. Gliserin, M. Högner, M. F. Kling, J. Zou, C. Späth, and U. Kleineberg. *Development of a 10 kHz high harmonic source up to 140 eV photon energy for ultrafast time-, angle-, and phase-resolved photoelectron emission spectroscopy on solid targets.* [Review of Scientific Instruments](#) **88**, 083105 (2017).

H. Pan, C. Späth, A. Guggenmos, S. H. Chew, J. Schmidt, Q.-z. Zhao, and U. Kleineberg. *Low chromatic Fresnel lens for broadband attosecond XUV pulse applications.* [Optics Express](#) **24**, 16788–16798 (2016).

S. H. Chew, A. Gliserin, J. Schmidt, H. Bian, S. Nobis, F. Schertz, M. Kübel, Y.-Y. Yang, B. Loitsch, T. Stettner, J. J. Finley, C. Späth, H. Ouacha, A. M. Azzeer, and U. Kleineberg. *Laser intensity effects in carrier-envelope phase-tagged time of flight-photoemission electron microscopy.* [Applied Physics B](#) **122**, 1–10 (2016).

J. Schmidt, A. Guggenmos, S. H. Chew, A. Gliserin, and U. Kleineberg. *Carrier-envelope-phase and angle-resolved photoelectron streaking measurements on W(110).* In [Conference on Lasers and Electro-Optics](#), FW1N.1 (2016).

J. Schmidt, A. Guggenmos, M. Hofstetter, S. H. Chew, and U. Kleineberg. *Generation of circularly polarized high harmonic radiation using a transmission multilayer quarter waveplate.* [Optics Express](#) **23**, 33564–33578 (2015).

S. H. Chew, K. Pearce, C. Späth, A. Guggenmos, J. Schmidt, F. Süßmann, M. F. Kling, U. Kleineberg, E. Mårsell, C. L. Arnold, E. Lorek, P. Rudawski, C. Guo, M. Miranda, F. Ardana, et al. In *Imaging Localized Surface Plasmons by Femtosecond to Attosecond Time-Resolved Photoelectron Emission Microscopy—“ATTO-PEEM”*. [Attosecond Nanophysics](#), pp. 325–364 (Wiley-VCH Verlag GmbH & Co. KGaA, 2015).

F. Süßmann, S. L. Stebbings, S. Zharebtsov, S. H. Chew, M. I. Stockman, E. Rühl, U. Kleineberg, T. Fennel, and M. F. Kling. In *Attosecond Nanophysics. Attosecond and XUV Physics*, pp. 421–462 (Wiley-VCH Verlag GmbH & Co. KGaA, 2014).

S. H. Chew, F. Süßmann, C. Späth, A. Wirth, J. Schmidt, S. Zharebtsov, A. Guggenmos, A. Oelsner, N. Weber, J. Kapaldo, A. Gliserin, M. I. Stockman, M. F. Kling, and U. Kleineberg. *Time-of-flight-photoelectron emission microscopy on plasmonic structures using attosecond extreme ultraviolet pulses*. *Applied Physics Letters* **100**, 051904 (2012).

S. H. Chew, K. Pearce, S. Nobis, C. Späth, A. Spreen, S. Radünz, Y. Yang, J. Schmidt, and U. Kleineberg. *Spatiotemporal characterization and control of light-field nanolocalization on metallic nanostructures by nonlinear-PEEM*. In *SPIE Proceedings. Vol. 8457*, 84571C. Plasmonics: Metallic Nanostructures and Their Optical Properties X (2012).

J. Lin, N. Weber, A. Wirth, S. H. Chew, M. Escher, M. Merkel, M. F. Kling, M. I. Stockman, F. Krausz, and U. Kleineberg. *Time of flight-photoemission electron microscope for ultrahigh spatiotemporal probing of nanoplasmonic optical fields*. *Journal of Physics: Condensed Matter* **21**, 314005 (2009).

Chapter 1

Introduction

It is at the heart of all scientific research to increase humankind's knowledge about nature by understanding, ultimately, the time-dependent interactions between fundamental particles and fields, as modeled by physics and chemistry, which constitute our world and our perception of it in daily life. Throughout history, the observation of dynamics in nature deepened our insight into the most fundamental physical laws, accurately modeling the universe from the largest scope of astronomy down to the most minute of atoms and elementary particles.

Exploring processes faster than the perception of the human eye requires experimental instruments, which allow the detection and visualization of such processes. Since the famous first slow-motion movie of a galloping horse [1] using a series of optical cameras set to a short exposure time, ever-shorter timescales became accessible owing to the tremendous technological progress in various fields. Modern-day electronics allow real-time observations on timescales of few picoseconds (10^{-12} s) [2], while even shorter timescales of femtoseconds (10^{-15} s) and attoseconds (10^{-18} s) are accessible by exploiting the high bandwidth of mode-locked bursts of laser light [3–6].

Naturally, interactions on such short timescales are strongly confined in space, since the speed of light poses an upper limit on any action, e.g. ~ 300 nm for 1 fs. Depending on the energies and masses of the particles involved [7, 8], this confinement can be on the nanoscale (e.g. for electric fields, free particles or collective electronic motion) or on the molecular or atomic scale (e.g. for nuclear motion within molecules or orbital dynamics). The visualization of fundamental interactions on these ultimate timescales is almost always indirect due to this strong spatial confinement and focuses on observing other properties than the spatial arrangement. Common experimental techniques include pump-probe studies of transient macroscopic absorption [9, 10] and fluorescence [11], waveform control of photocurrents [12, 13] and

ionization dynamics [14, 15], attosecond streaking spectroscopy [16–18] or attosecond tunneling spectroscopy [19]. Although some structural information is contained within the observed quantities, access to it is indirect and requires complex modeling. So far, only a few ultrafast visualization techniques exist which support nanometer (or better) spatial resolutions and ultimate time resolutions simultaneously. Among these are ultrafast scanning near-field optical microscopy (SNOM) [20], time-resolved transmission electron microscopy (TEM) [21] and ultrafast X-ray [22, 23] or electron diffraction [24, 25], which allow direct visualization of the structural information on the nanometer (microscopy, X-ray diffraction) and sub-atomic scale (albeit in reciprocal space in the case of electron diffraction).

While SNOM can utilize the high time resolution given by the duration of state-of-the-art ultrashort laser pulses and record electric fields at the surface with nanometer resolution using a sharp tip, acquiring spatial information requires in-plane scanning and thus many pump-probe cycles, resulting in a long acquisition time. TEM on the other hand offers parallel acquisition of spatial information (i.e. an entire image at once) with superior spatial resolution down to the atomic level [26]. However, achieving ultrahigh time resolution is challenging when using electron pulses for illumination due to Coulomb interaction and dispersion, resulting in typical electron pulse durations of several 100 fs in the case of ultrafast TEM [27] or ~ 30 fs in the case of ultrafast electron diffraction [25]. The successful combination of the spatial resolution offered by an electron microscope with the superior temporal resolution of ultrashort laser pulses has led to the emerging field of time-resolved photoemission electron microscopy (PEEM) in the past decades [28–30]. Here, a pulse of light excites electron dynamics in a solid sample, which is then probed by a second light pulse through the emission of electrons from the sample via the photoelectric effect. The origin of these photoelectrons at the sample surface is precisely imaged on the nanoscale by the electron optics of the microscope and contains information about local properties of the sample, such as the work function or the electric field strength at the surface. Combining a PEEM with an image-preserving spectrometer, e.g. an imaging energy filter (IEF) or time-of-flight (ToF) detector, adds the capability of spatially-resolved photoelectron spectroscopy, revealing surface state excitations or strong-field effects with typically ~ 25 nm spatial and ~ 50 meV energy resolution [31]. This constitutes a versatile and powerful visualization instrument for the all-optical control of nanoscale electron dynamics, which is a promising contribution to the relatively young field of nano-optics. Various existing and potential scientific and technological applications for this technique include the generation and propagation dynamics of collective electron motion at surfaces [32, 33], attosecond control of nanolocalized photoemission [31, 34–36], and, ultimately,

nano-optical devices which allow switching currents at optical frequencies, or 10^4 – 10^6 times faster than present-day current-driven nanoelectronics [37].

In this work, we present two different approaches to observe and control electron dynamics on the nanometer length and attosecond timescale using PEEM. The first approach is combining the PEEM with the well-established concept of attosecond streaking spectroscopy [38, 39] using attosecond extreme ultraviolet (XUV) pulses for photoemission. This concept has proved to be challenging, as the high energy bandwidth of the XUV pulses leads to aberrations and reduced resolution of the PEEM. Furthermore, the limited repetition rate of current attosecond XUV sources (kHz range) poses a practical limit on signal flux and minimum required acquisition time. The second approach demonstrates attosecond control of photoemission utilizing the carrier-envelope phase (CEP) of a few-cycle near-infrared (NIR) laser pulse, which is the phase difference between the carrier wave and the intensity envelope of the pulse, defining the shape of the pulse’s electric field. It has been shown that for a few-cycle pulse different shapes of the electric field (due to different CEPs) lead to a modulation of photoemission yield and kinetic energy from metal nanotips [12, 40]. This constitutes attosecond control, since a small change in CEP, which shifts the temporal shape of the pulse by a small fraction of an optical cycle (~ 2.2 fs at our wavelength), is sufficient to detect a modulation of the photoemission. Here, we present a CEP tagging technique in combination with energy-resolved PEEM in order to record the CEP for every pulse of a few-cycle laser source, which has not been CEP-stabilized. After additional correction for random intensity fluctuations of the laser, we are able to demonstrate CEP control of photoemission from a bulk tungsten surface measured by PEEM. A CEP-dependent modulation of the photoemission spectrum as low as $\sim 1\%$ can be detected with this instrument within ~ 30 min of measurement time. This thesis is structured as follows: chapter 2 provides some basic theoretical background for the ultrashort laser pulses used here, the photoemission processes and the surface plasmons at metal surfaces. Chapter 3 presents the experimental details, including the energy-resolved PEEM instrument, the different laser sources used in this work, the CEP tagging technique, as well as the fabrication methods of the plasmonic nanostructure samples used in these studies. In chapter 4, the results of some preliminary investigations of the attosecond PEEM approach are shown, in particular nanoscale imaging and spectroscopy using attosecond XUV pulses (without streaking yet) and the influence of space charge effects therein. Chapter 5 introduces the CEP tagging technique for PEEM and first applications on gold nanostructures. Here, a laser-intensity-related artefact is discovered and investigated, which prevents detecting an actual CEP dependence with small modulation depth. A refinement of the CEP tagging technique is presented in chapter 6 by adding laser intensity tagging as a remedy for the artefact discovered

before. The additionally intensity-resolved measurement substantially increases the CEP sensitivity of the instrument, allowing to detect small CEP modulation depths between 1 % and 7 % from a bulk tungsten surface with PEEM as a proof-of-principle at illumination intensities within the above-threshold photoemission (ATP) regime and the tunneling regime. Furthermore, a preliminary application of this technique on gold nanostructures is shown. Finally, the results are summarized in chapter 7 and an outlook is given.

Theoretical background and fundamentals

This chapter aims to provide a comprehensive overview of the theory and fundamentals related to the work presented here. First, an introduction on few-cycle laser pulses, their generation and use in high-harmonic generation (HHG) experiments is given. Next, linear and nonlinear photoemission from solids and their mechanisms are described. A brief review on surface plasmons is presented and finally the atto-PEEM concept and its current status is discussed.

2.1 Ultrashort laser pulses

Since the first demonstration of a mode-locked helium-neon laser [41], modern laser development has constantly pushed the limits of temporal resolution, from the picosecond to the femtosecond timescale. Up to now, XUV pulses generated by high harmonic radiation constitute the shortest bursts of light with durations of 80 as [5] and below [6, 42]. Concentrating light into extremely short pulses not only allows time-resolved studies with ultra-high temporal resolutions but also enables the generation of remarkably high peak intensities, facilitating nonlinear effects. Furthermore, unprecedented strong-field (or highly nonlinear) regimes can now be reached at metallic surfaces with the assistance of field enhancement facilitated by controlled plasmonic nanostructures [12, 40, 43–45] in combination with ultrashort laser excitation.

2.1.1 Few-cycle laser pulses and CEP

Ti:sapphire amplifiers in combination with a pulse compressor system based on nonlinear spectral broadening (e.g. in a fiber) and enhanced dispersion control are able to provide few-cycle pulses in the low millijoule range at kilohertz repetition rates [46,

47] and are some of the most prominent ultrafast sources to date. Other available few-cycle pulsed laser sources include high-repetition-rate mode-locked Ti:sapphire oscillators [48] and, more recently, hundred-kilohertz optical parametric chirped-pulse amplification systems [4, 49].

Basically, a few-cycle laser pulse is composed of a coherent superposition of many monochromatic waves at different optical frequencies, which are multiples (harmonics) of the laser cavity's fundamental repetition rate, and appropriate relative phases. The pulse may contain less than two optical field cycles, thus the electric field amplitude considerably changes within one optical cycle, constituting the breakdown of the slowly varying envelope approximation valid for multi-cycle pulses. Hence, the phase of the electric field carrier with respect to its envelope (referred to as CEP) starts to play an important role in light-matter interactions and strongly affects any nonlinear optical processes, which depend on the instantaneous field strength rather than on the intensity. CEP effects have already been demonstrated on gases [14, 38, 39, 50, 51], solids [12, 13, 17, 37, 40] and plasmas [52], providing a basic insight into light-matter interactions and revealing its enormous potential to precisely manipulate and control ultrafast electron dynamics. The time-varying few-cycle laser field $\mathbf{E}(t)$ can be described as a classical electromagnetic wave using the following mathematical representation:

$$\mathbf{E}(t) = \mathbf{E}_0 \cos(\omega t + \varphi) f(t). \quad (2.1)$$

Here, \mathbf{E}_0 is the electric field amplitude, ω the carrier frequency, φ the CEP and $f(t)$ an envelope function¹. The CEP describes the phase (and therefore temporal) offset between the carrier wave maximum and the pulse envelope maximum, thus defining the shape of the electric field of each pulse. Fig. 2.1 depicts an illustration of different CEPs for a few-cycle pulse of 4 fs full width at half maximum (FWHM) duration at 730 nm. In principle, two extreme cases for the pulse shape are found: the cosine-like waveform is symmetrical about the center of the pulse and has $\varphi = 0$ or π while the sine-like waveform is anti-symmetrical and has $\varphi = -\pi/2$ or $\pi/2$. Note that a few-cycle pulse requires an octave-spanning spectrum and a flat spectral phase, i.e. a phase which is constant or has a linear dependence on the frequency.

As the CEP of an ultrashort wavepacket from a laser generally experiences random fluctuations from shot to shot due to optical nonlinearity in the laser cavity [53, 54], various methods to stabilize it have been devised [53, 55–59] to ensure no phase slip between the pulses. Besides actively stabilizing the CEP to a fixed value, one can also measure it on a single-shot basis via a phase tagging technique simultaneously

¹For a transform-limited Gaussian pulse with a FWHM duration τ of its respective intensity envelope, $f(t) = \exp(-2 \ln 2 t^2 / \tau^2)$.

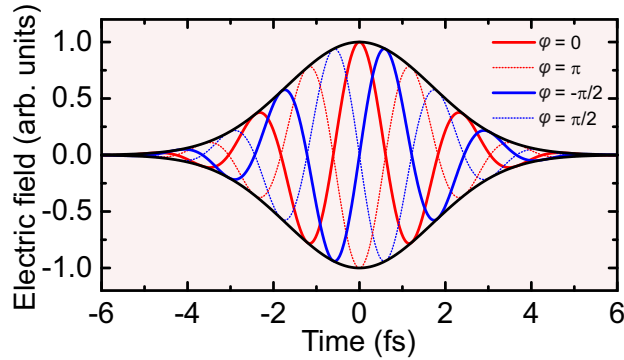


Figure 2.1: Illustration of a few-cycle laser field in the time domain with a central wavelength of 730 nm and a pulse duration of 4 fs FWHM. The pulse envelope is denoted by the black line. The electric field oscillations are plotted for four different CEPs (cosine-like waveform: $\varphi = 0$, $-\cosine$ -like waveform: $\varphi = \pi$, sine-like waveform: $\varphi = -\pi/2$ and $-\text{sine}$ -like waveform: $\varphi = \pi/2$).

with the experimental data acquisition. The latter technique (see subsections 3.3.2 and 3.3.3) is employed in this work as we aim to study CEP-dependent processes from metallic surfaces and nanostructures systematically.

Since the spectral phase of a few-cycle laser pulse changes nonlinearly when propagating through a dispersive medium, e.g. glass and air, it is crucial to carefully compensate for any introduced positive dispersion to maintain a Fourier-limited pulse. Generally, negatively chirped mirror sets [60] (negative dispersion) in combination with a pair of glass wedges (positive dispersion) are used to effectively control the second-order dispersion or linear chirp and thus correct for broadening of the pulse duration. In addition, third-order or higher-order dispersion, which can cause a significant pulse shape distortion besides temporal broadening, can only be removed by tailor-made dispersive optical elements, such as dispersive filters [61].

2.1.2 HHG and attosecond pulses

HHG in the XUV and X-ray regime, an up-conversion process to large integer multiples of the fundamental laser frequency, can be achieved by intense laser pulses via a highly nonlinear interaction with matter, particularly noble gases. In fact, attosecond science has emerged since the first observation of HHG in gases in the late 1980s [62, 63]. The three-step (“simple man”) model proposed by P. B. Corkum [64] provides a basic understanding of HHG by a single atom in a semiclassical picture and is shown schematically in fig. 2.2 (a). In the first step, a linearly polarized laser field with a strength comparable to that of the binding potential ionizes the atom via tunneling through the potential barrier by substantially reducing the binding potential in one direction at that instant (labeled as 1). The tunneled electron is

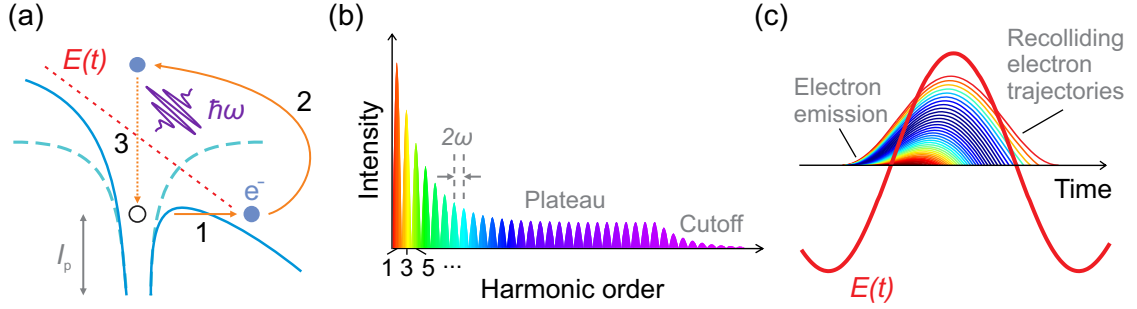


Figure 2.2: Schematic illustration of the HHG process. (a) Semiclassical three-step model for explaining the principle of HHG. See text for details. (b) Schematic photon energy spectrum of HHG from a macroscopic volume of gas atoms with distinct regions (low-order harmonics, plateau and cutoff). (c) Color-coded electron trajectories for different emission times. The dark blue and dark red trajectories correspond to the highest and lowest return energies, respectively.

now set free to the continuum and is immediately accelerated by the laser field away from the parent ion (labeled as 2). As the field reverses its direction in the next quarter of the optical cycle, the electron is driven backward to the atomic core. Upon returning, the electron recombines with its parent ion (with a low probability) and emits a highly energetic photon as a result of energy gain during the round trip in the laser field in addition to the ionization potential of the atom (labeled as 3). Consequently, the maximum photon energy emitted in the HHG process can easily lie in the XUV regime and is defined by [64–66]

$$E_{\text{cutoff}} = \hbar\omega_{\text{max}} = I_p + 3.17U_p, \quad (2.2)$$

where \hbar is the reduced Planck's constant, ω the carrier frequency, I_p the ionization potential of the atom and U_p the ponderomotive potential, i.e. the cycle-averaged quiver energy gained by a free electron in the laser field. Here, $U_p = e^2 E_0^2 / 4m\omega^2$, e being the electron charge, E_0 the laser electric field amplitude and m the electron mass. The highest kinetic energy is obtained when an electron acquires its highest return energy in the case where the atom is ionized at a phase $\omega t = 17^\circ$ [64] after the field crest rather than at the crest. Typically, HHG is generated by Ti:sapphire NIR lasers with a central wavelength around 750 nm, as also in our case. By focusing the laser pulses of such central wavelength to peak intensities of $\sim 5 \cdot 10^{14} \text{ W/cm}^2$, this yields $U_p \approx 26.3 \text{ eV}$. Hence, the cutoff energy E_{cutoff} of HHG under these conditions is $\sim 105 \text{ eV}$ when a neon gas target ($I_p = 21.6 \text{ eV}$) is used, as given by eqn 2.2.

HHG can also be described successfully by a quantum mechanical treatment in which the wave function of the electron is composed of a bound part ψ_g in the ground state and a continuum (unbound) part ψ_c in the ionization state [67, 68]. As the electron recollides with its parent ion, the unbound part ψ_c of its electronic

wave function, having a fast oscillating phase, can interfere with its bound part ψ_g . Such interference results in extremely fast oscillations of the electron density, thus leading to the generation of high harmonics.

In practice, the high harmonics are produced from a macroscopic volume of gas atoms, therefore phase matching between the fundamental laser and its harmonics must be provided in order to achieve efficient HHG from different atoms. This can be accomplished by a proper adjustment of the gas density (gas pressure), interaction length and focusing geometry in the experiments. Ultimately, a low high harmonic conversion efficiency in the range of $10^{-6} - 10^{-5}$ [69, 70] is obtained mainly due to a small recombination probability [71, 72] and absorption of XUV photons by the surrounding gas atoms [69, 70, 73, 74]. Nonetheless, the XUV photon flux generated is still very useful for many spectroscopic applications and is typically on the order of $10^5 - 10^8$ photons per pulse [35, 73–76]. Fig. 2.2 (b) shows a schematic representation of a typical HHG spectrum from a macroscopic gas target, which consists of discrete harmonics with a separation of 2ω . Note that only odd-numbered harmonics are generated because of the inversion symmetry of the gas target. While the intensities of the low-order harmonics decrease drastically with increasing harmonic number, the higher-order harmonics form a plateau with almost constant efficiency. The highest harmonics in the spectrum are characterized by a rapid drop of intensities again, which is called the cutoff region.

Since the recombination process takes place within every half laser cycle in the time domain, a train of subfemtosecond XUV bursts which are significantly shorter in duration than the fundamental laser are emitted. This strong temporal confinement is crucial for generating attosecond light pulses, and to date HHG constitutes the only available attosecond light source in practice. Depending on its emission time in the process of ionization, the electron in the continuum can recollide on different trajectories which results in different return energies, as shown by the color change in fig. 2.2 (c). There are two possible trajectories which result in the same kinetic energy upon recombination, referred to as the short and long trajectories. Furthermore, the short (long) trajectory produces a pulse with positive (negative) chirp [77]. The intrinsic chirp of the attosecond pulses limits the achievable shortest pulse duration and strongest harmonic yield. However, this can be compensated by filtering out the cutoff spectral region or using chirped multilayer mirrors [78].

The emergence of few-cycle laser pulses has enabled the generation of isolated attosecond pulses by choosing the appropriate CEP value in combination with amplitude gating [5]. As seen in fig. 2.3, a single isolated attosecond pulse can be created by spectrally filtering the cutoff region of the XUV spectrum generated by a cosine-like few-cycle NIR pulse with $\varphi = 0$ [5]. This is because the highest energetic photons are only emitted during a single electron recollision event which is completely localized

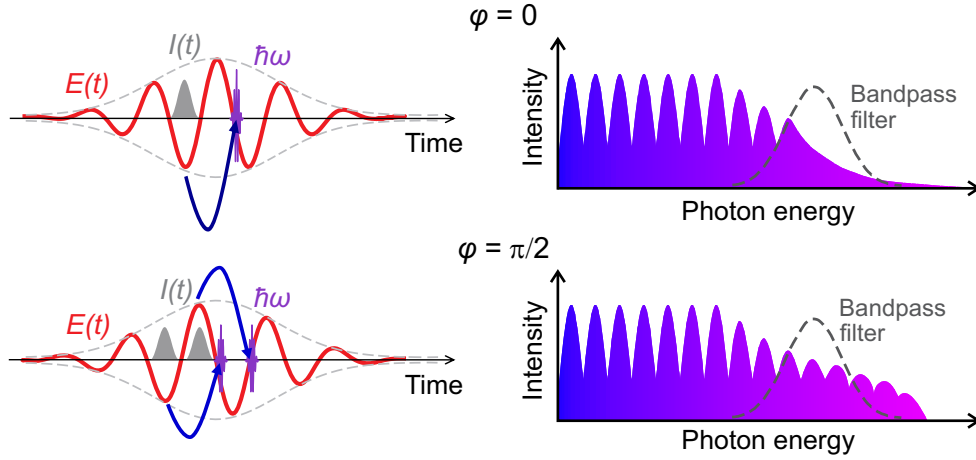


Figure 2.3: Schematic diagrams of the CEP dependence of the XUV emission in the HHG process. For a cosine-like waveform with CEP $\varphi = 0$, the highest recollision energy is obtained by the electron upon returning to its vicinity of the parent ion. The electron trajectory in this case is marked in dark blue. Such a waveform leads to a continuum in the cutoff region and a single isolated attosecond pulse can be extracted from the residual harmonics using a suitable spectral bandpass filter. In contrast, the filtered cutoff emission generated by a sine-like waveform with $\varphi = \pi/2$ creates two attosecond XUV pulses. The electron trajectories are marked in blue indicating a smaller return energy compared to the case of $\varphi = 0$ (see fig. 2.2(c)). Note that the sine-like waveform introduces a quasiperiodic spectral modulation in the cutoff region. The gray areas illustrate the time dependence of the ionization rate $I(t)$.

in time. On the other hand, a double attosecond pulse is obtained from the spectrally filtered harmonic cutoff generated by a sine-like few-cycle pulse with $\varphi = \pi/2$. This can be easily understood by the fact that the highest return energy can be acquired from two subsequent half-cycles of the laser field in the case of a sine-like pulse as it exhibits two field extrema with equal strength, and therefore two electron recollision events contribute to the cutoff energy. Other schemes [79, 80] have been developed to obtain isolated attosecond pulses including the promising double optical gating method [6, 81] that utilizes the high dependence of the HHG process on the fundamental laser's ellipticity and two-color fields. This method poses less stringent demands on the driving laser as it has been demonstrated that even 9 fs long NIR laser pulses could be used for obtaining isolated attosecond pulses [81]. Isolated attosecond pulses are essentially crucial for nonlinear attosecond experiments as well as for pump-probe spectroscopy [78].

2.2 Photoemission from solids

A relevant theoretical background of various photoemission processes is introduced here, which is useful for understanding the experimental methods presented in this work. The basics of photoemission and its application in a PEEM for the investigation of plasmonics and strong-field studies are considered.

2.2.1 Linear photoemission

The photoelectric effect was first discovered by H. Hertz in 1887 when he was experimenting on the efficiency of a spark-gap generator using ultraviolet (UV) light illumination [82]. However, a quantitative explanation for the mechanism of the photoelectric effect was only brilliantly given by A. Einstein via the quantization of light in 1905 [83]. The photoemission process described by A. Einstein is formulated as

$$E_{\text{kin}} = \hbar\omega - \phi - E_{\text{B}}. \quad (2.3)$$

An electron is coerced to leave the surface of a solid after acquiring a kinetic energy E_{kin} by absorbing a photon with an energy $\hbar\omega$ (here \hbar is the reduced Planck's constant and ω is the frequency of light). This only takes place if the photon energy exceeds the work function ϕ and the binding energy E_{B} of the material. Usually, $E_{\text{B}} = 0$ if the electron is emitted from the Fermi level to the vacuum level near surfaces. Eqn 2.3 refers to a direct process of one-photon photoemission without involving nonlinear effects. Generally, the work function of most solid materials is in the range of 4 eV – 6 eV [84]. With UV light illumination whose photon energies are slightly above the work function of these materials, the electrons are emitted in a process called threshold photoemission. In PEEM imaging, a mercury (Hg) discharge lamp with a cutoff energy of 4.9 eV is typically used to achieve this purpose.

It was later recognized that such electron emission carries very useful information about the electronic structure and properties of solids and hence different theoretical models have been developed to understand and explain these complex photoemission processes [85–87]. Nevertheless, the three-step model² in photoemission is the most common theory to describe the photoemission process intuitively yet successfully despite its oversimplification [87–89]. The first step is described by Fermi's golden rule which states that an electron in its initial state $|\psi_i\rangle$ can be excited to the final

²The three-step model mentioned here is not equivalent to the three-step model in HHG.

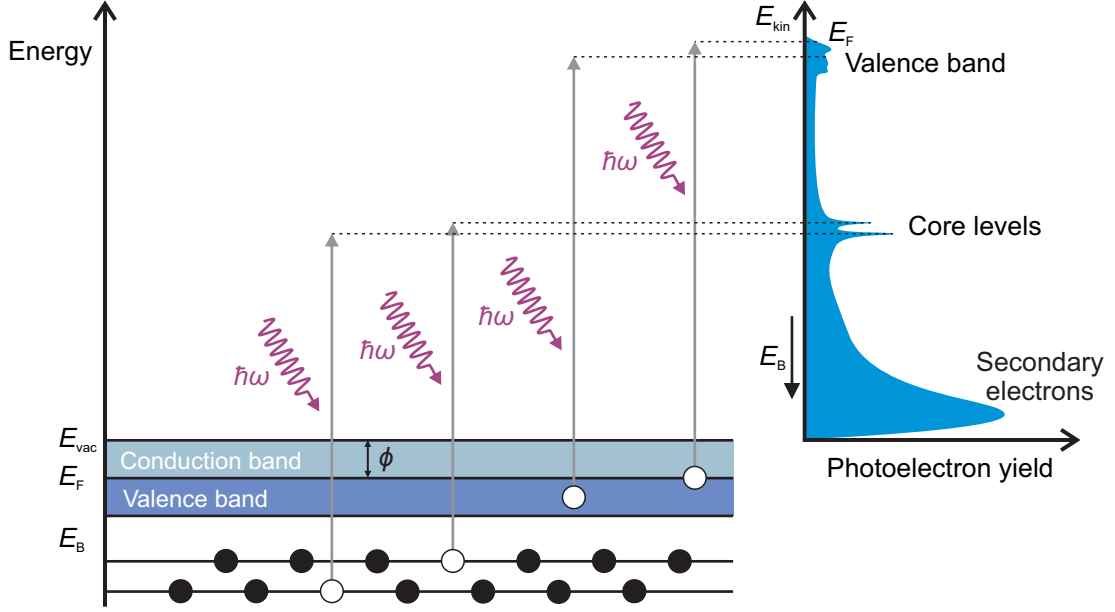


Figure 2.4: Schematic diagram of linear photoemission in a solid. Electrons with kinetic energies E_{kin} can escape into the vacuum by absorption of photons with energies $\hbar\omega$ according to eqn 2.3. The Fermi level E_F is between the conduction band and valence band (or within the conduction band if it is partially filled, as for metals) and is separated by work function ϕ from the vacuum level E_{vac} . The electrons in the valence band and core levels with binding energies E_B can be excited to the vacuum by higher photon energies such as X-ray. Secondary electron cascades formed by electron-electron interactions typically have a higher yield in the spectrum.

state $|\psi_f\rangle$ by absorption of a photon of an energy of $\hbar\omega$. The transition probability per unit time of such excitation is expressed by

$$\Gamma_{i \rightarrow f} = \frac{2\pi}{\hbar} |\langle \psi_f | H' | \psi_i \rangle|^2 \delta(E_f - E_i - \hbar\omega). \quad (2.4)$$

Here, H' represents the perturbing Hamiltonian of the ionizing field and the δ function ensures energy conservation during the optical transition. The second step is followed by the transport of the electron through the solid to the surface and finally the penetration through the surface into the vacuum. There is another more accurate model which is called one-step model since it takes all effects, e.g. surface-specific effects, into account [90]. This model considers a direct transition from the initial Bloch state into a free propagating state in the vacuum by penetrating the solid.

As shown in eqn 2.3, the photoemission technique also provides the possibility to gain access to the valence bands and core levels of the materials (when $E_B \neq 0$) using higher energy photons. The direct determination of the band structure via valence band electrons was only made possible with the advent of angle-resolved photo-

emission spectroscopy. X-ray photoelectron spectroscopy using mainly synchrotron radiation has been very useful to reveal deeply bound states of a broad range of materials by detecting primary electrons for element-specific studies. On the other hand, secondary (low-energy) electrons created in Auger processes and inelastic electron scattering are suitable for X-ray magnetic circular dichroism (XMCD) domain imaging with PEEM. This is because the secondary electron yield is proportional to the X-ray absorption cross-section which is sensitive to dichroism [91]. Fig. 2.4 depicts schematically how the energy-level diagram and the photoelectron spectrum relate to each other as a summary for the linear photoemission discussed in this subsection.

2.2.2 Nonlinear photoemission

The realization of cutting-edge femtosecond laser systems with high peak intensities in the last decades has prompted experimental studies of nonlinear photoemission from solid surfaces. Utilizing the field enhancement at nanostructures arising from surface plasmon excitation has brought new aspects to nonlinear phenomena as the electromagnetic field can be confined into a nanoscale volume [12, 33, 92, 93]. For a nonlinear process, the photoelectron yield no longer scales linearly with the intensity of the incident light. Moreover, electrons can be emitted from the surface even if the photon energy is smaller than the work function of the material (see subsection 2.2.1). The relevant nonlinear photoemission mechanisms including multiphoton photoemission and strong-field effects concerning this work, such as ATP and light-induced tunneling, will be reviewed.

The aforementioned photoemission mechanisms from a solid depend on the intensity of the laser light and work function ϕ of the solid material. The different regimes of photoemission can be classified and described successfully by the ubiquitous Keldysh theory albeit it was originally introduced for characterizing the ionization of atoms [94, 95]. The Keldysh parameter γ , also known as the adiabaticity parameter, is defined as

$$\gamma = \sqrt{\frac{\phi}{2U_p}} = \frac{\omega\sqrt{2m_e\phi}}{eE_0}. \quad (2.5)$$

Here, ϕ is the work function which can be replaced by the ionization potential I_p if an atomic system is considered. U_p is the ponderomotive potential energy, see subsection 2.1.2 for its definition. ω is the angular frequency of the laser, m_e the electron mass, e the electron charge and E_0 the electric field amplitude.

For lower laser intensities ($\gamma \gg 1$), multiphoton photoemission predominantly takes place since the laser field is not sufficient to overcome the binding potential of the bound electron. If the photon energy is below the work function, the photo-

emission process requires n photons to be absorbed quasi-simultaneously to free an electron into the continuum state (see fig. 2.5 (a)). Hence the kinetic energy E_{kin} of an electron released through a n -photon photoemission process can be written as:

$$E_{\text{kin}} = n\hbar\omega - \phi. \quad (2.6)$$

The photoemission rate $P(I) = \sigma_n I^n$ is obtained by summing the transitions over all possible intermediate states; here σ_n is the proportionality constant related to the matrix elements, n the number of photons and I the laser intensity. This nonlinear process can accurately be described by n -th order perturbation theory since the interaction between light and solid is predominantly non-adiabatic and is governed by the intensity envelope of the laser light. Resonant multiphoton photoemission occurs when at least one real intermediate state is involved during the transition. Under such condition, the photoemission probability can be greatly enhanced and the lifetime of intermediate states can be revealed using time-resolved two-photon photoemission spectroscopy. On the other hand, non-resonant multiphoton photoemission occurs via short-lived virtual intermediate states [96].

Moving towards higher intensity than that needed for multiphoton photoemission, ATP starts to come into play where more photons are absorbed than the minimum required number ($n > n_{\text{min}}$), as illustrated in fig. 2.5 (b). ATP is characterized by non-perturbative effects. Importantly, ATP spectra from flat metal surfaces exhibit a series of peaks spaced by the photon energy $\hbar\omega$ [97–101] which have been observed before in atomic systems [102, 103]. A more direct evidence of ATP was shown by M. Schenk *et al.* [104] where a sharp metal nanotip was used. Distinct peak features separated by ~ 1.5 eV (corresponding to the photon energy) and a photon order of up to 9 were measured in the spectra. It is worthwhile to mention that suppression of lowest order peaks and peak shifting to lower energies with increased laser intensities in the ATP mark the onset of strong-field effects [104].

For very high peak intensities around 10^{14} W/cm² – 10^{17} W/cm² ($\gamma \ll 1$) at a wavelength of 800 nm, a tunneling regime (also termed as optical field emission) is reached. As opposed to the two cases before, an electron can tunnel out from the metal surface because the optical field is large enough to overcome its binding potential (see fig. 2.5 (c)). The process is known to be adiabatic since the electron interacts and follows the field evolution instantaneously. The photoemission rate $P(\gamma)$ for $\gamma \ll 1$ in the presence of static electric fields [94, 95] is given as:

$$P(\gamma) \propto \exp\left(-\frac{4\sqrt{2m}\phi^{3/2}}{3|e|\hbar E_0}\right). \quad (2.7)$$

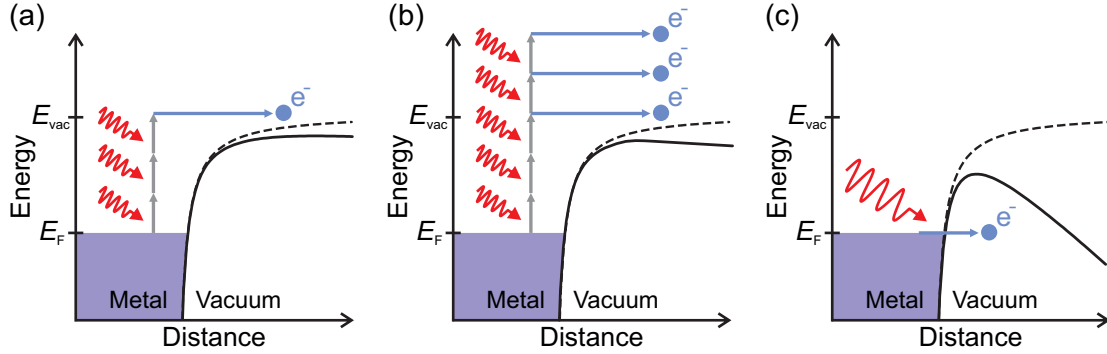


Figure 2.5: Potential energy diagrams of different photoemission mechanisms from a metal surface. (a) Multiphoton photoemission: multiple photons (red) are absorbed quasi-simultaneously by the metal surface to emit one electron (blue) over the potential barrier (dotted black line). The potential is only weakly perturbed (black line) by the light field. (b) ATP: with increased laser intensity, more photons are absorbed than necessary by the metal surface to set one electron free. The potential is more perturbed by the light field compared to the case in (a). (c) Tunneling regime: the potential is substantially distorted by the strong applied field and the electron can tunnel out from the Fermi level into the vacuum. This regime can be reached by either a very strong peak electric field or a low laser frequency (see eqn 2.5).

In general, most bulk metal surfaces or metallic thin films have a laser damage threshold on the order of $10^{12} \text{ W/cm}^2 - 10^{13} \text{ W/cm}^2$ [105, 106], which is close to $\gamma \approx 1$. Metallic nanostructures can surpass this limit easily and reach the tunneling regime, i.e. $\gamma \ll 1$, owing to their achievable high plasmonic field enhancement for obtaining very strong optical fields (or very high peak intensities). F. Schertz *et al.* obtained $\gamma \approx 0.2$ from a strongly coupled plasmonic system which has a sub-nanometer gap using a NIR laser with a low peak intensity of $\sim 10^{10} \text{ W/cm}^2$ without sample damage [107]. Other possible emission mechanisms such as thermally-assisted photoemission [108] and field emission [109] can mutually exist together with the aforementioned nonlinear processes, which may further complicate the interpretation of photoemission measurements.

2.3 Plasmonics

Plasmonics, which explores the confinement of electromagnetic fields in subwavelength dimension, is a major area of the rapidly-evolving field of nanophotonics. By definition, surface plasmons are collective electron excitations at metal-dielectric interfaces appearing as localized field enhancements (localized surface plasmons, LSPs) on isolated nanoscaled metal structures or traveling plasmon excitations (surface plasmon polaritons, SPPs), for instance, in plasmonic waveguides upon light exci-

tation. In this section, a new experimental concept using near-field PEEM to study LSPs with both attosecond time and nanometer spatial resolution will be presented.

2.3.1 SPPs and LSPs

Theoretically, propagating SPPs are an analytical solution of Maxwell's equations considering the boundary conditions at the metal-dielectric interface. These SPPs, inherently bound to an interface, can only be excited by light under the condition in which the wavevector of the light is matched to the wavevector of the SPP. As depicted in fig. 2.6 (a), these propagating electromagnetic waves are of transverse magnetic polarization in nature, where their electric fields are along the z -direction at the surface and decay exponentially into the metal ($z < 0$) as well as into the dielectric ($z > 0$). Such exponentially decaying z -components of the electric field are called evanescent waves. Note that the penetration depth inside the dielectric δ_d is longer than the penetration depth inside the metal δ_m [110] owing to the negative real part of the metal's dielectric constant (or relative permittivity) ϵ . The dispersion relation of SPPs propagating at the dielectric-metal interface is expressed as

$$k_{\text{SPP}}(\omega) = k_0 \sqrt{\frac{\epsilon_m(\omega) \cdot \epsilon_d(\omega)}{\epsilon_m(\omega) + \epsilon_d(\omega)}}, \quad (2.8)$$

where k_0 is the wavevector in vacuum, and $\epsilon_m(\omega)$ and $\epsilon_d(\omega)$ are the dielectric functions of the metal and the dielectric, respectively. To satisfy the wavevector matching (or phase matching) between the excitation light and the SPP, a grating or a prism coupler [111], known as the most common methods, can be used to provide the required wavevector component for coupling the light to a SPP. To date, numerous works employing plasmonic waveguides (e.g. metal grooves, metal-insulator-metal slabs, semiconductor nanowires, elementary logic gates, etc.) for propagating SPP applications have been studied [112], aiming ultimately to use light to overcome the speed limit of conventional electronics for future-generation integrated circuits. This work rather focuses on LSPs, which will be introduced below, attempting to reveal their subfemtosecond dynamics utilizing a PEEM.

On the other hand, non-propagating surface excitations of small, subwavelength nanosystems coupled directly to the light without wavevector matching are referred to as LSPs. Fig. 2.6 (b) illustrates the displacement of the conduction electron cloud relative to the positive ions driven by the oscillating external electromagnetic field. The electrons are then accelerated towards the parent ions due to the restoring force exerted by the electric field built up between them. Such oscillating motion (or resonance) results in strong light scattering, manifested by intense surface plasmon

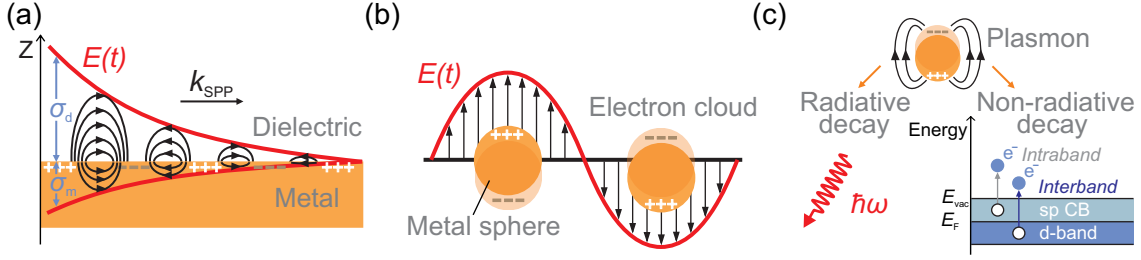


Figure 2.6: Sketches of SPPs and LSPs. (a) Propagating SPP at a metal-dielectric interface with its collective charge oscillation (+ and -). The electric fields (black arrows) are normal to the surface and decay exponentially along the direction of SPP propagation (k_{SPP}). Red lines show the envelopes of the electric fields. (b) LSP excited by an oscillating external light field (red line and black arrows). The light field displaces the free electrons on the metal sphere, which are later driven back to the positive ions due to the restoring force, resulting in an oscillating motion. (c) Radiative and non-radiative decay channels of the surface plasmons. A plasmon can decay radiatively by emitting a photon with an energy of $\hbar\omega$. Alternatively, it decays non-radiatively by creating an electron-hole pair via either an intraband transition within the sp conduction band (CB) or an interband transition from a lower-lying d-band to above of the Fermi level E_F .

absorption and enhancement of localized electromagnetic fields. For a spherical particle of radius $R \ll \lambda$, i.e. much smaller than the excitation wavelength, a simple quasi-static approximation can be used to analytically calculate the electric fields inside and outside of the sphere. By solving the electrostatic problem, the fields inside, \mathbf{E}_{in} , and outside, \mathbf{E}_{out} , of the particle, respectively, are evaluated to be [111]

$$\mathbf{E}_{\text{in}} = \frac{3\epsilon_a(\omega)}{\epsilon_p(\omega) + 2\epsilon_a(\omega)} \mathbf{E}_0 \quad (2.9)$$

$$\mathbf{E}_{\text{out}} = \mathbf{E}_0 + \frac{3\mathbf{n}(\mathbf{n} \cdot \mathbf{p}) - \mathbf{p}}{4\pi\epsilon_0\epsilon_a(\omega)} \frac{1}{r^3}. \quad (2.10)$$

Here, \mathbf{n} is the normal vector pointing away from the center of the sphere, r is the distance from the center, ϵ_0 is the electric permittivity of vacuum and $\epsilon_p(\omega)$ and $\epsilon_a(\omega)$ are the dielectric functions of the particle and of the ambient medium, respectively. The field of the oscillating wave is assumed to be spatially constant over the particle volume and induces a dipole moment \mathbf{p} proportional to the applied field amplitude \mathbf{E}_0 . Hence, the resulting polarizability $\alpha(\omega)$ of the subwavelength particle in response to the electric field [111, 113] is expressed as

$$\alpha(\omega) = 4\pi R^3 \frac{\epsilon_p(\omega) - \epsilon_a(\omega)}{\epsilon_p(\omega) + 2\epsilon_a(\omega)}, \quad (2.11)$$

where R is the radius of the particle. A resonant enhancement can easily be obtained when $|\epsilon_p(\omega) + 2\epsilon_a(\omega)|$ is a minimum. If $\text{Re}[\epsilon_p(\omega)] = -2\epsilon_a(\omega)$, the Fröhlich condition is satisfied and the resonance is due to a dipole surface plasmon at the metallic nanoparticle [111]. The quasi-static approximation is only valid for very small spheres or ellipsoids with dimensions below 100 nm. For the case of larger particles above 100 nm, the significant field variation of the incoming light wave needs to be taken into account. Mie theory [114] proves to provide a successful analytical solution as it considers the expansion of the internal and scattered fields into vector spherical harmonics to solve the problem for larger particles. Higher order modes, i.e. multipoles, can be excited which lead to red shift and broad resonance for increasing particle size. For plasmonic systems of arbitrary and complex geometries, numerical methods such as finite element or finite-difference time-domain are preferred over analytical calculations to obtain the field distributions.

The plasmon resonance is highly sensitive to the size, size distribution and geometry of the nanosystems, type of materials as well as the dielectric properties of the surrounding environment. Gold, being a chemically stable metal, has an optical response in the visible and NIR spectral region. This makes gold an excellent plasmonic material for fabricating the nanostructures used in this work. Besides single isolated nanostructures such as gold triangles, coupled nanosystems which can achieve a much higher field enhancement, e.g. gold nanoparticles on a gold plane (NPOP) and gold surface roughness, are being explored in this work. Typically, plasmon oscillations have a lifetime of 1 fs – 100 fs [115–117]. Fig. 2.6 (c) details the possible decay channels of the plasmon. The first damping process is characterized by a re-emission of photons to the far field (radiative decay, also referred to as bright modes), particularly for larger nanostructures, and is being linked to the particle's scattering cross-section. A second relaxation pathway are inelastic scattering processes which result in the creation of electron-hole pairs via intra- or interband excitations and the thermalization of the electron gas (non-radiative decay, also referred to as dark modes). The non-radiative process is dependent on the band structure of the nanostructure. Finally, thermalization of the electrons from the plasmon decay with the phonons in the lattice and energy transfer to the surrounding environment through phonon-phonon scattering take place on the picosecond timescale [116, 118].

Far-field optical spectroscopy can be used exclusively to detect bright modes by measuring the scattering and extinction spectra of the nanostructures. Bright modes are strong dipole moments that can couple very efficiently to the far field and decay radiatively under plane wave excitation. Dark modes, on the other hand, are pure near-field resonances and their dipole moments oscillate out of phase and therefore vanish in the far field. Under certain circumstances, dark modes can be excited if the symmetry of the system is broken by employing asymmetric excitations, e.g.

tilted plane wave excitation (grazing incidence illumination) [119] or a localized dipole emitter [120]. Non-radiative dark modes can therefore be probed by several near-field measurement techniques such as SNOM [121, 122], electron energy loss spectroscopy [123, 124], photon-induced near-field electron microscopy [125, 126] and PEEM [127, 128]. PEEM, being the technique used in this work, is capable of imaging the near-field intensity distribution of plasmonic fields directly and noninvasively with ultrahigh spatiotemporal resolution. The concept and perspectives of utilizing a PEEM for investigating ultrafast plasmonics, the topics of this work, are elaborated on in the following subsection.

2.3.2 Atto-PEEM concept for ultrafast plasmonics

Real-time observation of nanoplasmonic fields with femtosecond temporal resolution, as given by the duration of the probe pulses, has been realized for more than a decade. One common experimental method to achieve this goal is using interferometric time-resolved PEEM [29, 129, 130] in which the detected photocurrent $j(\mathbf{r})$ is highly sensitive to the plasmonic field strength due to the nonlinear photoemission process (e.g. $j(\mathbf{r}) \propto |\mathbf{E}^4|$ in the case of two-photon photoemission). Propagation, build-up and decay of SPPs could be observed in nanoplasmonic vortices [32]. Furthermore, coherent spatiotemporal control of optical near-field distributions by excitation with polarization-shaped femtosecond light pulses has also been shown [30]. A different technique has been demonstrated by the group of A. H. Zewail, where they imaged evanescent electromagnetic fields from carbon nanotubes using high-energy (200 keV) femtosecond electron pulses. The kinetic energy of these electron pulses is modulated when passing through the near fields, thus spatiotemporal mapping could be achieved by using an energy-resolved TEM [125].

Intrinsically, LSPs could undergo ultrafast dynamics as short as a few hundred attoseconds as given by the inverse broad spectral bandwidth of the plasmonic resonances when excited by few-cycle femtosecond laser pulses [117, 131]. In 2007, M.I. Stockman *et al.* [117] proposed an approach which combines energy-resolved PEEM and attosecond streaking spectroscopy [38, 39, 132] to detect the plasmon dynamics with nanometer spatial and attosecond temporal resolutions in an optical-pump/XUV-probe scheme. This technique is dubbed “atto-PEEM” and is illustrated in fig. 2.7 (a). The underlying idea is to use a waveform-controlled (or CEP-resolved) few-cycle optical pulse (pump pulse) to resonantly excite the nanoplasmonic fields on a nanostructured metal surface, while a synchronized isolated attosecond XUV pulse (probe pulse) with a variable time delay is then sent to the system to probe the fields. The XUV pulse emits valence band electrons from the surface whose kinetic energies are high enough (due to the high photon energy of the XUV pulse) to sep-

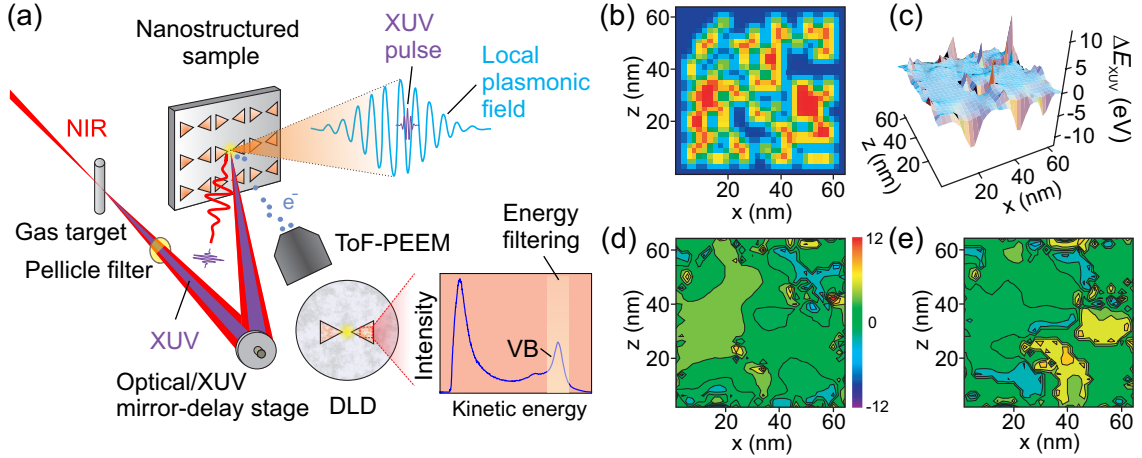


Figure 2.7: Schematic illustration of the atto-PEEM concept and attosecond nanoplasmonic fields. (a) Principle and concept of atto-PEEM: local plasmonic fields are resonantly excited in a nanostructured sample by an incident NIR laser pulse. The synchronized XUV pulse which is produced in a gas target via HHG by the same NIR pulse is delayed and sent to the nanosystem for probing the plasmonic fields. The local near field is enhanced with respect to the NIR field. A pellicle bandpass filter is used to block the central portion of the NIR beam and low harmonics but allow the XUV to pass through. Both the NIR and XUV pulses propagate collinearly and are focused onto the sample by a mirror-delay stage. Upon XUV excitation, electrons are photoemitted from the sample surface and subsequently streaked in the nanoplasmonic fields. These electrons are then extracted and imaged by a PEEM equipped with a ToF spectrometer via a delayline detector (DLD). The valence band (VB) electrons which are of interest can be energy-filtered from the inelastically scattered secondary electrons. (b) A simulated random rough silver surface consists of a grid of $4 \text{ nm} \times 4 \text{ nm} \times 4 \text{ nm}$ silver cubes. (c) A three-dimensional map displaying the energy shift ΔE_{XUV} caused by acceleration and deceleration of electrons in the nanoplasmonic fields. (d)-(e) Topographic maps showing the energy shift (color-coded) for different instances (or time delays). The spatial distributions of energy shift ΔE_{XUV} showing hot-spot dynamics for varying time delays; $\Delta t_{\text{XUV}} = 16.68 \text{ fs}$ in (c), $\Delta t_{\text{XUV}} = 16.87 \text{ fs}$ in (d) and $\Delta t_{\text{XUV}} = 17.25 \text{ fs}$ in (e). Figure taken from [117].

arate them from the background of multiphoton photoemission and ATP induced by the optical pulse. Photoelectron streaking of the liberated fast valence band electrons in the plasmonic near fields results in an increase or decrease of kinetic energy, which can then be spatially and spectroscopically detected in PEEM.

Unlike the classical attosecond streaking, the fast XUV-emitted photoelectrons experience an instantaneous acceleration and escape from the nanoplasmonic field region with negligible influence of the optical field. In this instantaneous regime, the electron escape time τ_e is much shorter than the optical field oscillation period T ($\tau_e \ll T$) since the plasmonic field is localized within a few nanometers. Hence, the final kinetic energy E_{XUV} of a photoelectron is related to the instantaneous local electrostatic potential $V(\mathbf{r}, t_{\text{XUV}})$ at the instant of the electron's emission t_{XUV}

(precisely defined by the incidence time of the XUV pulse) and the emission position \mathbf{r} via the following equation [117]:

$$E_{\text{XUV}}(\mathbf{r}, t_{\text{XUV}}) = \hbar\omega_{\text{XUV}} - \phi + eV(\mathbf{r}, t_{\text{XUV}}), \quad (2.12)$$

where \hbar is the reduced Planck's constant, ω_{XUV} the angular frequency of the XUV pulse, ϕ the metal work function and e the electron charge. Fig. 2.7 (b)-(e) show the simulation results of M. I. Stockman *et al.* using a random rough silver surface with a maximum field enhancement factor of ~ 30 . In their calculations, a 5.5 fs few-cycle NIR pulse of 800 nm and a 170 as XUV pulse at 93 eV were employed. An energy shift up to ~ 10 eV was obtained for a moderate NIR laser intensity of 10^{10} W/cm², as shown in fig. 2.7 (c). These hot-spot dynamics which occurs on an attosecond timescale (e.g. 200 as – 400 as) can be measured via the time delay between the pump and probe pulses (see fig. 2.7 (c)-(e)).

A different approach to access nanoplasmonic fields with attosecond time resolution was proposed by A. Mikkelsen *et al.* [35], which is detecting the lateral changes in electron density at the surface induced by the nanoplasmonic fields by taking advantage of the abundant secondary electrons released upon XUV excitation. As opposed to the original atto-PEEM concept, they suggested using a single optical pulse and a synchronized attosecond XUV pulse train in a pump-probe scheme. However, the concept of atto-PEEM using secondary electrons is indirect and the measurable nanoplasmonic dynamics can be limited by the slow secondary electrons to a temporal resolution close to ~ 1 fs [36, 133].

E. Skopalová *et al.* [134] later theoretically showed that a reconstruction of the nanoplasmonic fields is feasible from supported gold nanoantennas when spatial averaging is applied at the emission point in the classical oscillatory regime known from gas-phase atomic targets. Further theoretical studies on nanoplasmonic streaking of single metallic nanospheres [135–137] demonstrated that the streaking behavior is highly dependent on the emission position and particle size. So far, nanoplasmonic streaking utilizing atto-PEEM has not been realized because of the experimental challenges of working with low-repetition-rate attosecond XUV sources [34, 35, 138]. The main issue is a severely limited photoelectron signal yield, since only a low XUV intensity can be used in order to avoid space charge effects and maintain high spatial resolution (see section 4.3). Using these XUV sources, it is therefore nearly impossible to realize reasonable acquisition times for the pump-probe experiments considering the experimental stability. Due to these reasons, only a recent work on nanoplasmonic streaking in the oscillatory regime, performed on a gold nanotip without spatial resolution [139] has succeeded so far. Their experimental results showed

that the near fields at the tip were shifted by ~ 200 as with respect to the incoming laser field for an intensity below the onset of nonlinear effects.

Experimental setup

In essence, this work presents experimental investigations of ultrafast dynamics from metallic nanostructures and surfaces with spatial and energy resolution using ultra-short laser pulses as short as a few femtoseconds to several hundred attoseconds. The experiments described in this work require a versatile and complex setup involving many different techniques. The crucial detection instrument for probing ultrafast dynamics, the energy-resolved PEEM, and its working principle are described. Few-cycle NIR laser pulses and HHG from 1 kHz and 10 kHz laser systems are utilized here as the light sources for light-matter interactions. The methods and techniques of the few-cycle laser sources and XUV generation are given in this chapter. In addition, the combination of the energy-resolved PEEM with a single-shot stereographic above-threshold ionization (ATI) phase meter for studying CEP control in plasmonic nanostructures and at surfaces is outlined. Finally, the methods for nanostructure fabrication are presented.

3.1 PEEM

PEEM has been a powerful tool for studying surface science since its invention in the early 1930s [140]. It utilizes the photoelectric effect to image the lateral distribution of electrons emitted from the surface by the absorption of photons with an energy that exceeds the sample's work function. The excitation sources are usually UV light, synchrotron radiation, and lasers. The spatial resolution of PEEM is typically a few nanometers to a few tens of nanometers, owed to the fact that the de-Broglie wavelength of electrons is in the nanometer range at an energy of a few electronvolts. The spatial resolution is essentially only limited by the aberrations due to electron optics and excitation sources.

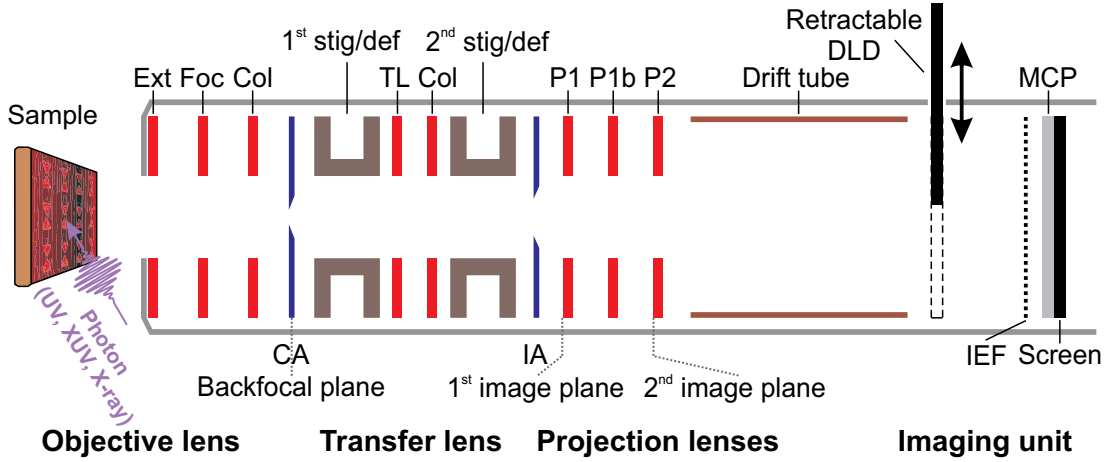


Figure 3.1: Electron-optical design of the 30 kV ToF-PEEM. Ext: extractor, Foc: focus, Col: column, Stig/def: stigmator/deflector, TL: transfer lens, P: projector lens, CA: contrast aperture, IA: iris aperture. See text for further explanation.

Basically, a PEEM consists of an imaging electron lens system, a magnification unit and an image acquisition device. Besides electrostatic tetrode lenses, magnetostatic triode lenses, which have lower aberration, are also used in commercially available PEEM instruments. The electrostatic lens systems are protected from stray magnetic fields by a closed μ -metal shielding around the PEEM. The PEEM used in this work is a ToF-PEEM (FOCUS IS-PEEM) based on electrostatic lenses from FOCUS GmbH. It has a maximum extractor voltage of 30 kV and we use the standard 65° incidence of illumination to the normal of the sample surface for all the experiments described in this work. The ToF-PEEM has an integral sample stage with piezoelectrically driven sample positioning which effectively improves the imaging stability by decreasing vibration and sample drift.

Fig. 3.1 depicts a schematic diagram of the electrostatic lens system of the ToF-PEEM. It starts with the sample stage which also forms the cathode of the tetrode objective lens besides the extractor, focus and column electrode. The sample distance to the extractor is fixed at 2.8 mm, which is rather long in comparison to the typical distance of 1.8 mm, since our ToF-PEEM has a maximum extractor voltage of 30 kV. Sample quality such as a clean and smooth sample surface with a good conductivity is essential to achieve imaging with high spatial resolution. Otherwise, sample charging due to excessive electrons in the cathode can arise. In addition, the high extractor field applied on the sample can induce cold field emission at surface roughness sites, i.e. sharp edges or sharp tips, due to the strongly enhanced local electrostatic field. These factors can lead to strong and non-uniform variations of the photocurrent, thus resulting in a reduction of spatial resolution.

The working principle of ToF-PEEM imaging is illustrated in the following. The objective lens images the photoelectrons from the sample onto the first image plane with approximately $40\times$ magnification. A contrast aperture of a variable diameter between $30\ \mu\text{m}$ and $1500\ \mu\text{m}$ is placed in the back focal plane of the objective lens. Using different sizes of the contrast aperture, the interplay between spatial resolution and image intensity is optimized. An octupole stigmator/deflector for correcting astigmatism and alignment errors of the optical axis is positioned right behind the contrast aperture. The intermediate image is then magnified and focused by two subsequent projective lenses onto the screen. This telescope configuration allows a field of view adjustment from $1\ \text{mm}$ down to $2\ \mu\text{m}$. The highest magnification of $\sim 10\,000\times$ is achieved by producing two intermediate images before the imaging assembly. In the k-space imaging mode, the angular distribution of electrons from the sample is imaged onto the back focal plane (also called diffraction plane) of the objective lens and consequently projected onto the screen by an additional transfer lens. A second stigmator/deflector situated before the first image plane is used to improve the angular resolution of the electrons. A continuously variable iris aperture right at the first image plane can be used for micro-spot analysis in the k-space imaging mode or contrast enhancement in the real space imaging mode. A drift extension is added inside the PEEM after the second projective lens for time- and energy-resolved imaging. A complementary IEF, which is a high-pass retarding field analyzer, can also be used for energy-filtered imaging particularly when applying high intensity. The first imaging assembly consists of a microchannel plate (MCP) and a fluorescence screen made of a YAG single-crystal with aluminum coating, which is imaged by a charge-coupled device (CCD) camera (CoolSNAP fx, Roper Scientific Photometrics). Alternatively, a delayline detector (DLD) can be used for imaging not only the spatial distribution of the electrons but also recording their kinetic energies. Both detectors are integrated in a straight column in the PEEM.

3.1.1 ToF spectrometer

In this subsection, the DLD (Model 3636, Surface Concept GmbH) in combination with the usage of a drift tube as a ToF spectrometer in the PEEM is described in detail. More comprehensive descriptions on the working principle and applications of a DLD can be found in [141–144]. In short, a DLD consists of MCPs and two lithographically manufactured meander-like wire grids. These wire grids are called delaylines; one is placed below the other, rotated by 90° , closely together but insulated. The MCPs, as a position sensitive electron multiplier, first amplify the incoming electrons by a factor of at least 10^7 [144]. These secondary electron clouds travel within picoseconds from the MCPs onto the delayline anodes and induce elec-

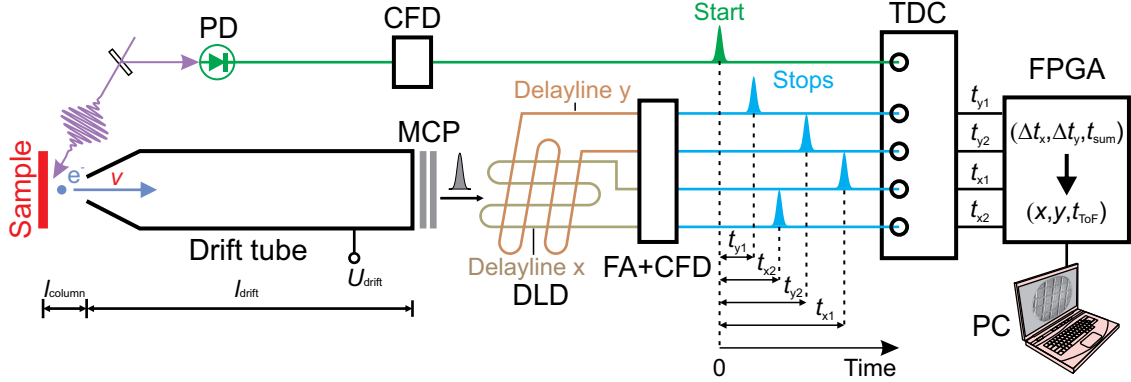


Figure 3.2: Working principle of a ToF spectrometer via a DLD. A photoemitted electron leaves the sample surface upon light excitation with a characteristic velocity, v , accelerates in the PEEM column and retards in the drift tube. The electron then induces an electrical pulse after passing the MCP that travels towards the DLD. Four pulses are generated on the delayline x and y for each incoming photoelectron, later converted into precise time signals by a fast amplifier (FA) and a constant fraction discriminator (CFD). The same light pulse detected by a photodiode (PD) starts the clock and acts as a reference for the detected electron which stops the time measurement. The accurate time measurement is processed by a TDC and a field-programmable gate array (FPGA) and read by a PC.

trical pulses inside the delayline wires via image charge coupling. The traveling time of these pulses to the wire ends depends linearly on the respective position on the wire frame where the electron cloud hits the wire. Using an external start trigger signal, the DLD therefore enables absolute time measurements (with respect to the start trigger) in addition to the lateral position measurements. Our DLD has a temporal response width of ~ 220 ps FWHM and is able of measuring a count rate of up to 3 MHz. It should be noted that a DLD is a single-electron counting device, which is advantageous for efficient low count rate detection.

Owing to its capability of simultaneously acquiring lateral positions of electrons and their corresponding kinetic energies, microspectroscopic imaging and energy-selective imaging can be realized when it is used with a PEEM. The detection scheme of a ToF spectrometer by means of a DLD is outlined schematically in fig. 3.2. The impinging light pulse releases an electron from the sample. This electron is accelerated by a voltage over a length l_{column} between the sample and the start of the drift tube. The same light pulse is used as a start trigger to start the time measurement. This can be done via a photodiode which converts the light pulse into a pulse of photocurrent and then feeds it into a constant fraction discriminator to avoid false threshold triggering. Due to the photoelectric effect, the electron leaves the sample surface with a certain kinetic energy, E_{kin} , when the photon energy exceeds the sample's work function. Assuming a direct photoemission process, the

kinetic energy is given by the initial state of the electron. The electron is retarded to a lower drift potential, U_{drift} , in order to introduce sufficient temporal dispersion in the drift tube. Hence, the electron propagates with its characteristic velocity v that is determined by its kinetic energy after leaving the surface and the drift potential. In other words, the electron carries an energy of $eU_{\text{drift}} + E_{\text{kin}}$ inside the drift tube of length l_{drift} , e being the elementary charge. At the end of the drift path, the electrons and their arrival time with respect to the start trigger are detected by the DLD. One should also take into account the work function difference $\Delta\phi$ between the sample's and drift tube's work function. Therefore the velocity v experienced by an electron in the drift tube is given simply by the following equation:

$$\frac{1}{2}m_e v^2 = eU_{\text{drift}} + E_{\text{kin}} + \Delta\phi, \quad (3.1)$$

m_e being the electron's mass. Solving eqn 3.1 for the velocity v and using $v = dz/dt$ (z being the position) yields

$$\frac{dt}{dz} = \sqrt{\frac{m_e}{2e}} \cdot \left(U_{\text{drift}} + \frac{E_{\text{kin}} + \Delta\phi}{e} \right)^{-\frac{1}{2}}. \quad (3.2)$$

We obtain the ToF, t_{ToF} , by integrating eqn 3.2:

$$t_{\text{ToF}} = \sqrt{\frac{m_e}{2e}} \int_{z_0}^{z_d} \left(U_{\text{drift}} + \frac{E_{\text{kin}} + \Delta\phi}{e} \right)^{-\frac{1}{2}} dz, \quad (3.3)$$

where $z_0 - z_d = l_{\text{drift}}$. Eqn 3.1 finally yields a linear relation between the ToF and kinetic energy by a first-order Taylor approximation of eqn 3.3 [145]:

$$E_{\text{kin}} + \Delta\phi \approx 2\sqrt{\frac{m_e}{2e}} U_{\text{drift}}^{\frac{3}{2}} l_{\text{drift}} t_{\text{ToF}}. \quad (3.4)$$

The operation of a DLD is illustrated in fig. 3.2. The induced electrical pulses travel with a velocity v towards both ends of the delayline x . At the end of the delayline, a time-to-digital converter (TDC) detects the arrival time of the pulses. The measured time $t = t_0 + x/v$ contains the information about the position x where the electron hits the delayline. Here, t_0 is a time offset (see section below). The position x can then be calculated by the difference $\Delta t_x = t_{x_1} - t_{x_2}$ between the arrival times of both pulses, using an inversion algorithm which takes into account the geometrical and electrical properties of the delayline. Likewise, the position y can be determined by the time difference $\Delta t_y = t_{y_1} - t_{y_2}$ within delayline y . With

reference to an external clock, given by the start trigger pulses, the ToF of the electrons can be calculated by the sum of the measured times:

$$t_{\text{sum}} = t_{x_1} + t_{x_2} = 2t_0 + \frac{x_1}{v} + \frac{x_2}{v} = 2t_0 + \frac{L_{\text{delay}}}{v}, \quad (3.5)$$

where L_{delay} is the total length of the delayline x . It is possible to sum only t_{x_1} and t_{x_2} or t_{y_1} and t_{y_2} . Since both x and y sums carry the same temporal information, the total sum of all four time measurements, t_{x_1} , t_{x_2} , t_{y_1} and t_{y_2} can be used for obtaining the ToF with a better precision. From this, the kinetic energy of the electrons can be obtained using eqn 3.4. For accurate time measurements, a fast data acquisition unit comprised of a fast amplifier and a constant fraction discriminator is used to process the pulses before the TDC, which measures the time between the start trigger pulse and the four stop pulses at the ends of both delaylines. For each detected electron, a field-programmable gate array computes the image coordinates (x, y) from the time differences as well as the ToF (t_{ToF}) from the time sums and transfers the data as (x, y, t_{ToF}) -tuples to a personal computer (PC). A software is then used to calculate spatial and temporal histograms from all electron counts (images or ToF spectra, respectively).

3.1.2 Energy calibration

Absolute spectral measurements are crucial in acquiring the spectroscopic information of photoemission processes from surfaces accurately. Therefore, the ToF spectrometer used in this work has to be properly calibrated to exclude any systematic errors. In principle, there are three methods to perform an energy calibration of a ToF spectrometer:

First, a well-studied sample of a known spectrum, such as the electronic density of states, can be used as a reference to calibrate a ToF spectrometer for converting a ToF spectrum into an energy spectrum. Second, a photon peak can be used to determine the time offset, a time constant related to cable lengths, electron propagation times and experimental geometry. In general, the time offset t_0 is related to the ToF, t_{ToF} , and time sum, t_{sum} , as follows:

$$t_{\text{sum}} = t_0 + t_{\text{ToF}}. \quad (3.6)$$

The photon peak can be detected at the DLD by using the scattered light from the sample surface [146]. Since the photons travel with the speed of light, they arrive earlier at the detector than the electrons passing through the drift tube. In particular, t_0 is the time between the start trigger signal and the incidence of the

light pulse on the sample. Ultimately, this time offset t_0 can be determined using the following equation:

$$t_0 = t_{\text{phot}} - \frac{l_{\text{column}} + l_{\text{drift}}}{c}, \quad (3.7)$$

where t_{phot} is the time when the photons hit the detector, l_{column} is the distance between the sample surface and the start of the drift tube¹, l_{drift} is the length of the drift tube and c is the speed of light. l_{column} and l_{drift} can be obtained easily by the known geometry of the PEEM. The ToF spectrum can then be converted to kinetic energy by using eqns 3.4 and 3.6 and taking into account the time offset t_0 given by eqn 3.7. Third, a bias voltage U_{bias} can be applied to the sample and scanned over a desired range while recording the position of the ToF peak (or any other point of interest within the ToF spectrum) as a function of the kinetic energy [146–148]. Here, the kinetic energy of the photoelectrons is given by $E_{\text{kin}} = E_{\text{phot}} - \phi + eU_{\text{bias}}$, E_{phot} and ϕ being the photon energy and the sample’s work function, respectively. This method is more precise, since it considers the actual electric potential and trajectories of the electrons inside the PEEM. It should be noted that this calibration is only valid for the corresponding PEEM parameter settings and changing the voltages of the PEEM lens system will therefore require a new calibration. An example of such an energy calibration carried out with a pulsed diode laser of a central wavelength of 405 nm and a pulse duration of 60 ps is demonstrated in fig. 3.3. The measurement was performed on a polycrystalline gold surface under an extractor voltage of 22 kV and using a drift tube voltage of 40 V. In this case, the sample potential was scanned over a range of 3 V with a step size of 0.6 V. Fig. 3.3 (a) shows the half-maximum of the low-energy edge from the ToF spectrum as a function of the kinetic energy, yielding a calibration curve which then can be used for converting an arbitrary ToF spectrum into energy. The low-energy edge of the ToF spectrum is chosen as a reference point for the energy calibration, since it denotes electrons with a kinetic energy of 0 eV [149]. This method is suitable for absolute energy calibration if the spectrum is lacking well-known features for spectral referencing, such as the Fermi edge or other absorption edges. For the narrow energy range used here (3 eV), a linear fit is suitable to approximate the relation between ToF and energy, as shown in fig. 3.3 (a). Using the fitted slope (-1.48 eV/ns) and intercept (23.41 ns), the ToF spectrum can be converted into energy as displayed in fig. 3.3 (b). Nevertheless, for

¹Note that the drift time in the column is essentially energy-independent for electrons if an excitation source of low photon energy is used which results in a negligible temporal dispersion of the electrons.

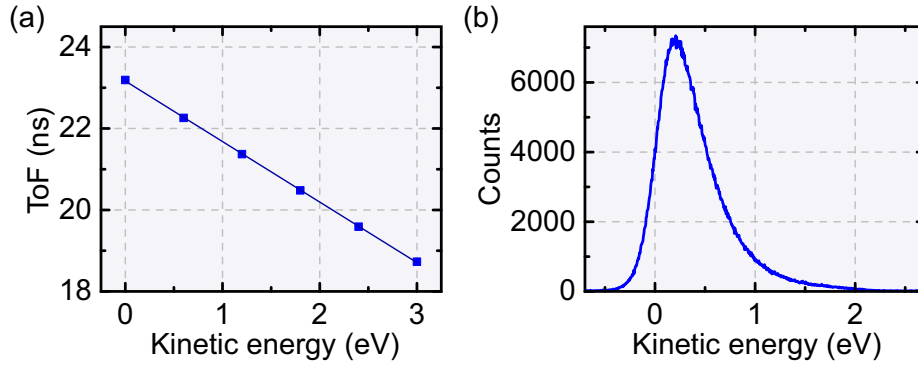


Figure 3.3: Energy calibration measurement of the ToF spectrometer using the potential scanning method. (a) ToF of the electrons as a function of the kinetic energy at the low-energy edge, given by the sample potential. The blue line shows a linear fit of the energy-dependent ToF spectra. (b) Converted energy spectrum based on the fitting parameters from the calibration curve shown in (a).

a broad energy spectrum, the relation between ToF and energy becomes nonlinear, as given by the classical equation of motion (see eqn 3.1):

$$t_{\text{ToF}} = l_{\text{drift}} \sqrt{\frac{m_e}{2E_{\text{kin}}}} + t_0. \quad (3.8)$$

Therefore, a suitable nonlinear fit must be used for the calibration curve to convert broadband energy spectra. Note that eqn 3.8 is a constant-potential approximation and does not account for acceleration and deceleration of the electrons when entering and leaving the drift tube. Thus, only this potential scanning calibration method provides a proper empirical relation between ToF and energy [148].

In addition, the electron counts need to be weighted by $dt(E)/dE$, so that the integrated counts within an interval of the energy spectrum are equal to the integrated counts within the corresponding interval of the ToF spectrum (conservation of differential counts). This is required particularly for a broad energy spectrum because of the nonlinear relation between the equidistant time intervals (ToF spectrum) and the corresponding non-equidistant energy intervals (energy spectrum).

3.1.3 Spatial and energy resolutions of the ToF-PEEM

The current state-of-the-art ToF-PEEM is able to reach a spatial resolution down to 20 nm [143]. The lateral resolution of our ToF-PEEM was determined in a threshold photoemission mode using UV excitation on a copper-coated microstructured silicon sample [31]. A contrast aperture of 70 μm was used for this test measurement. A line scan was performed across one edge of the microstructure, marked by the white

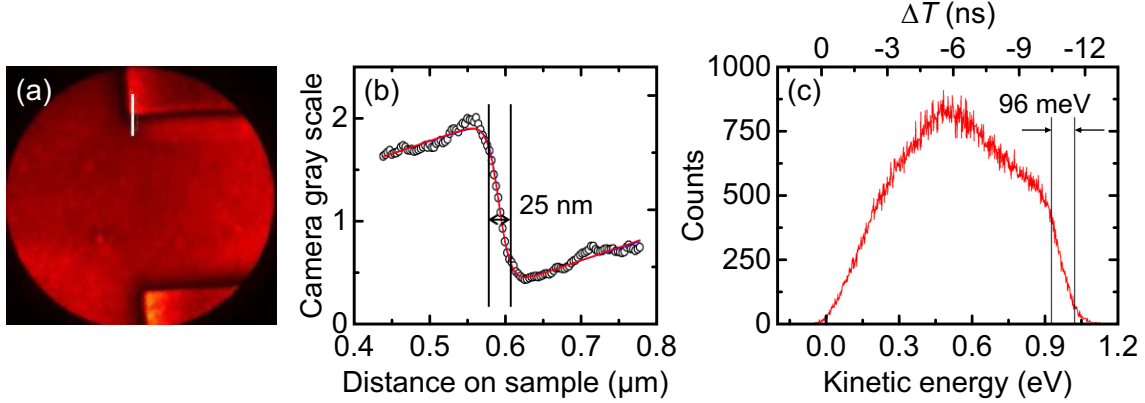


Figure 3.4: Spatial and energy resolution of our ToF-PEEM. (a) A PEEM image taken with a CCD camera on a microstructured copper sample upon UV excitation. A line scan (marked by a white line) across the microstructure edge is used for estimation of the spatial resolution. (b) The line profile from (a) yields a spatial resolution of ~ 25 nm, following a 16% – 84% criterion. (c) Measured energy width of the Fermi edge of ~ 96 meV obtained from a Mo(110) sample at room temperature. Figure taken from [31].

line in fig. 3.4 (a). Fig. 3.4 (b) shows the respective step profile from the line scan in fig. 3.4 (a). The edge slope width is determined to be ~ 25 nm following a 16% – 84% criterion error function fit. Hence, the spatial resolution of our ToF-PEEM is estimated to be at least 25 nm. However, the spatial resolution can be reduced to the range of 100 nm – 200 nm (refer to section 4.1) when employing a NIR or XUV source, mainly due to chromatic aberrations.

The resolution of a spectrometer is of vital importance for resolving the fine spectral details in an experiment. Technically, two limiting factors determine the energy resolution of a ToF spectrometer: i) the ripple of the drift voltage power supply ΔU_{ripple} and ii) the time resolution Δt_{res} of the DLD. The time resolution can be converted into an energy resolution by the following dispersion relation:

$$\Delta E_{\text{res}} = \frac{dE_{\text{kin}}}{dt} \Delta t_{\text{res}}, \quad (3.9)$$

where dE_{kin}/dt is the time derivative of the kinetic energy of the electrons. Using eqn 3.9, the technical energy resolution of the ToF spectrometer follows by addition in quadrature:

$$\Delta E_{\text{technical}} = \sqrt{(e\Delta U_{\text{ripple}})^2 + \left(\frac{dE_{\text{kin}}}{dt} \Delta t_{\text{res}}\right)^2}. \quad (3.10)$$

In our case, the ripple of the drift voltage, ΔU_{ripple} , is smaller than 20 mV, the DLD's Δt_{res} is better than 0.3 ns, and the energy dispersion dE_{kin}/dt at the Fermi edge

is 94 meV/ns (courtesy of FOCUS GmbH), yielding a resulting energy resolution of $\Delta E_{\text{technical}} = 35$ meV. However, the actual energy resolution of a spectrometer can be slightly worse due to systematic errors in the DLD electronics and broadening effects inside the PEEM. The ToF spectrometer resolution can be directly determined by measuring the width of a well-known Fermi edge and comparing it with the corresponding thermally broadened Fermi-Dirac distribution. The measured energy resolution, $\Delta E_{\text{measured}}$, is then obtained by deconvolution:

$$\Delta E_{\text{measured}} = \sqrt{\Delta E_{F(\text{measured})}^2 - \Delta E_F^2}, \quad (3.11)$$

where $\Delta E_{F(\text{measured})}$ and ΔE_F are the measured and calculated widths of the Fermi edge, respectively. Fig. 3.4(c) displays the ToF spectrum obtained by illuminating a molybdenum single-crystal, Mo(110), with a 405 nm picosecond pulsed diode laser. The drift voltage used was 10 V which is the lowest practical drift voltage to obtain the highest temporal dispersion without deteriorating the spatial resolution. By taking the energy width between the 16% – 84% level of the Fermi edge slope from the molybdenum surface, $\Delta E_{F(\text{measured})}$ is determined to be 96 meV at room temperature (295 K). The thermal broadening at a finite temperature T is provided by the first derivative of the Fermi-Dirac distribution [150]:

$$f(E) = \frac{1}{e^{\frac{E-E_F}{k_B T}} + 1}, \quad (3.12)$$

where E_F is the Fermi energy and k_B the Boltzmann constant. Following the 16% – 84% criterion, the energy width of the Fermi edge results as

$$\Delta E_F = 3.32k_B T, \quad (3.13)$$

corresponding to $\Delta E_F = 84.4$ meV at 295 K room temperature. Using eqn 3.11, the measured ToF spectrometer resolution is determined as $\Delta E_{\text{measured}} = 46$ meV [31]. This result agrees quite well with the technical estimation mentioned above, considering the fact that $\Delta E_{\text{technical}} = 35$ meV does not include all resolution broadening contributions, thus being a lower limit. It is noteworthy to mention that a more proper determination of the energy resolution can be performed by measuring the Fermi edge of polycrystalline samples at the lowest possible temperature. This is due to the fact that all direct transitions between the electronic levels are averaged out in polycrystalline samples, while in single-crystalline samples a distortion due to electronic levels crossing the Fermi level can arise [151].

3.2 Atto-PEEM

Initiated by the theoretical proposal of M. I. Stockman *et al.* [117], we first began the atto-PEEM experiment using attosecond XUV pulses from HHG as a light source for the PEEM without a pump-probe scheme yet. The atto-PEEM experiment was carried out at the AS-5 beamline at the Max Planck Institute of Quantum Optics (MPQ). The following section describes the HHG setup based on a commercial chirped-pulse amplification (CPA) laser system (Femtopower Compact Pro, Femtolasers Produktions GmbH) used in this work. A brief description of the static atto-PEEM experimental layout is also given.

3.2.1 1 kHz few-cycle laser system

The key components of the laser system used at the AS-5 are outlined in fig. 3.5. The 1 kHz CPA laser system at the AS-5 beamline is shared with the Petawatt Field Synthesizer group, where it is primarily used for developing petawatt-scale CEP-controlled few-cycle laser pulses for ultrahigh-field applications [152, 153]. The beamline begins with a Kerr-lens mode-locked Ti:sapphire oscillator pumped by a diode-pumped solid-state laser, generating seed pulses of 750 nm, 3.5 nJ and 7 fs at a repetition rate of 70 MHz [154]. The seed pulses are stretched to a pulse duration of 10 ps by a SF-57 glass stretcher before entering the CPA stage [154]. Additionally, the higher-order dispersion of the oscillator output is fine-tuned by an acousto-optic programmable dispersive filter (Fastlite DAZZLER). After amplification by 10 consecutive passes through a Ti:sapphire amplifier crystal pumped by a Q-switched, frequency doubled, diode-pumped solid-state Nd:YAG laser (Etna, Thales Laser), the laser pulse energy reaches ~ 2 mJ with a central wavelength of 800 nm and a pulse duration of 2 ps (see fig. 3.5) [154]. A Pockels cell and a Glan-Thompson prism are used to reduce the laser's repetition rate to 1 kHz before the amplifier and the beam is further divided into two parts of lower repetition rate for simultaneous operation of the Petawatt Field Synthesizer and AS-5. From here the laser beam is guided to the experimental laboratory which is situated on the floor below. The laser beam now enters a hybrid pulse compressor which consists of a paired double-prism compressor and a set of 16 high-dispersive mirrors. More details can be found in [155]. This final compression step of the pulses results in a Fourier transform-limited pulse duration of 26 fs FWHM with a pulse energy of 1.4 mJ [154]. A commercial beam lock system compensates the thermal and mechanical drift of the laser beam before it passes into the final compressor stage.

To achieve the broadband spectra required for few-cycle pulses, the laser beam is focused into a 1 m long hollow-core fiber (HCF) filled with neon gas of a static pressure of 2.8 bar – 3 bar [154] for spectral broadening. A second beam lock system

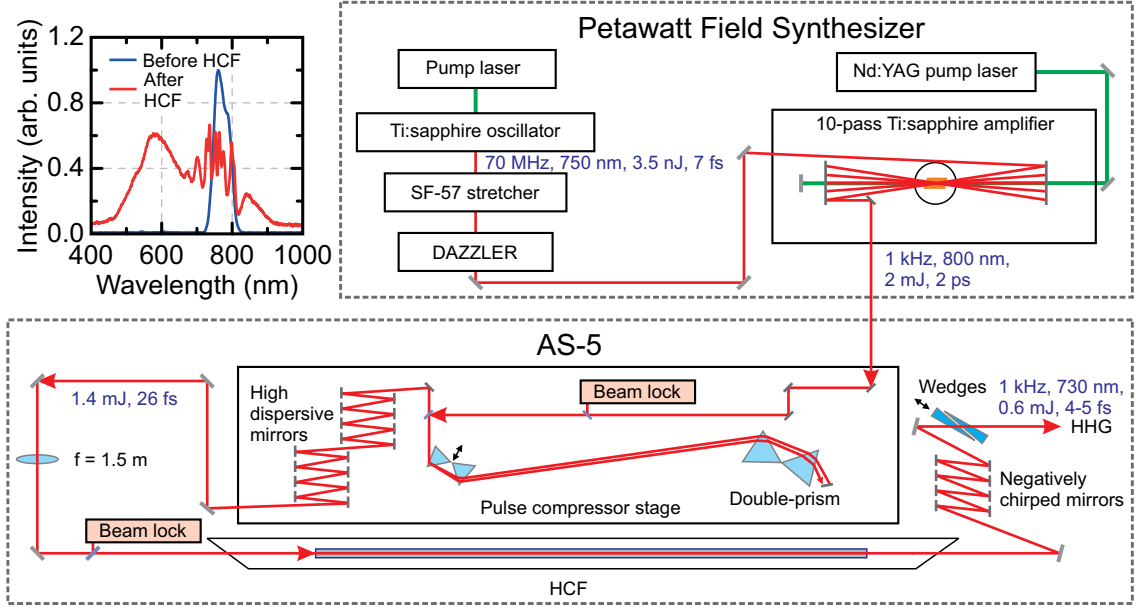


Figure 3.5: Schematic overview of the AS-5 laser system at MPQ. The laser pulses produced by the 1 kHz CPA laser system from the Petawatt Field Synthesizer are first compressed by a pair of double-prisms in combination with a set of high-dispersive mirrors. The second step of pulse compression is completed by the typical spectral broadening in a HCF accompanied by negatively chirped mirrors in order to achieve few-cycle laser pulse duration. The inset illustrates the spectrum before and after the HCF; figure adapted from [154].

stabilizes the laser beam position at the fiber entrance. It is worth noting that the use of noble gases in the HCF advances pulse compression to high energies (sub-millijoule energy range), owing to the high damage threshold of these gases [156, 157]. The intense laser beam propagates through the gas in the fiber and induces white light or supercontinuum generation primarily due to self-phase modulation resulting from the nonlinear Kerr effect. In other words, when an ultrashort laser pulse propagates in a medium, it changes the refractive index of the medium, thus producing a phase shift in the pulse and consequently leading to a frequency sweep within the pulse envelope. The linear relation between the refractive index change, $\Delta n(t)$, and gas pressure, p , in the HCF is given by [158]:

$$\Delta n(t) = n_2 I(t) = p \psi_2 I(t), \quad (3.14)$$

where n_2 is the nonlinear refractive index, $I(t)$ the laser intensity and ψ_2 the nonlinear refractive index per unit pressure. Self-steepening, in addition to the self-phase modulation, also contributes to the formation of very broadband pulses due to the intensity dependence of the group velocity along its direction of propagation (the group velocity at the pulse peak is slower than that of the trailing edge). This leads

to an asymmetric spectrum where the blue side is more extended (see fig. 3.5) as the trailing part of the pulse is steeper than the leading one. The HCF pulses are now positively chirped and the positive dispersion can be compensated by a set of broadband negatively chirped mirrors designed and manufactured at Ludwig Maximilians University of Munich (LMU). 4 to 8 pairs of chirped mirrors are used for dispersion control depending on the amount of positive dispersion in different experiments. These mirrors use two angles of reflection, 5° and 19° , to achieve an optimized phase contrast ensuring a homogeneous group delay dispersion. Fine tuning of the laser pulse length is managed by a pair of fused silica glass wedges. The typical HCF output spectrum after the chirped mirror compression at AS-5 is shown in fig. 3.5 and the resulting pulse energy is $\sim 600 \mu\text{J}$. The spectrum spans over a full octave from 450 nm to 1000 nm [154] and its Fourier transform-limited pulse duration is below 3 fs FWHM, well within the few-cycle regime.

3.2.2 1 kHz HHG source

The AS-5 beamline for the atto-PEEM experimental campaign is illustrated in fig. 3.6. The first part of the AS-5 beamline covering the 1 kHz laser system for producing few-cycle laser pulses has already been presented in subsection 3.2.1. Here, the second part of AS-5 beamline for HHG is described. Briefly, the second part of the AS-5 beamline consists of four essential components: HHG chamber, beam diagnostic chamber, filter chamber and experimental chamber. The intense few-cycle laser beam enters the HHG chamber through a fused silica Brewster window where the loss of the p-polarized laser intensity is minimized to almost zero. High harmonic radiation is generated by focusing the laser pulses with a concave spherical silver mirror of a focal length of 50 cm onto a 3 mm diameter nickel tube filled with a neon gas target. The physics of HHG has been described in subsection 2.1.2. The nickel tube is mounted on translation stages for precise laser beam positioning. The laser focus diameter is approximately $150 \mu\text{m}$, which is of about the same size as the laser-drilled hole in the tube. The neon gas pressure is kept between 150 mbar and 200 mbar for optimal XUV generation. Neon is chosen as the gas target since it exhibits an optimal combination between ionization potential and absorption cross-section for high harmonic emission of isolated pulses in the energy range of 70 eV – 130 eV [159]. The gas load emerging from the tube is continuously pumped away by a turbomolecular pump to maintain a pressure below 10^{-3} mbar in order to ensure a minimal re-absorption of the XUV radiation and a rather good vacuum in the first pumping stage.

Both the broadband NIR beam and XUV beam propagate collinearly into the diagnostic chamber after passing the differential pumping stages. The latter serve as

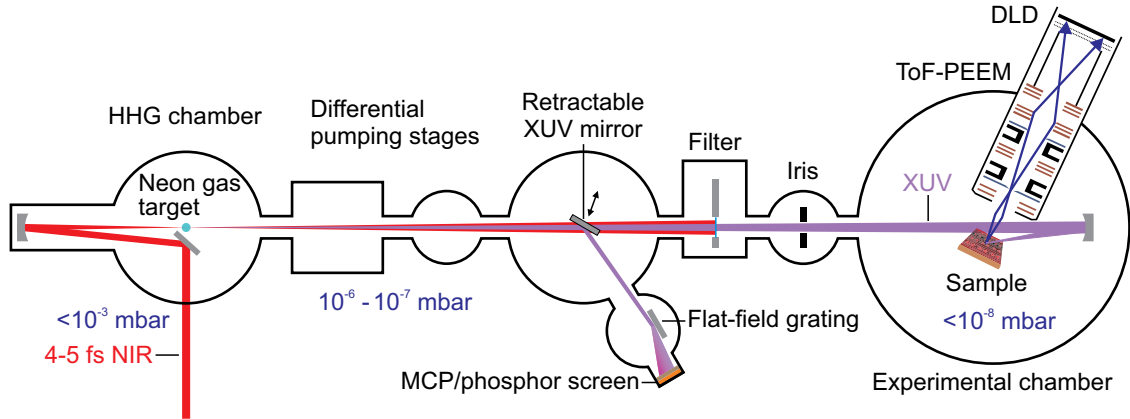


Figure 3.6: Schematic overview of the AS-5 beamline at MPQ for the atto-PEEM experiments. The XUV pulses are generated in the HHG chamber by focusing the NIR laser pulses onto a gas target. Both NIR and XUV pulses propagate collinearly into the diagnostic chamber for XUV beam characterization. The NIR beam is blocked in the filter chamber while the XUV beam transmits through and enters into the experimental chamber. An iris is used to adjust the XUV intensity. The vacuum condition inside the beamline is maintained by continuous pumping with turbomolecular pumps backed by rough pumps.

an intermediate stage to reduce the gas load from the HHG chamber down to a pressure range of 10^{-6} mbar – 10^{-7} mbar before reaching the experimental chamber. In the atto-PEEM experiments, only XUV pulses were used since a NIR-pump/XUV-probe setup was not intended at that phase. At the diagnostic chamber, the beam profile and the spectrum of the XUV radiation are monitored. Gold-palladium mirrors can be inserted into the beam path to either reflect the XUV beam directly onto a MCP/phosphor screen or to reflect the beam onto a flat-field grating at grazing incidence which disperses the beam spectrally on the MCP/phosphor screen. A CCD camera connected to a PC is used for recording the optical data from the phosphor screen. To avoid saturation of the imaging devices caused by low-order harmonics and intense NIR light, a 800 nm thick zirconium filter is placed in front of the MCP/phosphor screen. The XUV spectrometer is calibrated using additional filters inserted into the beam path to provide spectral information for HHG optimization [154]. At the filter chamber, the NIR beam is blocked completely by using different filters such as zirconium or silicon nitride mounted on a filter wheel, depending on the requirement of the experiments, thus only the XUV beam is transmitted through the filter section. The XUV intensity can then be adjusted by a motorized iris behind the filter section.

In the experimental chamber, the XUV beam is focused by a concave spherical XUV mirror ($f = 12.5$ cm) onto the sample situated in the PEEM. The mirror assembly can be moved in all three dimensions to align the XUV focus onto the

sample. Photoelectrons emitted from the sample surface upon XUV excitation are spatially and energetically detected by the PEEM in combination with a DLD. In addition, a Hg arc UV lamp emitting unpolarized continuous-wave light with a cutoff energy of 4.9 eV is used as a standard UV excitation source for sample imaging. This Hg lamp is mounted on another entrance port of the experimental chamber at an incidence angle of 65° to the sample. A detailed description of the PEEM design and working principle can be found in section 3.1.

3.3 CEP-tagged PEEM

For CEP control on plasmonic systems we used a phase tagging technique by means of a stereographic above-threshold ionization (ATI) phase meter instead of a phase-stabilized laser system in order to retrieve CEP information for every laser shot. This work includes the novel development of CEP-tagged PEEM and the exploration of CEP control on metallic nanostructures and bulk tungsten by using PEEM. The CEP-tagged PEEM was performed using the 10 kHz laser system at LMU. The work on CEP-tagged PEEM is a parallel research effort along with atto-PEEM, which paves the path towards the visualization of spatiotemporal dynamics with nanometer spatial and attosecond temporal resolution.

3.3.1 10 kHz few-cycle laser system

At the LMU beamline, the 10 kHz few-cycle laser generation and operation in principle are very similar to the 1 kHz few-cycle laser system at AS-5, MPQ (cf. subsection 3.2.1), with several differing details. The 10 kHz laser infrastructure at LMU is illustrated in fig. 3.7. Here, the seed pulses from a 80-MHz oscillator are amplified for 9 consecutive passes through a Ti:sapphire crystal. The amplifier output is compressed by a grating compressor, since gratings provide a much larger negative dispersion compared to a prism compressor. Hence, an additional set of high dispersive mirrors is not needed for the pulse compression. This results in compressed pulses with a pulse energy of $400 \mu\text{J} - 600 \mu\text{J}$ and a pulse duration of 27 fs FWHM. A higher repetition rate, 10 kHz in this case, comes at the expense of lower pulse energy, therefore ~ 0.7 bar of argon gas is used in the HCF to achieve few-cycle laser pulse duration. Argon gas exhibits strong enough nonlinearity at a moderate focused laser intensity and gas density (≤ 1 bar). A throughput of $130 \mu\text{J} - 180 \mu\text{J}$ can be achieved after the HCF and negatively-chirped mirrors depending on the focusing parameters at the entrance of the fiber and gas pressure. The laser pulses are characterized by a spectrometer and an autocorrelator for laser alignment and

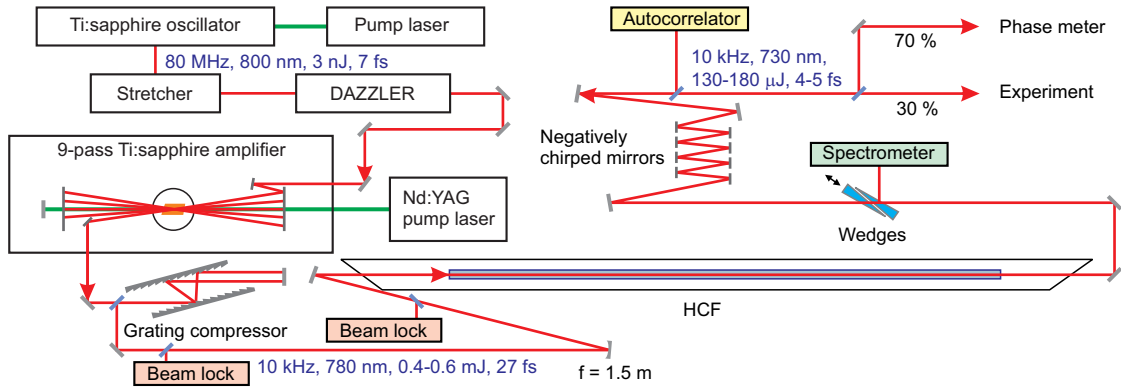


Figure 3.7: 10 kHz laser infrastructure at LMU. See text for details.

optimization. A broadband beam splitter directs 70% of the laser beam to the phase meter and the remaining laser beam to the PEEM experiment, respectively.

3.3.2 ATI phase meter

Conventional active CEP stabilization of the laser [160–162] has been demonstrated as a well-established technique to control the electron dynamics in matter by scanning the CEP of the phase-stabilized laser pulses. Recently, an improved CEP stabilization technique via a feed forward method [163] has greatly increased the stability of continuous locking from several hours [164, 165] to more than ten hours [58]. Alternatively, single-shot phase tagging is a promising new approach for CEP-resolved experiments, as it entirely omits the need for active CEP stabilization. Phase tagging uses a stereographic ATI phase meter [166–168] to measure the CEP of every laser shot at kHz repetition rates. The concept and design of the ATI phase meter was pioneered by G. G. Paulus *et al.* [50, 169, 170]. This technique offers several advantages over conventional CEP stabilization such as permitting real-time determination of the CEP for every laser shot and continuous real-time monitoring of the laser performance. It also allows for long data acquisition times over several hours and even over more than ten hours with a drift correction scheme [171]. Moreover, this technique enables parallel data acquisition for all CEPs within a certain measurement time, which evenly distributes any possible dynamic changes during the measurement, e.g. sample drift, over all CEP values [172]. In contrast, CEP locking requires a serial scan, where drift of the experimental parameters correlates with the scanned CEP, leading to systematic errors.

The CEP detection relies on the asymmetric electron emission during strong-field ionization of noble gases by linearly polarized few-cycle laser pulses. Typically, the few-cycle laser pulses are focused onto a xenon gas target at a peak intensity of

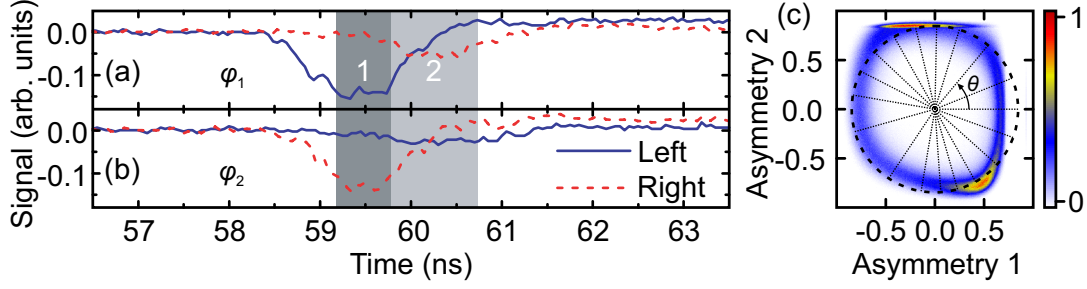


Figure 3.8: Working principle of a single-shot stereographic ATI phase meter. (a) and (b) Single-shot ToF traces from the left and right MCPs of the phase meter for two laser shots with different CEPs, φ_1 and φ_2 . Light and dark shaded areas indicate the integration regions, 1 and 2, for determining A_1 and A_2 , respectively (see eqn 3.15). Figure adapted from [164]. (c) A typical PAP for 10^6 sub-5 fs laser pulses. The dotted radial lines denote 18 segments of the PAP with an equal number of counts, corresponding to equidistant CEP intervals of 20° size. The color scale shows the relative counts.

$\sim 8 \cdot 10^{13} \text{ W/cm}^2$ [168]. ATI electrons, i.e. direct electrons and rescattered electrons, are emitted from the xenon atoms and fly towards opposing ToF detectors. The direct electrons of low kinetic energy are suppressed by applying a repelling static voltage to a mesh in front of the MCP at each detector. In the meantime, two ToF spectra of the CEP-sensitive rescattered electrons with high kinetic energy are recorded at both left and right detectors placed along the polarization axis of the focused laser beam. These ATI electron spectra are detected as time-dependent electron currents and are converted into time-dependent voltages. In order to retrieve the CEP in real-time from the ToF spectra, two properly adjusted gated integration windows, labeled 1 and 2, respectively, are applied to the ToF spectra for each laser shot. Two asymmetry values can be calculated using an electronic circuit:

$$A_{1,2} = \frac{L_{1,2} - R_{1,2}}{L_{1,2} + R_{1,2}}, \quad (3.15)$$

where L and R are the integrated electron yields of the left and right MCP detectors, respectively. These asymmetries are then output as analog voltages, which are proportional to the respective asymmetry values, for data acquisition. Next, a parametric asymmetry plot (PAP) of A_1 and A_2 can be generated, in which the polar angle, $\theta = \arctan(A_1/A_2)$, corresponds to the CEP, φ , of the laser pulse via the relation $\theta = \varphi + \varphi_0$ [173], where φ_0 is an arbitrary offset, since the CEP is randomly and uniformly distributed for our laser system. Hence, the CEP φ of each laser shot can be determined directly from the PAP polar angle θ , except for a constant offset, as long as the measured PAP constitutes a uniform distribution as a function of polar angle. The asymmetry values are recorded simultaneously with the

DLD photoelectron counts, therefore enabling phase tagging of every detected event in the experiment. Fig. 3.8 (a) and (b) depict typical ToF spectra from the left and right detectors of the ATI phase meter for two laser shots with different CEPs. The light and dark shaded areas indicate the gated regions (high and low energy) for retrieving the two asymmetry values, A_1 and A_2 , respectively. Since the asymmetry values are highly sensitive to the pulse duration of the few-cycle laser pulses and the CEP, the PAP can also be used to deduce the laser pulse duration. An empirical relationship between the pulse duration and the radius of the PAP is demonstrated by A.M. Saylor *et al.* [167], using pulse duration calibration with spectral-phase interferometry for direct electric-field reconstruction. The FWHM pulse duration, Δt , as a function of the radius r of the PAP is therefore

$$\Delta t = \beta + \sqrt{\frac{-\alpha}{\ln(1-r)}}, \quad (3.16)$$

where $\beta = (1.6063 \pm 0.2593)$ fs and $\alpha = (9.7317 \pm 1.5069)$ fs², are fitting parameters. A bigger diameter of the PAP implies a shorter pulse duration. Fig. 3.8 (c) displays a typical PAP with a pulse duration of 4.13 fs FWHM and its corresponding radius, $r = 0.78$. Note that the measured PAP in fig. 3.8 (c) is clearly not a uniform distribution over the polar angle, i.e. the counts at certain polar angles appear more frequently than the others. This is due to systematic errors in the stereographic ATI phase meter, e.g. non-ideal integration windows or nonlinearities in the MCP detectors, which results in a bias towards certain polar angles. Since the laser's CEP is uniformly distributed, the measured PAP needs to be balanced in order to retrieve the actual CEP. This is done by splitting the PAP into a certain number of equidistant polar angle bins (for example, 18 bins of 20° size each) and subsequently adjusting the boundaries between the bins such that every bin contains the same number of counts (indicated by the radial dotted lines in fig. 3.8 (c)). The mapping between the redistributed bins and the original bins can then be used to retrieve the actual CEP from a measured PAP polar angle (except for a constant offset) for a non-uniform PAP measurement.

3.3.3 Single-shot CEP-tagged PEEM

In this subsection, the combination of single-shot ToF-PEEM with a stereographic ATI phase meter for studying the CEP control on plasmonic nanostructures is described. The setup of single-shot phase-tagged ToF-PEEM is schematically illustrated in fig. 3.9. One part of the few-cycle laser pulses, containing 70% of the 160 μ J pulse energy (see fig. 3.7), is focused onto a xenon gas target inside the ATI phase meter using a 25 cm focal length spherical mirror, while the remaining part

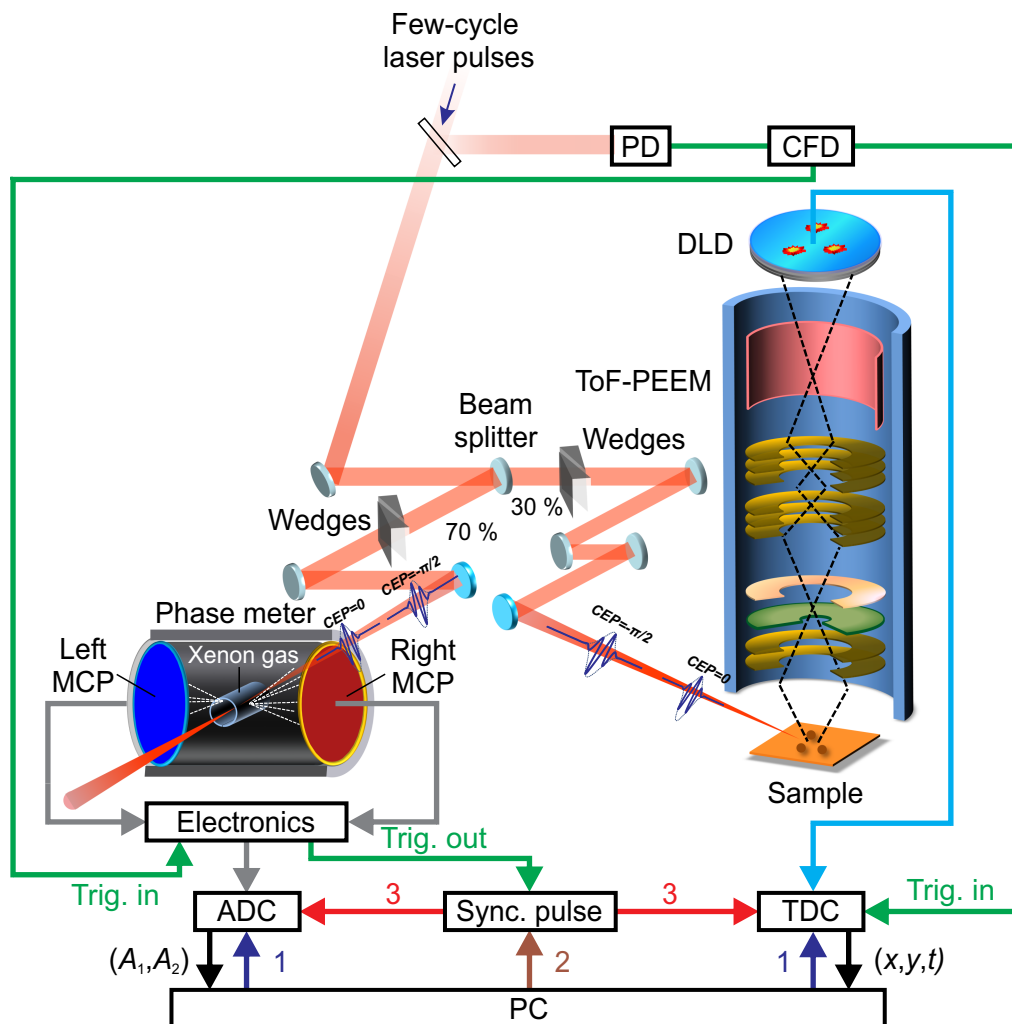


Figure 3.9: Single-shot CEP-tagged PEEM setup used for this work. A beam splitter separates the few-cycle laser beam into two paths. The first beam is focused by a 25 cm spherical mirror into the ATI phase meter containing a xenon gas target; at the same time the second beam is focused onto a sample inside the ToF-PEEM. Both the ToF-PEEM and the phase meter are synchronized to the broadband laser to enable simultaneous data acquisition. The laser trigger signal for synchronization is first obtained with a photodiode (PD) and transformed by a constant fraction discriminator (CFD) before being fed into the TDC and the phase meter's electronics, respectively. The master trigger to start the acquisition of both the ADC and TDC is controlled by a PC. See text for details on the acquisition synchronization.

is directed into the ToF-PEEM chamber. Individual pairs of fused silica wedges are used in both beam paths to correct for residual chirp in order to ensure shortest pulses, and irises are used to vary the laser intensity in both instruments.

The DLD is solely used instead of the fluorescence screen and CCD camera for the CEP-tagged experiments for two main reasons: first, the DLD is capable of syn-

chronized single-shot data acquisition, which is essential for phase tagging of every laser-triggered event. Second, the DLD has a superior signal-to-noise ratio [144], which enables background-free detection at low count rates, since low laser intensity is used in order to suppress space charge effects. To implement single-shot phase-tagged data acquisition, the commercial TDC of the DLD has been modified with a custom firmware, which assigns an absolute laser shot tag number for a particular exposure to each detected electron count [172]. This is necessary to maintain a correlation between the DLD and phase meter measurements because of the statistical nature of the DLD detection, which can result in multiple or zero electron detections per laser pulse, while the phase meter provides exactly one measurement per laser pulse. An analog/digital converter (ADC) is used to acquire the asymmetry values (A_1, A_2) from the phase meter. For starting an exposure, both the ADC and TDC are set to a hardware-triggered acquisition mode via a PC (labeled as 1 in fig. 3.9). In order to ensure synchronized acquisition, both devices are configured to start the actual data acquisition only upon an external synchronization pulse, once they are set to the acquisition mode, which is also issued by the PC after a short delay (ca. 100 ms), which makes sure that both devices are ready (labeled as 2). This pulse itself is synchronized with the laser via a hardware trigger, because it is issued upon the arrival of the next laser pulse, the according laser trigger signal being obtained via a photodiode. Thus, the data acquisition of the asymmetry values (A_1, A_2) at the ADC and the DLD data (x, y, t) at the TDC are both started simultaneously at a well-defined time with respect to the laser pulse train (labeled as 3). The subsequent single-shot acquisition during an exposure is clocked by the 10 kHz laser's repetition rate via the same photodiode, providing a trigger for both devices. A constant fraction discriminator is employed to transform the electrical pulses from the photodiode into transistor-transistor logic pulses suitable for the TDC as the start trigger input. The same transistor-transistor logic pulses are also used to trigger the phase meter. The data acquisition software then combines both measurements into a single data stream of asymmetry and DLD values (A_1, A_2, x, y, t) for each registered electron count at the DLD using the laser tag number of the particular electron count from the TDC to assign the corresponding asymmetry values of the respective laser shot from the phase meter data. By this procedure the asymmetry values from the phase meter are synchronized with the DLD data from the PEEM for every laser shot within an exposure, regardless of multi-events or missing events at the DLD. In chapter 6, another measurement parameter, which is the single-shot laser intensity, is added to our CEP-tagged PEEM in order to correct for an artefact which arises from laser intensity fluctuations. Further details about this intensity tagging can be found in section 6.1.

3.4 Plasmonic samples

High-definition and reproducible plasmonic nanostructures require well-developed fabrication techniques. The micro- and nanostructured samples investigated in this work were fabricated with chemical synthesis and nanolithography using an electron beam.

3.4.1 Chemical synthesis of NPOP

The NPOP samples used for this work were fabricated by F. Schertz from University of Mainz. More details of the NPOP preparation and characterization can be found in [127, 174–176]. NPOP was used as the first sample for CEP-tagged experiments since it exhibits a very strong field enhancement when in resonance, giving rise to a higher photoemission signal for detection and CEP-resolved data analysis (see section 5.1). The sample fabrication procedure is described in the following. A Si(100) substrate was deposited with 1 nm of chromium as an adhesive layer and then with a 50 nm gold film by thermal evaporation. Next, the sample was immersed into a cysteamine (organic molecule) solution and a self-assembled monolayer was formed after ~ 17 h on the gold surface. The gold nanoparticles (~ 90 nm average diameter) synthesis was achieved using a method reported by G. Frens [177].

In brief, a 100 ml aqueous solution containing 0.25 mmol/L of hydrogen tetrachloroaurate (III) trihydrate ($\text{HAuCl}_4 \cdot 3\text{H}_2\text{O}$, 99.995 %, Sigma-Aldrich) was heated under reflux and brought to boiling while stirring. Later, 2 ml of an aqueous solution of trisodium citrate dihydrate ($\text{HOC}(\text{CO}_2\text{Na})(\text{CH}_2\text{CO}_2\text{Na})_2 \cdot 2\text{H}_2\text{O}$, Sigma-Aldrich) was added quickly to the boiling solution. The mixture was then cooled down slowly to room temperature while stirring after maintaining the boiling for 10 min. A color change from black to dark red indicates the formation of gold nanoparticles as a result of nucleation and growth. In the last step, the prepared substrate was immersed in the freshly prepared colloidal gold suspension for ~ 5 min. This way, the gold nanoparticles became strongly immobilized by attaching to the cysteamine monolayer which serves as a spacer, creating a sub-nanometer gap between them and the gold plane to allow high field enhancement.

3.4.2 EBL

Electron beam lithography (EBL) has a significant advantage in resolution over conventional photolithography, since the resolution of the latter technique is constrained by the diffraction limit of the light used for the development of the photoresist. While EBL is capable of fabricating structure sizes down to a few nanometers, it also allows a large number of structures to be written in a reasonable time. It

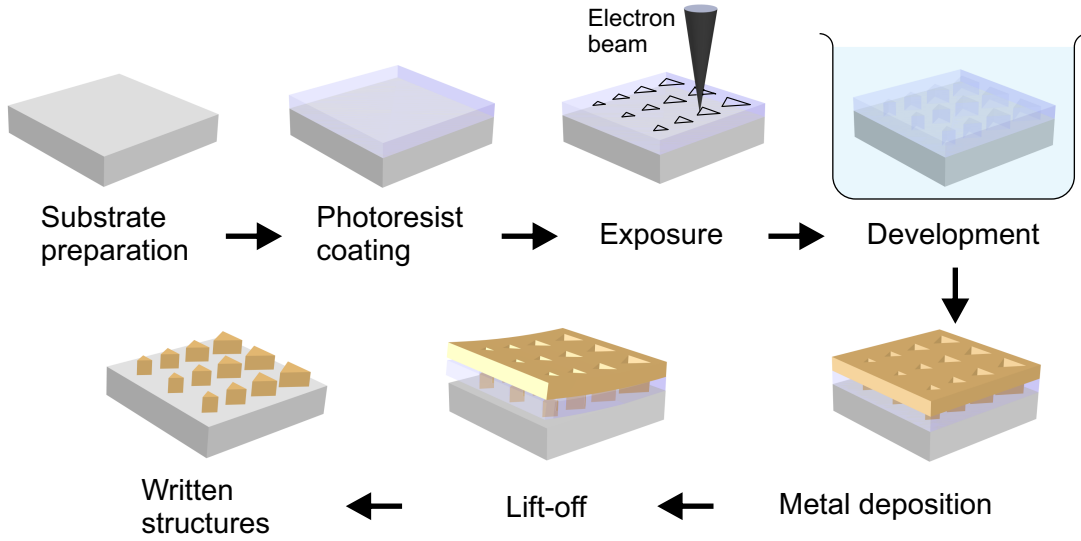


Figure 3.10: Schematic illustration of the fabrication steps required for the EBL technique. See text for details.

is therefore the technique of choice for achieving tailor-designed and well-defined metallic nanostructures that exhibit controlled surface plasmon resonances upon optical excitation. The samples investigated in this work were prepared by C. Späth from our group and by the Misawa group in the Research Institute for Electronic Science, Hokkaido University.

Fig. 3.10 illustrates the general fabrication procedure using this technique. As a first step, a conductive substrate such as silicon or indium-tin-oxide (ITO) coated glass is cleaned in an ultrasonic bath containing a solvent. Afterwards, the substrate is spin-coated with a positive or a negative photoresist to a thickness of 80 nm – 200 nm and then exposed to an electron beam that writes a given pattern, inducing a solubility change on the exposed area. In a subsequent solvent development, the exposed area with a positive photoresist is dissolved and removed whereas the exposed part with a negative resist is solidified and therefore remains on the sample. A thin metal film such as gold can be deposited via electron beam evaporation or magnetron sputtering onto the developed substrate in a high vacuum environment. The thickness of the metallic film is dependent on the requirements of the experiments and can be controlled by adjusting the deposition time. A polycrystalline metal film is obtained using such deposition methods. The final step is completed by a lift-off process, in which the remaining photoresist and its corresponding metal layer are removed using a solution depending on the photoresist type, resulting in the formation of metal nanostructures on the substrate. The nanofabrication carried out in our own group used a 30 kV EBL system (Raith 150) integrated with a scanning electron microscope (SEM), DSM 982 Gemini. To improve the nanofabrication

method, we also employed a two-layer photoresist method followed by EBL to reduce the likelihood that the evaporated metal nanostructures are removed during the lift-off process by creating undercuts in the photoresist [178]. Furthermore, the samples provided by the Misawa group were fabricated using a high-resolution 125 kV EBL system (Elionix ELS-F125, Tokyo, Japan). Nanostructures with a gap size of 6 nm have been fabricated by employing this high-resolution EBL system [179]. In some cases, EBL in combination with ion beam etching can be used to transfer the written structure onto a metal.

Towards atto-PEEM

This chapter reports the experimental implementation of the atto-PEEM concept and its challenges using a 1 kHz low-repetition-rate HHG source in our group. In this atto-PEEM setup, we investigated the ultimate spatial resolution of XUV imaging with attosecond pulses centered at 93 eV photon energy using lithographically fabricated gold structures. It is found that by employing energy-filtered imaging one could improve the spatial resolution of XUV imaging which is mainly reduced by chromatic aberrations due to the large energy bandwidth of XUV-generated photoelectrons. Space charge effects, a major issue affecting the imaging quality and the electron spectrum, as a result of using low-repetition-rate laser sources, are also studied. The discussion of the results in this chapter is based on [34, 138, 180].

4.1 XUV imaging with attosecond pulses

Following the described atto-PEEM concept (see subsection 2.3.2), we here experimentally carried out a series of XUV imaging using a low-repetition-rate (1 kHz) HHG source for PEEM with medium magnification. The details of the experimental setup are already presented in subsection 3.2.2. We used a mixture of isolated attosecond pulses and attosecond double-pulses for the experiments since the 1 kHz few-cycle laser system was not actively phase-stabilized (see subsection 2.1.2). A 150 nm zirconium filter and a 150 nm silicon nitride filter are used to block the collinear NIR beam while spectrally filter the XUV beam. The transmission curves of these metallic filters are displayed in fig. 4.1 (a). It should be noted that a zirconium filter permits a small percentage of XUV transmission at around 25 eV, therefore a silicon nitride filter of a narrow bandwidth is added to exclude these low-order harmonics. The resulting XUV spectrum peaks at 97 eV after being filtered by the zirconium and silicon nitride filters, as measured by an XUV flatfield

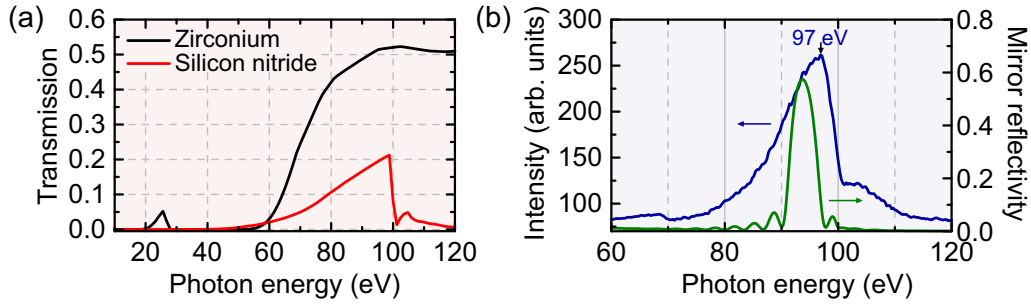


Figure 4.1: Spectral filters for XUV transmission. (a) Transmission curves of zirconium and silicon nitride filters, data taken from [181]. (b) XUV spectrum (blue curve) filtered by zirconium and silicon nitride filters and simulated XUV mirror's reflectivity (green curve) peaked at 93 eV with a bandwidth of 5.4 eV.

spectrograph (see fig. 4.1 (b)). The XUV beam is further spectrally filtered at around 93 eV and focused onto the sample in the ToF-PEEM by means of a concave Mo/Si multilayer mirror of 12.5 cm focal length. The 5.4 eV FWHM spectral bandwidth of the mirror reflectivity supports XUV pulses with a Fourier limit of 350 as. The XUV focus can be aligned onto the sample by using the NIR laser beam¹ as a guidance via the motorized XUV mirror assembly inside the ToF-PEEM chamber. The alignment is done using the low magnification mode in the PEEM. The XUV focal spot size on the sample is estimated to be in the range of 200 nm – 400 nm, indicated by the electron emission spot size in the PEEM.

The photoemitted electrons from the XUV pulses can be recorded either with a CCD camera placed after the PEEM's fluorescence screen or a DLD inserted in the PEEM column before the fluorescence screen (see section 3.1). Fig. 4.2 illustrates the comparison of image quality using a CCD camera and a DLD. The test sample used here consists of a thin layer of copper coated on a $10\ \mu\text{m} \times 10\ \mu\text{m}$ silicon grid which has a depth of 300 nm. A medium-sized backfocal contrast aperture of $150\ \mu\text{m}$ was used in the PEEM to allow sufficient electron transmission while minimizing the aberrations for improving the spatial resolution. The contrast aperture may also act as a low-pass energy filter thus decreasing the energy spread and transverse momentum spread of the electrons, allowing for higher resolution. Note that the PEEM voltage settings for both imaging devices (CCD camera and DLD) are comparable and a medium magnification mode was used. Fig. 4.2 (a) and (c) show the PEEM images of the copper grid sample acquired by a CCD and a DLD, respectively, upon excitation by a 4.9 eV Hg arc UV lamp. The required exposure time to obtain both images is within several minutes. In this case, the high image contrast is formed by surface topography of the sample, since the entire surface is covered by copper.

¹The NIR beam is used to generate the XUV radiation, therefore the two beams are superimposed and propagate collinearly.

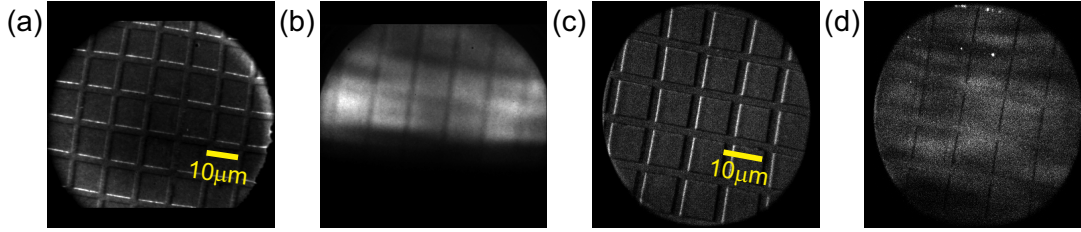


Figure 4.2: Comparison between PEEM imaging with a CCD and a DLD. (a) UV-PEEM image of a copper grid illuminated by an Hg arc lamp with an exposure time of 3 min, taken by a CCD camera. (b) XUV-PEEM image illuminated by attosecond XUV pulses under the same conditions as in (a) with an exposure time of 13 min, taken by a CCD camera. (c) UV-PEEM image of a copper grid illuminated by an Hg arc lamp with an exposure time of 1 min, taken by a DLD. (d) XUV-PEEM image illuminated by attosecond XUV pulses under the same conditions as in (c) with an exposure time of 1 h, taken by a DLD.

However, the image contrast of the PEEM image upon XUV excitation is notably degraded in the case of CCD acquisition (see fig. 4.2 (b)). The reduced contrast is caused by a broader electron energy spectrum induced by the 93 eV XUV pulses of 5.4 eV bandwidth. XUV contrast can be improved by using a smaller contrast aperture or applying an IEF to achieve a narrower electron energy spectrum, however at the expense of significantly lower transmission.

In addition, the XUV intensity has to be decreased substantially to reduce the space charge effect which causes image blurriness, hence a longer exposure time is required. A neon gas pressure of ~ 60 mbar is used to achieve such low XUV intensity for imaging using both the CCD camera and the DLD (see fig. 4.2 (b) and (d)). A detailed investigation of the space charge effect on the XUV imaging will be discussed in section 4.3. It should be noted that the XUV intensity was cut out at the bottom of the image possibly due to iris clipping and the inhomogeneous illumination could be caused by the structure of the metallic filter. It is found that an exposure time of more than 13 min using the CCD camera does not improve the spatial resolution anymore at such a low XUV intensity, as it starts to saturate. This issue can be resolved by switching from the CCD camera to the DLD for imaging. An improved XUV image contrast could be obtained with an exposure time of nearly 1 h using the DLD with negligible background, albeit with a great loss of intensity for suppressing the space charge effect. Both edges of the copper grid could be resolved using DLD imaging whereas only one blurred edge can be seen by CCD camera imaging. The comparison clearly demonstrates that the DLD intrinsically has a superior signal-to-noise ratio compared to the CCD camera that produces more electronic noise. This can be explained by two sources of dark noise [141], which are the MCP and the CCD in a conventional image intensifier that usually consists of a MCP, a phosphor screen and a CCD camera. In contrast, the noise originates only from the MCP in

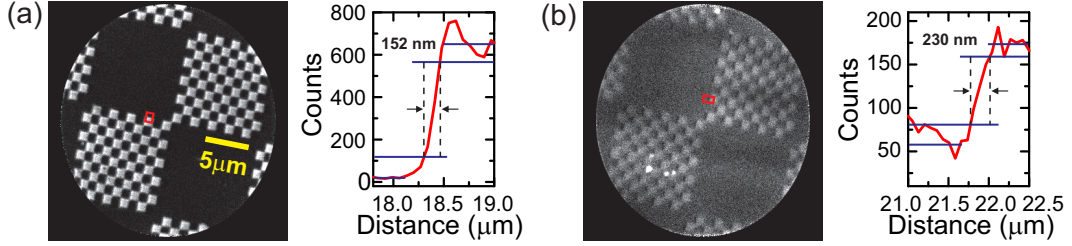


Figure 4.3: Spatial resolution estimation of the PEEM at medium magnification mode. (a) Left: UV-PEEM image of gold squares illuminated by an Hg arc lamp with an exposure time of 2 min; right: exemplary intensity profile extracted from the region marked on the left image yields a spatial resolution of 152 nm. (b) Left: XUV-PEEM image illuminated by attosecond XUV pulses under the same conditions with an exposure time of 1.5 h; right: exemplary intensity profile extracted from the region marked on the left image yields a spatial resolution of 230 nm.

the DLD imaging assembly, and only the portion of the MCP noise which is strong enough to produce a detectable current pulse inside the DLD wires contributes to the image noise.

Since PEEM imaging with a DLD can greatly improve the signal-to-noise ratio for long exposure times, the imaging capability using attosecond XUV pulses in our setup described here was tested only with a DLD. The sample used for resolution measurements consists of alternating $1\ \mu\text{m} \times 1\ \mu\text{m}$ gold squares on a silicon wafer substrate with native oxide coverage and was fabricated by EBL and ion beam etching. The gold layer has a thickness of 100 nm. A 15 nm thick chromium layer was added between the gold layer and the silicon substrate as an adhesion layer to improve the quality of the gold layer. In this series of PEEM imaging, a high drift voltage of 130 V was applied to the drift tube, thus improving image resolution at the expense of ToF resolution which was not required for this measurement. The extractor voltage of the PEEM objective lens was set to 20 kV (medium magnification mode) and a contrast aperture of $150\ \mu\text{m}$ was chosen. Fig. 4.3 (a) shows the PEEM image of the gold square sample excited by a 4.9 eV Hg arc UV lamp. The UV-PEEM image contrast arises from work function differences at the surface, with gold appearing bright due to its work function (4.4 eV [84]) being lower than the UV excitation energy (4.9 eV), while silicon dioxide appears dark due to its higher work function of 4.9 eV [182]. The spatial resolution is estimated by taking the intensity profile over the structure's edge region (averaging over the $1\ \mu\text{m}$ edge length) following a 16% – 84% criterion error function fit. By averaging five intensity profiles from different sample positions, a spatial resolution of (153 ± 10) nm is estimated for the UV-PEEM image. Fig. 4.3 (b) depicts the PEEM image of the same sample excited by attosecond XUV pulses of 93 eV photon energy. The estimated spatial resolution for the XUV-PEEM image is (194 ± 50) nm (average from five different sample po-

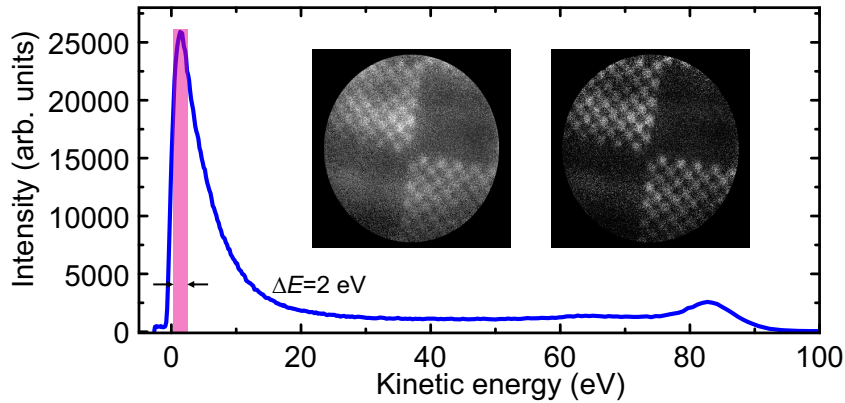


Figure 4.4: Full energy spectrum of XUV excited photoelectrons integrated over the whole gold square sample area as shown in the left inset. Left inset: energy-integrated image with XUV excitation over the full electron energy spectrum with an exposure time of 1.5 h. Right inset: energy-filtered image from 1 eV to 3 eV within the secondary electron peak.

sitions). The images are flat-field corrected for DLD gain. It should be pointed out that several hot spots on the sample indicated by the very bright areas in the XUV image are induced by nanoplasmonic fields due to NIR leakage through the pinholes of the filters. The inhomogeneous illumination on the sample by XUV excitation is mainly caused by the beam profile and filter structure. The XUV-PEEM image is typically of lower contrast in comparison to the UV-PEEM image, attributed to vanishing work function contrast and a broader electron energy spectrum for the 93 eV XUV excitation. The XUV pulse intensity was reduced by decreasing the neon gas pressure to avoid the space charge effect that causes image blurriness. This requirement currently limits the ability to achieve PEEM imaging in high-resolution mode where the transmission of photoelectrons is drastically decreased.

A ToF-PEEM allows for the distinction between the dominating secondary photoelectrons and the direct photoelectrons. In the next series of PEEM imaging, a low drift voltage of 40 V was applied to the drift tube in order to achieve decent energy resolution. The PEEM extractor voltage was set to 20 kV and the largest contrast aperture of 1500 μm was used in order to increase the transmission of high-energy photoelectrons. However, the PEEM resolution was now reduced due to spherical and chromatic aberrations of the objective lens as a consequence of using a larger contrast aperture size. Fig. 4.4 shows the electron energy spectrum excited by XUV which is spatially integrated over the whole sample area as depicted in the left inset. The spectrum, which is corrected for the work function difference between the sample surface and the drift tube, exhibits basically two peaks, one at low energy (secondary electrons or inelastically scattered electrons) and one at high energy (primary valence band electrons). The maximum detected kinetic energy (carried

by electrons at the Fermi edge) corresponds to the central XUV photon energy of 93 eV reduced by the material work function (4.4 eV for polycrystalline gold [84] and 4.9 eV for amorphous silicon dioxide [182]). By selecting a narrow energy interval ΔE , in this case from 1 eV to 3 eV within the secondary electron peak, the image contrast can be significantly enhanced due to a smaller energy spread, as illustrated in the right inset of fig. 4.4. However, using this ToF mode with the largest contrast aperture the spatial resolution is now degraded to ~ 300 nm as compared to ~ 200 nm when using a small contrast aperture and a limited ToF resolution. Energy-filtered imaging using only the high-energy valence band electrons at 83 eV can be performed similarly; however, gold and silicon dioxide show a very similar photoelectron yield at 93 eV photon energy excitation (see section below) and thus do not provide sufficient image contrast.

4.2 Microspectroscopic imaging

Besides filtering the PEEM images for different ranges of kinetic energies, electron ToF analysis utilizing a DLD has the potential for full-image microspectroscopy in XUV-PEEM, which was previously only feasible by illumination with synchrotron radiation. Conventionally, microspectroscopic data in XMCD-PEEM is obtained by scanning the photon energy for every recorded PEEM image [183, 184]. In comparison, a DLD takes advantage of its capability of three-dimensional dataset acquisition, allowing simultaneous lateral and energy distribution measurements of the photoelectrons. This is illustrated by selected micro-area spectra from a sample of gold ellipsoids fabricated on a native oxide covered silicon wafer by EBL and lift-off. The gold layer thickness is 20 nm and there is a 4 nm thin adhesion layer of chromium between the gold layer and the native oxide covered silicon wafer. This microspectroscopic data is obtained using attosecond XUV pulses of 93 eV photon energy, as described before. The UV-PEEM image (fig. 4.5 (a)) as well as the XUV-PEEM image (fig. 4.5 (b)) display the array of gold ellipsoids with three distinctly different intensity areas visible in the XUV-PEEM image: (i) a moderately bright intensity from the gold ellipsoids, (ii) a dark background from the native oxide covered silicon wafer surface, and (iii) very bright intensities observed at the rim of the gold frame and several gold ellipsoid areas. When defining these three different regions of interest (ROIs), as displayed by colored areas in fig. 4.5 (b), we obtain three different spectra representing these ROIs in fig. 4.5 (c). The gold spectrum shows a distinct secondary electron intensity at low kinetic energies and less intense photoemission from primary photoelectrons of the Au (5d) valence band of gold [185] below the Fermi edge at high kinetic energies. It should be pointed out that the fine structure of this Au (5d) valence band cannot be resolved due to the broad spectral band-

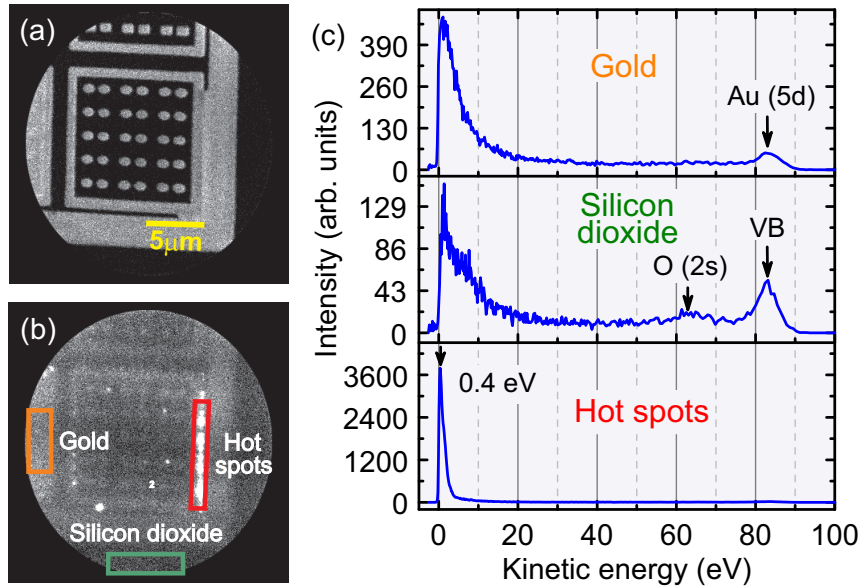


Figure 4.5: Microspectroscopic analysis of 500 nm gap gold ellipsoids coated on a native oxide covered silicon wafer imaged by a DLD. (a) UV-PEEM image of the sample illuminated by an Hg arc lamp with an exposure time of 5 min. (b) XUV-PEEM image illuminated by attosecond XUV pulses under the same conditions with an exposure time of 1 h. Three different regions (gold, silicon dioxide, and hot spots) on the sample are selected for microspectroscopy. (c) The corresponding kinetic energy spectra of the three marked ROIs shown in (b) with respective colors. VB: valence band.

width of the XUV pulses. Meanwhile, the emission from the native oxide covered silicon (also referred to as silicon dioxide) surface shows a smaller contribution of the secondary electrons compared to the gold due to a larger work function of silicon dioxide. The contrast in secondary electron emission between gold and silicon dioxide is mainly determining the observed image contrast in non-filtered PEEM imaging. At high kinetic energies, the emission possibly consists of a mixture of valence band electrons from both silicon dioxide and bulk silicon [186, 187]. Note that the high-energy emission intensities of both Au (5d) and silicon valence band electrons are very similar, which might prevent achieving PEEM image contrast in energy-filtered imaging around this energy range. This issue can be resolved by cleaning the sample surface to increase the photoemission yield from the Au (5d) valence band significantly compared to the photoemission yield from the substrate. Furthermore, some indication of photoemission from the O (2s) core level state is observed. Interestingly, the electron spectrum from the most intense PEEM image areas manifests as distinct and very intense emission of very low-energy electrons which may be attributed to photoemission from surface plasmon-assisted hot spots excited by leaking NIR laser radiation through the metallic filters. In conclusion,

this successful microspectroscopic identification of core and valence band electronic states with attosecond XUV pulses proves the capability of using a ToF-PEEM with a DLD to measure the changes of the electron's kinetic energy on the order of a few electronvolts as predicted in the atto-PEEM concept [117].

4.3 Space charge effects

Space charge effects in photoemission are frequently observed when using low-repetition-rate ultrashort laser pulse systems of pulse durations ranging from femtoseconds to attoseconds [35, 188, 189]. A detailed analysis of the influence of space charge due to the very short attosecond XUV pulses (1 kHz HHG source) on the PEEM image quality as well as the resulting photoelectron spectra was performed by means of ToF spectroscopic measurements at different illumination intensities. Optimal XUV intensity is reached at around 150 mbar – 200 mbar of neon gas in HHG; however, no useful image contrast and resolution could be achieved under these illumination conditions due to space-charge broadening. In this investigation, a 150 nm zirconium filter in combination with a 150 nm silicon nitride filter are used to spectrally filter the XUV intensity, which is further filtered by a Mo/Si multilayer mirror of 57% reflectivity at 93 eV (as described in section 4.1). The XUV peak intensity is estimated to be reduced by over three orders of magnitude by reducing the neon gas pressure in the gas target besides implementing the filters and the XUV mirror in order to achieve low enough intensity for PEEM operation without space charge.

In photoemission induced by ultrashort pulses the tolerable number of photoelectrons per pulse should not exceed about one electron within $1 \mu\text{m}^2$ [35, 190], because multiple electrons emitted quasi-simultaneously suffer from Coulomb repulsion either at the sample, or more severely, at the back focal plane inside the PEEM column where the electron beam trajectories cross. It is also possible that space charge effects can occur in a retardation lens, especially in the case of a PEEM incorporated with a hemispherical energy analyzer, as the electrons are decelerated before entering the analyzer [188]. When attenuating the XUV pulse intensity by gradually decreasing the neon gas pressure the image contrast as well as the image resolution improves until an optimum at a neon gas pressure of about ~ 50 mbar (see fig. 4.6(a)). Thus, the XUV intensity is just below the onset of space charge at this gas pressure, not exceeding a photoelectron flux of about one electron per pulse within $1 \mu\text{m}^2$. Note, however, that the achieved parameters are a trade-off between reasonable photon flux (image acquisition time) and space charge suppression; but even under these conditions at 1 kHz repetition rate space charge is not totally avoided. A similar observation was concluded by A. Mikkelsen *et al.* [35], who also

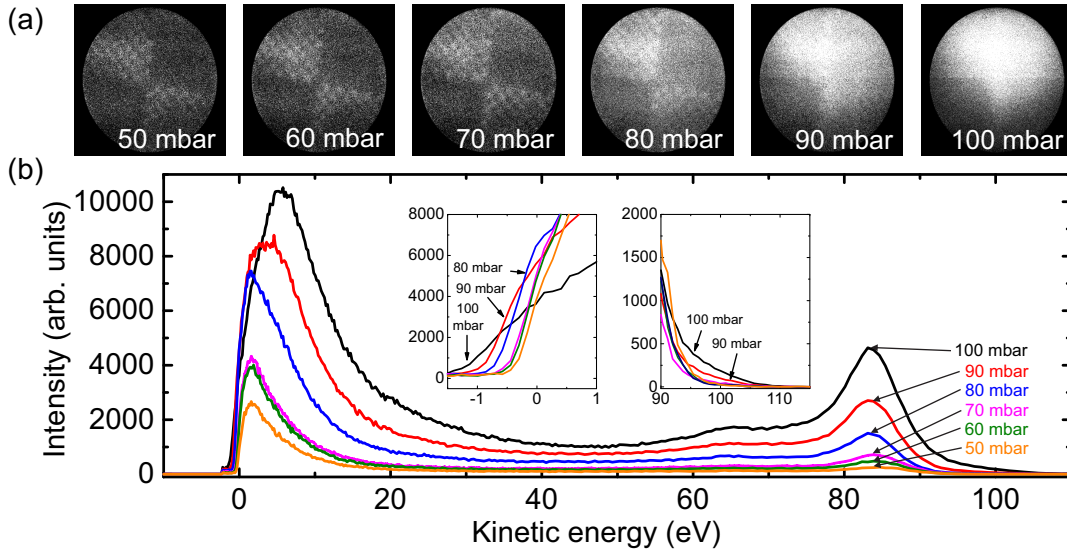


Figure 4.6: Space charge effect investigation. (a) PEEM images obtained by XUV excitation at different gas pressures. (b) Full energy spectra of XUV emitted photoelectrons at different gas pressures. Left inset: intensity normalized at secondary electron peak. Right inset: intensity normalized at primary electron peak.

used attosecond XUV pulses at 1 kHz repetition rate but in pulse trains and with a central photon energy of 30 eV to image lithographically fabricated gold nanoholes using a PEEM without a ToF option. Fig. 4.6 (b) displays the corresponding energy spectra varying with the gas pressure. The image starts to get blurred at a pressure of 70 mbar (see fig. 4.6 (a)), whereas the spectrum only starts to broaden at 80 mbar (fig. 4.6 (b)). Note that the very bright spot in the top center area of the images at 90 mbar and 100 mbar might be an artefact resulting from multiple hits on the DLD in addition to the blurriness caused by the space charge effects. This can be explained by a count rate significantly above the laser’s repetition rate at the DLD at 90 mbar and 100 mbar. Interestingly, it is observed that the high-energy electron peaks do not shift in energy as the gas pressure increases. In contrast, the low-energy electron peak starts to shift at 90 mbar from 1.4 eV to 3.7 eV and at 100 mbar to 5.5 eV, respectively. This shows that the low-energy electrons (secondary electrons) are more easily influenced by space charge effects as they are slow and thus have more time to disperse before entering the PEEM’s extractor compared to the high-energy valence band electrons. This is a very important finding, since it underlines the feasibility of the atto-PEEM concept, which is based on the image acquisition and analysis using the fast valence band electrons, which carry information about the instantaneous electric field of the LSPs.

As pointed out in section 4.1, strong attenuation of the XUV intensity to avoid space charge extends the image acquisition time to a few hours or even more if

energy-filtered imaging on fast valence band electrons is taken into account, making time-resolved experiments nearly impossible at 1 kHz repetition rate. Therefore, high-repetition-rate XUV sources [191–195] ranging from hundred kilohertz to megahertz repetition rates are demanded and currently being developed in order to enable realistic atto-PEEM experiments in a pump-probe scheme as well as for other applications. The group of A. Mikkelsen has demonstrated an improvement of XUV-PEEM imaging quality on silver nanowires by a factor of 2 – 3 with a reduced image acquisition time by a factor of ~ 10 when increasing the repetition rate from 1 kHz to 200 kHz [133, 138]. In their case, the PEEM imaging was also achieved with attosecond XUV pulse trains centered at around 30 eV, as aforementioned. Ultimately, we expect that an attosecond XUV source in the low-megahertz regime will allow an image acquisition time on the order of seconds to minutes while excluding any space charge effects. On the other hand, high-megahertz HHG sources might be disadvantageous if a ToF spectrometer is used, since the maximum ToF range is limited by the repetition period. This fundamental limit also prevents a high time resolution of the ToF spectrometer to be achieved, thus decreasing the attainable energy resolution. Alternatively, a PEEM with a hemispherical energy analyzer or IEF can be considered as a solution to this issue posed by hundred-megahertz HHG sources, since the resolution of these spectrometers does not depend on repetition rate. They lack, however, the capability of parallel data acquisition for all electron energies of interest simultaneously, which is naturally provided by a ToF spectrometer.

Laser intensity effects in single-shot CEP-tagged PEEM

In the previous chapter we have demonstrated that a spatial resolution of ~ 200 nm could be achieved using ~ 350 as XUV pulses on lithographically fabricated gold structures. We have shown that utilizing energy-filtered imaging of the secondary electrons could improve the chromatic aberrations, and we have also successfully proven the microspectroscopic identification of core and valence band electronic states using these ultrashort XUV pulses. Ultimately, it is more intriguing to use the CEP of few-cycle laser pulses (as the pump) to control the plasmonic optical fields on a nanostructured metal surface, and the field dynamics can be probed by synchronized attosecond XUV pulses. In this chapter and the next chapter first studies on CEP control without a pump-probe scheme will be presented. Instead of employing a typical commercially available CEP locking scheme, we have combined a single-shot stereographic ATI phase meter with ToF-PEEM (see subsection 3.3.3) for controlling and probing plasmonic fields [172]. More details on the advantages of using a phase tagging technique can be found in subsection 3.3.2. First CEP-resolved measurements on NPOP and surface roughness from a gold film show an apparent CEP modulation with a period of π . This modulation is found to originate from an intensity dependence of the photoelectron spectra and the CEP measurement rather than from an intrinsic CEP dependence, which is confirmed by simulations. Solutions to eliminate this CEP artefact in our CEP-tagged PEEM setup will be presented in chapter 6.

5.1 Nonlinear photoemission at nanostructures

Nonlinear photoemission, such as multiphoton photoemission and light-induced tunneling, is now made available with the advance of femtosecond laser pulses with large peak intensities, particularly in conjunction with tailored nanostructures for enhancing the optical fields at the surface. An introductory description of nonlinear photoemission is given in subsection 2.2.2. Laser-excited nonlinear PEEM provides a direct imaging capability which is highly sensitive to the local magnetic or electric surface fields with a nanoscale spatial resolution. By exploiting such an imaging technique, we attempt to explore light-field control in supported nanostructures using intense, CEP-controlled few-cycle laser pulses.

The experiments described in this chapter [172] were performed using 4 fs – 6 fs few-cycle laser pulses with a central wavelength of 730 nm at a repetition rate of 10 kHz (see subsection 3.3.1). The incident angle of both the UV light and the p-polarized laser pulses was 65° to the sample surface normal. In order to avoid too high peak intensities on the sample due to the intense few-cycle laser pulses, the focusing mirror ($f = 25$ cm) was positioned out-of-focus such that the beam spot at the sample was rather large, approximately $300 \mu\text{m} \times 600 \mu\text{m}$ (FWHM). NPOP was chosen as the first sample, as it exhibits a very strong field enhancement when in resonance with the incident light, given by the very small but well-defined gap size (<1 nm) between the gold nanoparticles and the gold film. See subsection 3.4.1 for a detailed sample description.

A near-field gap resonance is excited when the light's electric field is aligned across the nanoparticles and the gold plane. A field enhancement factor of ~ 400 is obtained based on finite element method simulations using our laser excitation parameters at an incident angle of 65° . A peak laser intensity of $\sim 5 \cdot 10^8 \text{ W/cm}^2$ was used to illuminate the sample. Fig. 5.1 (a) and (b) depict the NPOP at medium magnification and high magnification, respectively, under a SEM. The nanoparticles are separated from each other by some hundred nanometers to several micrometers, as shown in fig. 5.1(a). Some unknown contaminant is observed as a transparent layer surrounding the nanoparticles, which was not present during the measurements (see fig. 5.1(b)). The SEM image was taken about three years after the measurements and this contamination must have built up over the time. Fig. 5.1 (c) shows the energy-integrated PEEM image over $7 \cdot 10^6$ laser shots on the NPOP sample. The image is smeared out in one direction because astigmatism was not corrected during the measurement. Fig. 5.1 (d) illustrates the corresponding integrated electron energy spectrum from the entire PEEM image of $60 \mu\text{m}$ field of view. The electron spectrum represents the kinetic energy distribution of electrons after multiphoton photoemission reduced by the work function of the sample. It is expected that differ-

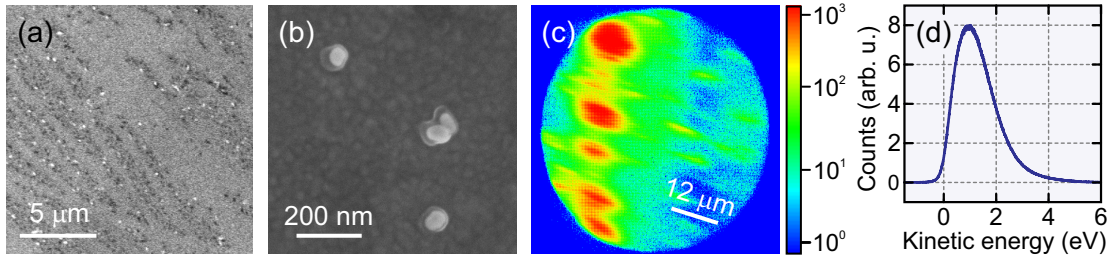


Figure 5.1: Microscopic images and photoemission spectrum of the NPOP sample. (a) SEM image of the NPOP displaying isolated gold nanoparticles indicated by the bright dots on the gold film surface. (b) A zoomed-in SEM image of the ~ 90 nm gold nanoparticles. (c) PEEM image of the NPOP illuminated by few-cycle laser pulses. The achievable image contrast is given mainly by the multiphoton photoemission. The hot spots are from plasmonic-enhanced photoemission of the nanoparticles. Larger hot spots are formed by clustered nanoparticles. The colorbar shows the counts. (d) Normalized energy spectrum integrated over the whole NPOP sample area as shown in (c).

ent numbers of photons are involved in the emission process, since a broadband laser was used for excitation. In this case, a minimum of three photons (the central photon energy is 1.7 eV, determined from the laser’s central wavelength) are required to overcome the sample’s work function of 4.0 eV [107]. Another aspect considering the contribution of light-induced tunneling on the spectrum of NPOP will be discussed in subsection 5.2.1.

5.2 Investigation of CEP artefact for NPOP and surface roughness

This section presents the investigation and analysis of an apparent CEP modulation found in our first CEP-resolved experiments on plasmonic nanostructures. Any real CEP effects can possibly be overwhelmed by an undesirable CEP artefact, which arises from laser intensity fluctuations in the experimental setup. We carried out intensity-dependent measurements on the kinetic energy of the photoelectrons emitted from hot spot areas of the plasmonic sample and the CEP of the according laser pulses detected by the stereographic ATI phase meter to gain a deeper understanding for the cause of this CEP artefact.

5.2.1 Apparent CEP modulation

The PAP obtained from the phase meter for the previously described NPOP measurement is shown in fig. 5.2(a). The PAP is reconstructed from the phase-tagged data set by using the asymmetry values measured for every detected electron count

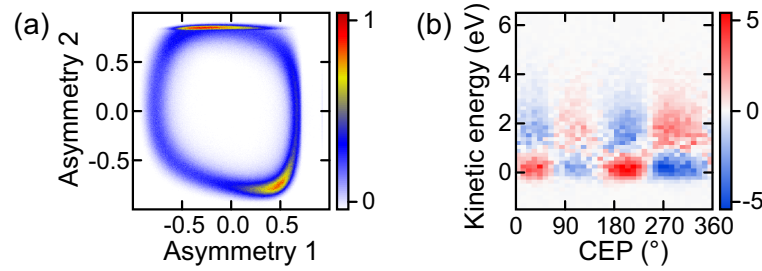


Figure 5.2: CEP-tagged PEEM results for the NPOP sample. (a) PAP for $7 \cdot 10^6$ laser shots; the pulse duration is estimated as 4.1 fs FWHM. The colorbar shows the normalized counts. (b) Normalized CEP spectrogram for the NPOP with the CEP-averaged spectrum subtracted. The colorbar shows the modulation depth in percent.

and a CEP map is generated by balancing the PAP as described in subsection 3.3.2 in order to obtain the actual CEP φ . Subsequently, the DLD data sets (x, y, t) can be sorted or filtered according to the associated CEP values. More details regarding CEP-tagged PEEM configuration can be found in subsection 3.3.3. In order to analyze the CEP dependence, the difference between CEP-resolved electron spectra and the CEP-averaged electron spectrum, normalized to the peak amplitude of the CEP-averaged spectrum, is taken to enhance the visibility of the CEP effect and depict the modulation depth. It is shown as a CEP spectrogram in fig. 5.2(b). A CEP bin size of 10° is chosen, which yields 36 bins over the entire 2π (360°) range, providing adequate statistics within each bin at a reasonable acquisition time. A modulation of the spectrum with a period of π (180°) is clearly visible, corresponding to an apparently CEP-dependent energy shift: the modulation of the high-energy part of the spectrum around the CEP-averaged central energy peak is inverted, i.e. shifted by π , compared to the low-energy part, while no modulation is visible at the central energy.

For comparison, we also carried out a phase-tagged measurement on a 90 nm thick multicrystalline gold film on an ITO-coated glass substrate. Fig. 5.3(a) shows the gold film feature under UV light excitation obtained with the PEEM. Irregularities, such as bigger crystal grains or possibly unknown particles on the multicrystalline gold film surface, can be observed, whereas very smooth surfaces are visible on the ITO-coated glass and single-crystalline gold flake. It is well known that evaporated multicrystalline gold films exhibit typical crystal grain sizes of 30 nm – 50 nm [196]. Atomic force microscopy (AFM) imaging on the investigated gold film confirms a crystal grain size of 30 nm – 50 nm in our case. Its corresponding root mean square (rms) surface roughness is ~ 0.9 nm. It is intriguing to see some bigger crystal grains or unknown hill-shaped particles, which are 15 nm – 60 nm in height and have a lateral extent of 50 nm – 150 nm in the AFM image (see fig. 5.3(b)). These irregu-

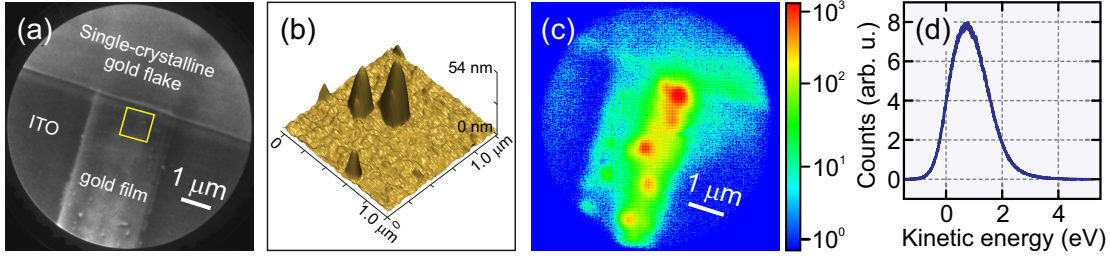


Figure 5.3: Microscopic images and photoemission spectrum of the gold surface roughness sample. (a) PEEM image of the 90 nm thick multicrystalline gold film on an ITO-coated glass substrate using UV lamp excitation. The surface roughness of <1 nm is too fine to be resolved with the PEEM. However, larger surface roughness of ~ 11 nm rms can be seen on the gold film surface. (b) AFM image of the area marked by a yellow square in (a). Two kinds of surface roughness are observed, see text for details. (c) PEEM image of the same sample area as shown in (a), acquired with few-cycle laser pulses. The hot spots originate from plasmon-enhanced photoemission from the gold surface roughness. The colorbar shows the counts. (d) Normalized energy spectrum integrated over the whole surface roughness sample area as shown in (c).

larities result in a rms surface roughness of ~ 11.1 nm, and it is believed that the rough distinct features can be caused by coalescence or contamination either during the gold evaporation process or the lift-off process in EBL. Surface roughness is chosen as an experimental control to scrutinize the apparent CEP effect observed in our CEP-tagged setup, since no CEP effect is expected from random nanostructures at a surface. The photoemission from hot spots formed by the surface roughness of this gold film is shown in fig. 5.3 (c). A defocused peak laser intensity of $\sim 8 \cdot 10^8$ W/cm² was used for the sample illumination. A variety of surface plasmon modes seen as the hot spots can be excited in the nanoscale gaps between gold crystal grains upon the broadband laser excitation ranging from 400 nm – 1000 nm. The NPOP exhibits a slightly higher electron kinetic energy of ~ 4 eV (see fig. 5.1 (d)) than the surface roughness (~ 3 eV), even though the laser peak intensities for both samples are comparable. This can be explained by an energy gain of the electrons when being expelled from the strong plasmonic near-field region inside the gap, following the ponderomotive force [107]. It is believed that a tunnel ionization process is also involved besides the multiphoton photoemission process in the case of NPOP. This can be validated by the Keldysh parameter, $\gamma = \omega\sqrt{2m_e\phi}/eE_0$ [94], where ω is the angular frequency of the laser, m_e the electron mass, ϕ the work function, e the electron charge and E_0 the electric field amplitude (see eqn 2.5). With a laser peak intensity of $\sim 5 \cdot 10^8$ W/cm² and a field enhancement of 400 by the plasmonic resonance, this yields a total electric field strength E_{gap} of ~ 20 GV/m in the gap. Using our experimental parameters with the sample's work function being 4 eV and the laser's central wavelength being 730 nm we obtain $\gamma \approx 0.87$. Note that multiphoton pho-

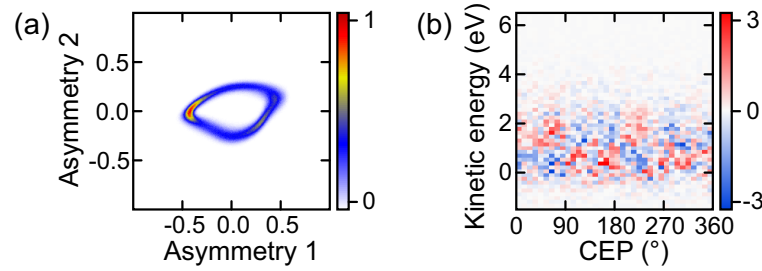


Figure 5.4: CEP-tagged PEEM results of the gold surface roughness sample. (a) PAP for $2 \cdot 10^6$ laser shots; the pulse duration is estimated as 6.5 fs FWHM. The colorbar shows the normalized counts. (b) Normalized CEP spectrogram for the surface roughness sample with the CEP-averaged spectrum subtracted. The colorbar shows the modulation depth in percent.

toemission is favored for $\gamma \gg 1$ and tunneling for $\gamma \ll 1$ [94]. Hence, this confirms our assumption that electron tunneling also plays a role in the emission process, which is facilitated by the strong near fields at the coupled plasmonic structure. Note that the static field of the PEEM generated by the extractor is only ~ 5 MV/m and therefore can be neglected, as it is 4 orders of magnitude smaller than E_{gap} . A smaller PAP is obtained for this measurement, suggesting a longer pulse duration possibly due to a change in dispersion of the laser pulses (see fig. 5.4 (a)). This PAP is also reconstructed from the phase-tagged data set. The non-uniform shape of the PAP is caused by imperfect phase meter alignment. For the gold surface roughness sample a similar spectral feature with a modulation period of π but with smaller modulation depth is observed (see fig. 5.4 (b) and cf. fig. 5.2 (b)).

Since we expect no observable CEP dependence from the surface roughness sample, we suspect the apparent modulation to be caused by a measurement artefact. Furthermore, a 2π rather than π CEP modulation is expected from solid state samples [12, 40], thus the same artefact is likely the cause for the observed CEP modulation from the NPOP sample. A strong evidence for this is the persistence of the CEP modulation in both measurements when shifting the CEP tagged list by several events, i.e. associating the CEP of earlier or later laser shots to every electron event. This persistence is not expected for a real CEP effect, since the CEP is assumed to be random for every laser shot in a kHz amplified laser system, and any CEP correlation should be destroyed when shifting the tagged CEP list even by a single event. Here, we found no apparent change in modulation depth when shifting by several events (up to ~ 10). When shifting by more events, the modulation becomes less and less pronounced and entirely fades away into random noise after shifting by a number of events corresponding to about 2 s (events are correlated to timing via the count rate). This was consistently found for both measurements despite their different count rates (~ 1000 counts/s for NPOP vs. ~ 150 counts/s for gold surface

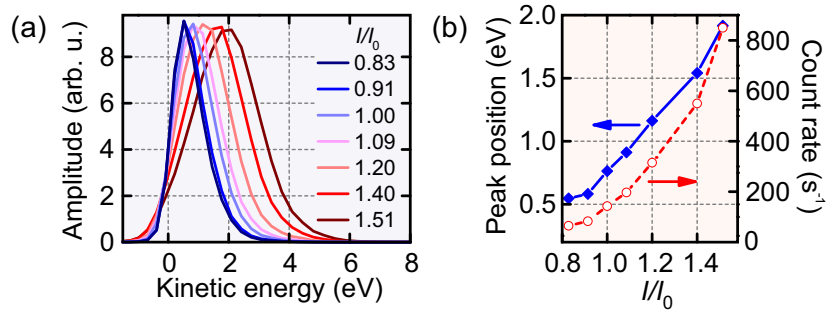


Figure 5.5: Laser intensity dependence of the photoemission spectra. (a) Photoemission spectra from the gold surface roughness sample at different relative intensities I/I_0 , I_0 being the intensity used for phase-tagged experiments. Energy shift and broadening are evident. (b) Shift of the central energy as a function of intensity (blue) showing a nearly linear intensity dependence after an onset. The count rate increases with an exponent of 4.4 as a function of intensity (red), indicating a 4 – 5 photon photoemission process.

roughness hot spots). The persistence of the observed apparent CEP modulation of the photoelectron spectra over timescales on the order of one second suggests a correlation with slowly varying laser parameters other than its CEP, such as the intensity, which affects both the photoelectron spectrum and the CEP measurement inside the phase meter in a correlated way and thus introduces an apparent CEP artefact into the CEP-tagged measurement. The intensity appears to be a suitable cause for this effect, since notable intensity fluctuations of our laser take place on a timescale of hundreds of milliseconds and above with an amplitude of 0.6 % rms over 1 min and up to several percent over few hours. This means that on timescales of few hundred milliseconds and below the laser intensity is essentially constant, which is in good agreement with the observed temporal persistence of the apparent CEP modulation. On larger timescales (seconds and above), intensity fluctuations become more pronounced, which destroys any correlation between measured events via the laser intensity.

5.2.2 Laser intensity dependence

Fig. 5.5 (a) shows normalized photoemission spectra from the gold surface roughness sample for different relative laser intensities, I_0 being the intensity used for the phase-tagged experiments in fig. 5.3 (c) and (d) as well as in fig. 5.4 (b). A space charge-induced energy shift and broadening with increasing laser intensity are clearly visible. Fig. 5.5 (b) quantifies the shift of the kinetic energy peak (blue curve). An onset is evident at about $0.9I_0$, attributed to space charge, followed by a nearly linear energy shift with intensity. Around I_0 the energy shift is about 20 meV per percent of intensity change. Besides the energy shift it is worth to note that the

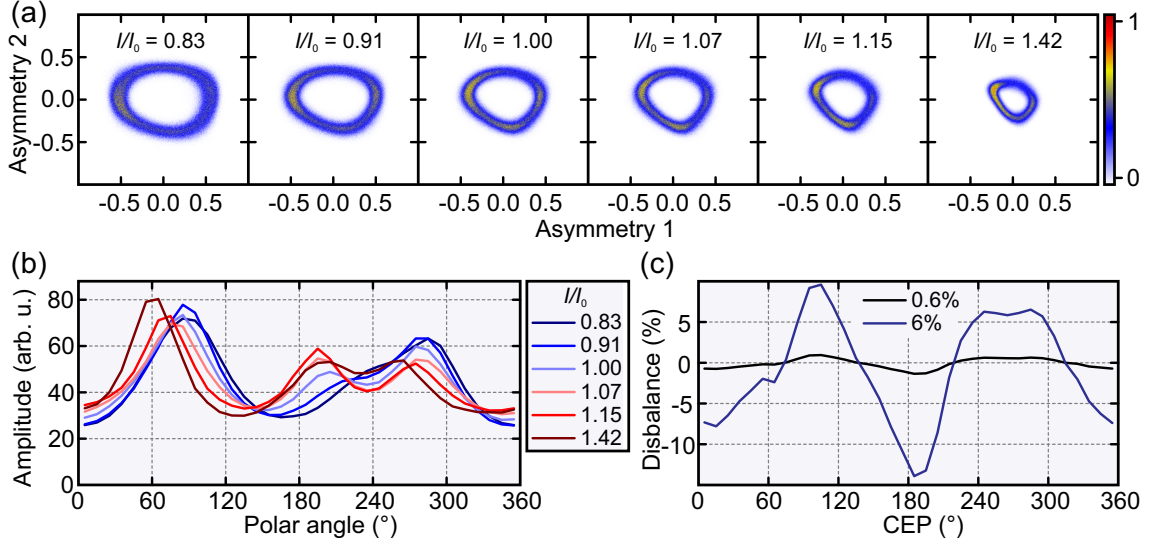


Figure 5.6: Laser intensity dependence of the PAP and intensity-induced disbalance of the CEP retrieval. (a) PAP as a function of relative intensity I/I_0 , I_0 being the intensity used for phase-tagged experiments. The colorbar shows the normalized counts. (b) Polar distribution of counts extracted from the PAP. (c) Calculated disbalance of the CEP for a laser intensity change of 0.6% (black) and 6% (blue), respectively, around I_0 .

count rate increases as a function of intensity with an exponent of 4.4 (red curve), indicating a 4 – 5 photon photoemission process.

An intensity-dependent energy shift of the photoemission spectrum can only explain the persistent CEP modulation if it is accompanied by an intensity-dependent disbalance of the PAP, which induces a deviation from a uniform distribution of counts over the CEP for different intensities. Fig. 5.6(a) shows the PAPs for different relative intensities, I_0 being again the intensity used for the phase-tagged experiments in fig. 5.3(d) and fig. 5.4(b). A change in shape as well as in the polar distribution of counts is clearly visible as a function of intensity. The distribution of counts as a function of the polar angle is depicted more clearly in fig. 5.6(b) and is normally used for balancing the PAP such that each every polar angle interval contains the same number of counts (see subsection 3.3.2). Here, the balancing was omitted in order to show the naturally non-uniform distribution of counts within the PAP. Since the shape shifts and changes with intensity, the CEP retrieval becomes unbalanced for laser intensities other than the intensity at which the PAP for CEP tagging was recorded. This disbalance is quantified as the deviation from unity when normalizing the distribution of counts as a function of CEP at a particular intensity to the distribution at I_0 . The counts distribution curve within the PAP can be obtained for any intensity within the measured range around I_0 by interpolation. Fig. 5.6(c) shows the resulting disbalance as a function of CEP for

an intensity change of 0.6 % around I_0 in black (typical laser intensity drift over 1 min) and 6 % in blue (typical laser intensity drift over few hours), respectively. The disbalance exhibits a periodicity of π and scales approximately linearly with the intensity change. It amounts to ~ 2.3 % peak-to-peak (for 0.6 % intensity change) or ~ 23 % peak-to-peak (for 6 % intensity change), respectively.

5.3 CEP artefact simulations

In order to reproduce the impact of this intensity-dependent disbalance on the measured CEP spectrogram, a phase tagging simulation using 50 million single shots was performed and the simulation result was compared with the measurement of the gold surface roughness sample. We chose this sample because of the similarity of the corresponding PAP (see fig. 5.4(a)) with the PAP used for the investigation of the intensity dependence (see fig. 5.6(a), $I/I_0 = 1.00$). The measured CEP spectrogram is shown again in fig. 5.7(a) for comparison along with the shift of the central kinetic energy as a function of CEP (see fig. 5.7(b)), determined by Gaussian fits. For simplicity, a Gaussian kinetic energy distribution was chosen for the simulation, resembling the experimentally obtained energy spectrum of the gold surface roughness sample (~ 1.6 eV FWHM, ~ 0.8 eV central energy), as well as a Gaussian intensity distribution around I_0 , the standard deviation of which was used as a variable parameter (see below), and a random CEP for every event. All distributions (energy, intensity, CEP) were initially uncorrelated, representing a sample with no CEP dependence. The kinetic energy of each event was then modified according to the associated laser intensity using the experimentally obtained value of 20 meV per percent of intensity change (see fig. 5.5(b)). Also, the weighting of each event was calculated according to the disbalance value associated with laser intensity and CEP using the relationship obtained from the intensity dependence measurements for the gold surface roughness sample (see fig. 5.6(c)). Afterwards, a CEP spectrogram was constructed by summing up the weightings of all events in a particular energy and CEP bin. The standard deviation of the intensity distribution was used as a parameter in the simulation in order to find the best match to the measurement. The CEP spectrogram for a laser intensity distribution of 6 % rms is shown in fig. 5.7(c) along with the shift of the central kinetic energy as a function of CEP (see fig. 5.7(d)). This value is in good agreement with the typical laser intensity drift over several hours of measurement time and yields the best match to the measured CEP spectrogram as well as the measured shift of the kinetic energy of about 26 meV peak-to-peak. Despite the different PAPs used for the measurement and simulation, resulting in slightly different shapes, we obtained a remarkable agreement, both qualitatively (matching modulation period of π) and quantitatively (matching modulation depth

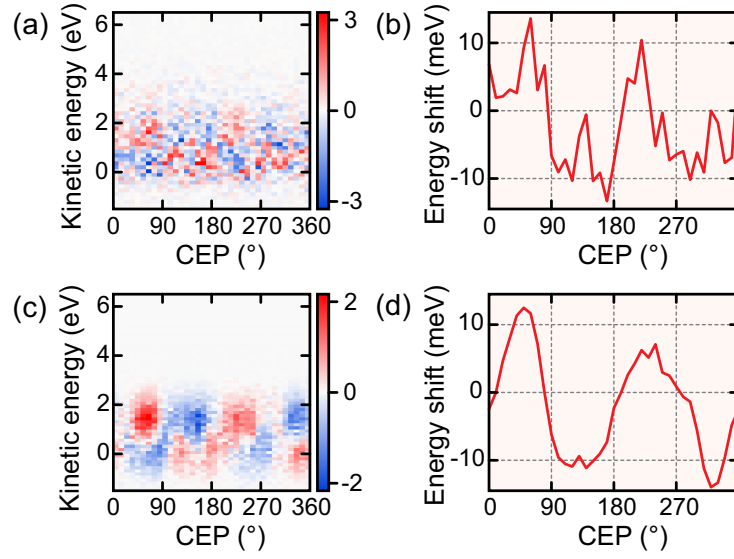


Figure 5.7: Simulation of apparent CEP modulation caused by laser intensity fluctuations. (a) Measured normalized CEP spectrogram for the gold surface roughness sample with the CEP-averaged spectrum subtracted. The colorbar represents the modulation depth in percent (from fig. 5.4 (b)). (b) Central kinetic energy shift as a function of CEP, obtained from the measured spectrogram. (c) Simulated normalized CEP spectrogram with the CEP-averaged spectrum subtracted for a Gaussian intensity distribution with a standard deviation of 6% around I_0 . The colorbar represents the modulation depth in percent. See text for simulation details. (d) Central kinetic energy shift as a function of CEP obtained from the simulated spectrogram.

and energy shift). Since the simulation was performed with no intrinsic CEP effect, i.e. no initial correlation between CEP and kinetic energy or weighting, this result constitutes a strong evidence for laser intensity effects being the cause of the observed apparent CEP modulation.

This finding is crucial particularly for the studies of weak CEP-dependent processes employing the phase tagging technique, as the artefact might easily outweigh a weak intrinsic CEP modulation of the studied sample. Shortening the measurement time in order to reduce laser intensity fluctuations seems infeasible with typical kHz amplified laser systems, given the low count rates necessary to avoid space charge effects (≤ 1 electron per pulse). Sufficient intensity stabilization of such laser systems while maintaining adequate pulse energies and spectral bandwidths is also intricate, requiring an effort comparable to CEP stabilization and thus lessening the benefits of the phase tagging technique. Alternatively, CEP-tagged ToF-PEEM measurements have to be restricted to plasmonic samples which exhibit a strong CEP dependence, such that the CEP artefact becomes negligible compared to the intrinsic CEP modulation. However, this would prevent ToF-PEEM from studying CEP dependence in plasmonic nanostructures, since the CEP dependence of such nanostructures [197]

and even bulk materials [54, 198] (see section 6.3) is on the order of only a few percent or less. In the next chapter we introduce intensity tagging as a technique for removing or reducing the intensity-related CEP artefact by expanding the current phase tagging technique with a single-shot intensity measurement.

Single-shot intensity-CEP-tagged PEEM

Chapter 5 discusses the discovery of an intensity-related CEP artefact in our first CEP-tagged ToF-PEEM experiments. Further investigations and analysis confirm the modulation depth and periodicity of the observed CEP artefact, which arises from an intensity-dependent energy shift of the photoelectrons emitted from the sample in combination with an intensity-dependent disbalance of the CEP retrieval from a stereographic ATI phase meter. In this chapter, we therefore introduce and incorporate intensity tagging into our current CEP-tagged ToF-PEEM setup, i.e. recording the intensity for each laser shot in addition to the CEP measurement, as a mitigation for the intensity-related CEP artefact caused by laser intensity fluctuations. As a result, the artefact background could be sufficiently reduced to reveal a CEP modulation depth as low as $\sim 1\%$ using this additional intensity tagging channel.

To date, CEP effects in solids have been experimentally studied for a gold cathode [198], tungsten and gold nanotips [12, 40], dielectric nanospheres [199, 200], plasmonic nanostructures [13, 201, 202] as well as optically transparent materials such as fused silica [203, 204] and calcium fluoride [203] for potential solid-state light-phase detections. We investigate and observe a CEP effect from a bulk W(110) single crystal surface via multiphoton and strong-field photoemission for the first time by employing the intensity-CEP-tagged ToF-PEEM. An attosecond streaking experiment using bulk tungsten has been demonstrated previously [17], however, the photoelectrons from the metal surface were emitted upon XUV excitation and only afterwards interacted with the few-cycle NIR pulse. Practically, our method constitutes a simple and relatively sensitive solid-state CEP detector, which does neither require complex fabrication and handling of nanostructures nor a two-pulse pump-probe technique. Furthermore, we extend this work to a possible application

of this technique for studying the CEP effects in two-dimensional gold nanotriangles fabricated by EBL, paving the way to lightwave nanoelectronics.

6.1 Experimental concept of intensity tagging

For implementing single-shot intensity tagging in the CEP-tagged ToF-PEEM setup (see subsection 3.3.3), a photodiode in combination with a gated integrator was added to the current data acquisition system to record the laser power for every shot. The gated integrator is triggered with the laser’s repetition rate (as the rest of the system) and is set to integrate the photocurrent within a narrow time window around each laser pulse, corresponding to the photodiode’s response time (about 10 ns), thus eliminating the majority of electronic noise within the $\sim 100 \mu\text{s}$ time interval between laser shots. The integrated signal for each pulse, which is proportional to its intensity, is held as a voltage at the integrator’s output until the next trigger pulse and sampled by the ADC system (refer to subsection 3.3.3) along with the phase meter signals. The assignment of an intensity to each detected electron event thus allows sorting or filtering the data by intensity in postprocessing and a balanced CEP retrieval can be performed using an appropriate PAP for the intensity interval of interest on the CEP-tagged data from the same intensity interval. Note that in this experiment, unlike in chapter 5, we recorded intensity and PAP information for every laser shot and not only for those laser shots which resulted in a photoelectron detection. This is required to observe a CEP-dependent modulation of the photoemission yield, which we expect from the tungsten sample (rather than only a CEP-dependent energy shift), by comparing the PAP obtained from all laser shots to the PAP obtained only from laser shots which produce photoelectron detections.

6.1.1 Intensity-resolved CEP retrieval

The intensity and PAP measurements for every laser shot are used to create a CEP map for CEP retrieval of every electron detection event based on the balancing method described in subsection 3.3.2. The additional intensity information allows creating a PAP, and thus an individual CEP map, for an arbitrary intensity interval. Fig. 6.1 (a) shows several exemplary PAPs for different intensity intervals around the average intensity, I_0 , extracted from a ~ 30 -min measurement at 10 kHz repetition rate. Although the shape and the polar distribution of counts are similar, a clear systematic change of the PAP is visible as a function of intensity. This confirms the results of the intensity scan shown in subsection 5.2.2; however, here the intensity-dependence is extracted from a single measurement, albeit over a shorter range, utilizing the laser’s intrinsic intensity fluctuation.

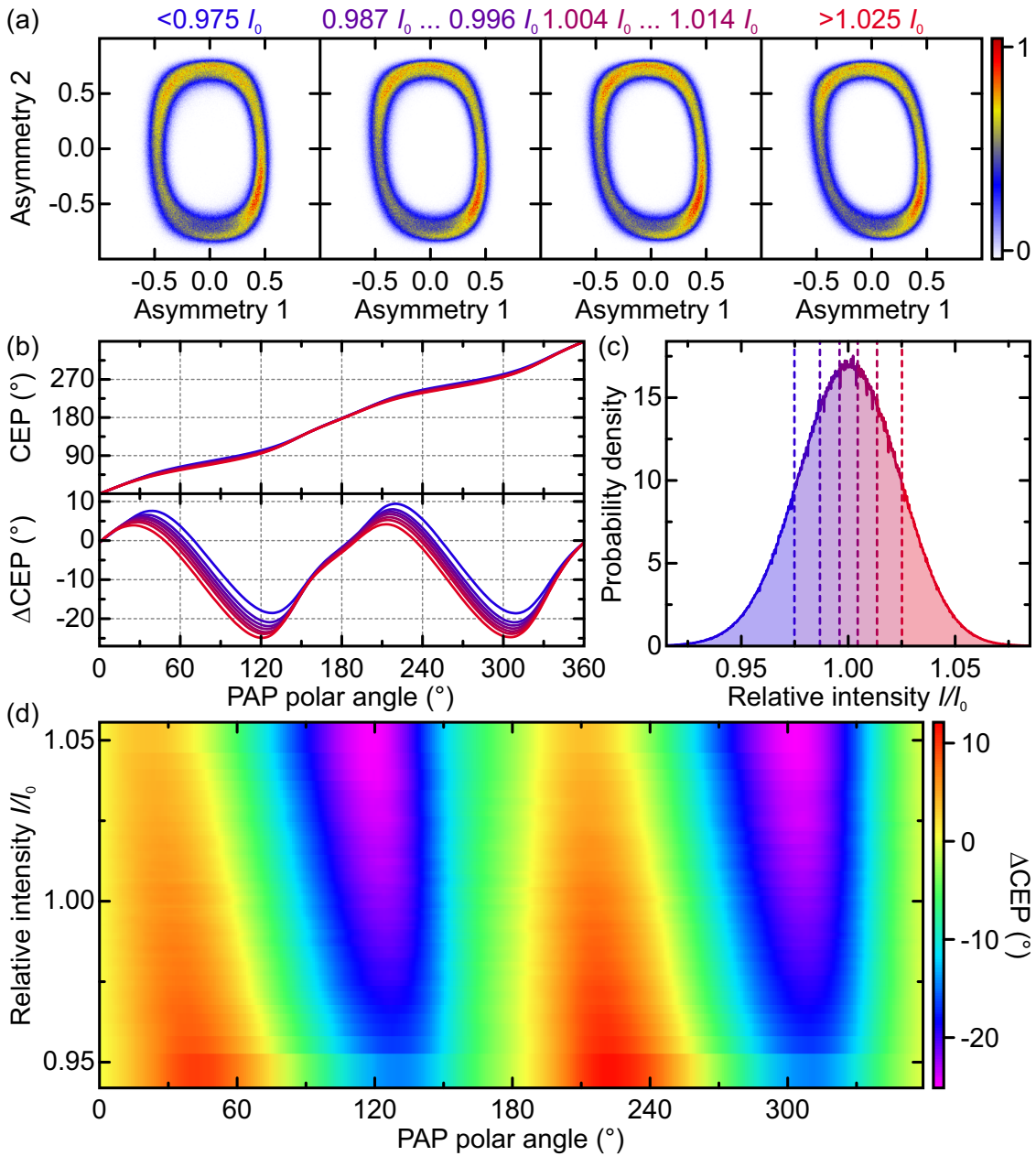


Figure 6.1: Intensity-resolved CEP retrieval. (a) Exemplary PAPs for different intensity intervals around the mean intensity, I_0 , extracted from a single measurement. (b) Top: CEP map functions for different intensity intervals denoted in (c); bottom: deviation of the CEP maps from the ideal, i.e. direct, CEP map. (c) Laser intensity distribution for this measurement relative to the mean intensity, I_0 (the integral is normalized to 1). The dashed lines denote intensity intervals with an equal amount of integrated counts and the colors correspond to the CEP maps in (b). (d) Resulting two-dimensional CEP/intensity map using 64 intensity bins with an equal amount of counts. The color scale shows the deviation from the ideal CEP map for clarity.

Fig. 6.1 (b) shows intensity-resolved CEP maps generated from these PAPs (1° bin size) in the top panel, which can be used to directly convert a measured PAP polar angle into the corresponding CEP. The bottom panel shows the deviation from the ideal CEP map¹ in order to emphasize the non-uniform distribution of counts within the PAP and its intensity dependence (see fig. 5.6 (b) in subsection 5.2.2). The CEP maps and their deviation plots are depicted here exemplarily for seven intensity intervals, which are shown in fig. 6.1 (c) by the dashed lines and the corresponding colors along with the intensity distribution of the laser pulses, which exhibits a standard deviation of 2.35% around the mean intensity, I_0 . The intensity intervals were chosen such that the number of counts within each interval is equal, thus assuring an identical statistical error for each intensity-resolved CEP map.

The individual CEP maps can be combined into a two-dimensional mapping function, which allows intensity-resolved balanced CEP retrieval for any electron detection event with an assigned PAP polar angle and laser intensity. Fig. 6.1 (d) depicts the resulting CEP/intensity map for 64 intensity intervals with an equal amount of counts each and the color scale shows the deviation from the ideal CEP map for clarity. For the actual CEP retrieval, this two-dimensional map is expanded into 3600 PAP polar angle bins (i.e. 0.1° bin size) by interpolation and the intensity dependence is parametrized for each polar angle bin by a third-order polynomial in order to smooth the map function and eliminate artefacts due to the limited number of discrete and non-equidistant intensity intervals. The CEP of an electron detection event with an assigned intensity and PAP polar angle is then calculated by taking the nearest polar angle bin in the two-dimensional map and evaluating the associated polynomial at the measured intensity.

6.1.2 Laser intensity-correlated artefact in CEP retrieval

The intensity-tagging technique also allows intensity filtering of the data in order to reduce the intensity spread of a given measurement at the expense of statistics. This eliminates any directly intensity-dependent effects and thus serves as a useful tool for a thorough investigation of the apparently intensity-related artefact in CEP retrieval discussed in chapter 5.

Fig. 6.2 (a) shows a typical laser intensity distribution (black line) around the average intensity, I_0 (same as in fig. 6.1 (c)). The blue line shows the photoemission yield from a bulk tungsten surface measured by the ToF-PEEM at an effective laser peak intensity of $(1.2 \pm 0.6) \cdot 10^{13} \text{ W/cm}^2$ as a function of relative intensity (see section 6.2 for further details of this measurement and CEP-resolved results). Each

¹An ideal CEP map is a direct (1:1) correspondence between the PAP polar angle and the CEP, except for a constant offset.

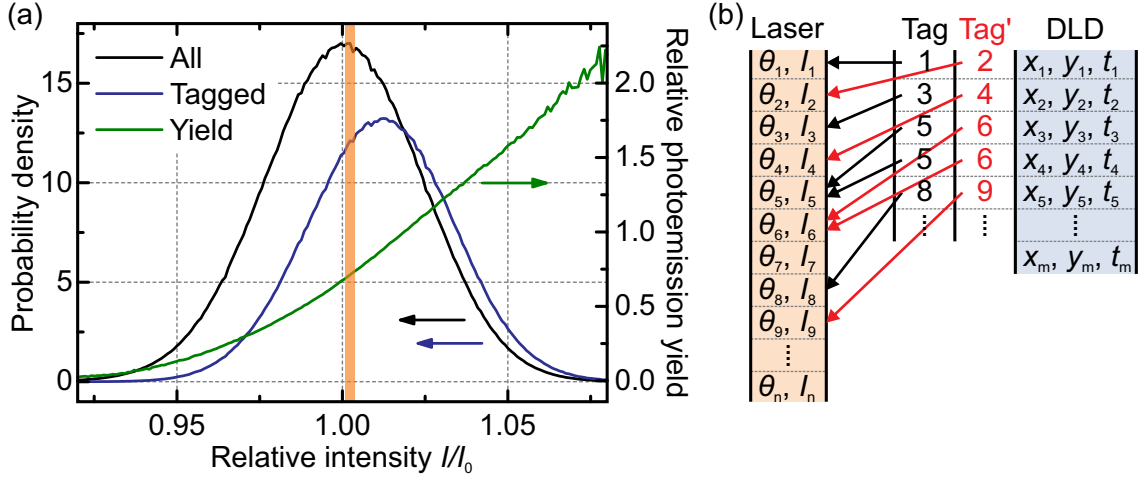


Figure 6.2: Intensity filtering and tag list assignment. (a) Laser intensity distribution relative to the mean intensity, I_0 , for all laser shots (black) and only for “tagged” shots (blue), i.e. shots with electron detection events. The integral for all laser shots is normalized to 1. The green line shows the photoemission yield per laser shot. The thin orange rectangle denotes the intensity-filtered region for the investigation of the CEP retrieval artefact. (b) Illustration of the assignment of the measured laser pulse parameters, PAP polar angle and intensity (θ_i, I_i), to the position and ToF (x_i, y_i, t_i) of the electron events measured by the DLD via the tag numbers. The black tag list (Tag) shows an example of the tagged shots including missing electron events as well as multi-hits. The red tag list (Tag') demonstrates a shift of the assignment by one laser shot by incrementing the measured tag numbers.

electron detection event is assigned with the PAP measurement (consisting of two asymmetry values A_1 and A_2 , yielding the PAP polar angle θ) and the intensity of the corresponding laser shot via the tag number of this event provided by the TDC, as described in subsection 3.3.3. Notably, the resulting intensity distribution of the detected photoemission events (i.e. “tagged” shots) is narrower than the laser intensity distribution and centered at a $\sim 1.1\%$ higher intensity, which reflects the nonlinear intensity dependence of the photoemission process. In addition, the relative yield (green line) is over unity at higher intensities, denoting a significant contribution of multiple photoemission events from a single laser shot due to the high laser intensity used. The total yield amounts to ~ 0.72 electron detection events per laser shot at the DLD. For further analysis, the data is intensity-filtered over a narrow intensity interval of $\sim 0.3\%$ of I_0 close to I_0 , denoted by the thin orange rectangle. The position and width of this interval were chosen to simultaneously filter $\sim 5\%$ of the counts for all laser shots as well as for the tagged subset in order to avoid statistical bias. The filtered data exhibits a negligible intensity variation, while providing sufficient statistics ($\sim 10^6$ laser shots).

As pointed out in subsection 5.2.1, an artefact in the CEP retrieval was observed as an apparent CEP modulation, even after shifting the list of electron events relative to the measured PAP list by up to several seconds. This persistence was found to correlate with the timescale of laser intensity fluctuations. Intensity filtering of the data enables us now to study this artefact by excluding any direct intensity dependence. Furthermore, since we recorded the laser pulse parameters for every shot, the assignment of a PAP measurement to an electron detection event can be shifted with a single-laser-shot precision, i.e. a time interval of 100 μs at a repetition rate of 10 kHz. Fig. 6.2(b) illustrates the assignment of the measured PAP polar angle (resulting from the two asymmetry values A_1 and A_2) and intensity to each electron detection event via the tag number. By adding an arbitrary offset N to all tag numbers in the list, the assignment is effectively shifted by N laser shots. An offset of $N = 1$ is shown in red as an example. Since the CEP changes essentially randomly between consecutive laser shots for a kHz amplifier system [166, 205] any residual CEP modulation after shifting the tag list by an offset of $|N| \geq 1$ shots is attributed to a systematic error, i.e. an artefact.

Fig. 6.3(a) depicts several PAPs reconstructed from the PAP asymmetry values assigned to the tagged shots (i.e. electron detection events) at different laser shot offsets between $N = 0$ and $N = 10\,000$ with the PAP reconstructed from all laser shots subtracted. All PAPs were normalized and the color scale shows the relative difference in percent. This PAP difference is shown more clearly and quantitatively in fig. 6.3(b) as the difference between the CEP maps obtained from the respective PAPs used in (a). The PAP difference at 0 shot offset reveals the actual CEP-dependent modulation of the photoemission yield from the tungsten sample with a clearly visible 2π periodicity. An in-depth analysis of this CEP effect is given in subsection 6.2.2. At an offset of $N = 1$ the previous 2π CEP modulation disappears. However, an apparent CEP modulation with a periodicity of π and a slightly smaller modulation depth remains. For larger shot offsets this residual CEP modulation becomes gradually less pronounced and fades into noise for $N \gtrsim 10\,000$, which confirms the findings in subsection 5.2.1. The corresponding temporal persistence of this artefact (~ 1 s) is at least 4 orders of magnitude larger than for the true CEP effect ($< 100 \mu\text{s}$). The skewed shape of the PAP difference plots in fig. 6.3(a) resembles a difference between two PAPs of slightly different intensities, based on the intensity dependence of the PAP shape shown in fig. 6.1(a), where the tagged PAP (skewed red contour) has a seemingly higher intensity. An actual intensity difference between the PAPs obtained from all shots and from the tagged subset can be ruled out, since the data has been intensity filtered; thus the observed PAP difference for $1 \leq N \lesssim 10\,000$ must have another cause.

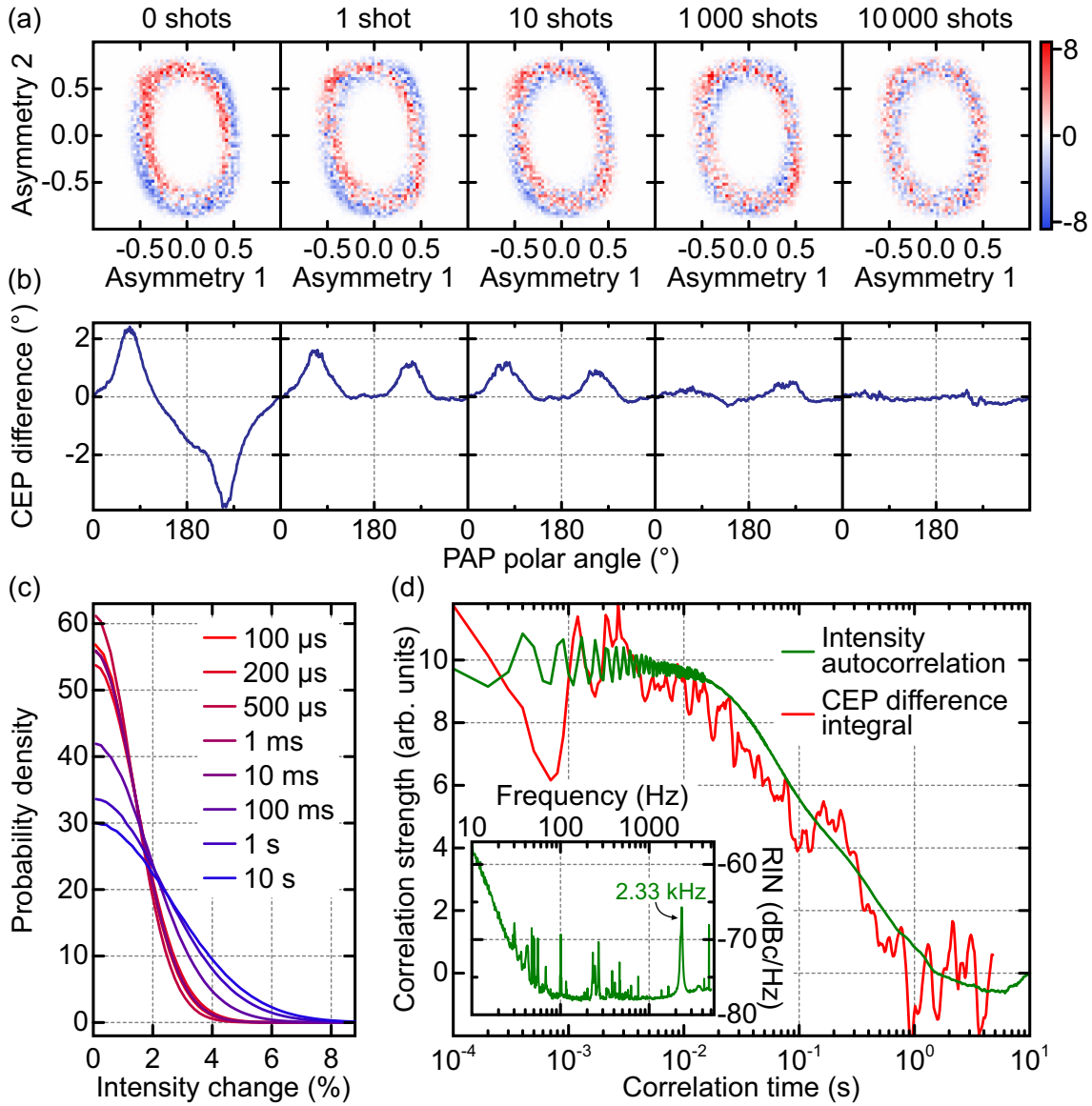


Figure 6.3: Artefact in CEP retrieval. (a) Normalized difference between PAPs reconstructed from tagged laser shots and all laser shots for different laser shot offsets between $N = 0$ and $N = 10000$ (see text for details). The color scale shows the relative difference in percent. (b) Difference between the CEP maps obtained from the respective PAPs used in (a). (c) Probability density for an intensity change between any pair of laser shots separated by a particular correlation time (100 μ s to 10 s). The integral of each curve is normalized to 1. (d) Autocorrelation trace of the laser intensity (green) in comparison to the artefact strength (red), given by the integral of the respective CEP map difference curves in (b) (see text for details). A modulation of the intensity autocorrelation with a 430- μ s period is attributed to a 2.33-kHz noise peak in the relative intensity noise (RIN) graph shown in the inset.

As discussed in sections 5.2 and 5.3, the temporal persistence of the CEP artefact resembles the characteristic timescale of the intensity drift in our laser system, which is illustrated in fig. 6.3 (c). The relative intensity change between pairs of laser pulses separated by different amounts of time (from 100 μs , or one shot, to 10 s, or 100 000 shots) is shown as a probability distribution. The distribution becomes significantly broader when the pulses are separated by 100 ms or more, indicating a higher probability for a large change in intensity over these timescales. A more complete picture of the temporal characteristics of the laser intensity fluctuations is provided by the autocorrelation function of the change in laser intensity, $\Delta I(t) = I(t) - I_0$, which is given by:

$$\Delta I^{\text{AC}}(t) \propto \int_{-\infty}^{\infty} \Delta I(t) \Delta I(t + \tau) d\tau. \quad (6.1)$$

The result is shown in fig. 6.3 (d) as the green curve (only for positive correlation times). A large autocorrelation value denotes a nearly constant (i.e. highly correlated) intensity on this timescale, while a small or zero value denotes a correlation of essentially random intensities, i.e. little or no correlation at all. The data acquisition was performed in chunks of 10 s exposure time with few-second breaks in between for data processing and storage, thus the largest correlation timescale for an accurate autocorrelation value is 10 s. For enhanced statistics, the autocorrelation was calculated for each 10-s chunk within the ~ 30 -min measurement and then averaged. A transition from strong to weak correlation is clearly visible in the 10-ms to few-second range, revealing the onset of slow intensity drift of the laser system. Furthermore, a modulation of the autocorrelation trace with a period of $\sim 430 \mu\text{s}$ is visible, corresponding to a frequency of 2.33 kHz. This frequency peak is also found in the relative intensity noise spectrum of the laser, shown in the inset in fig. 6.3 (d), denoting characteristic intensity noise on a shot-to-shot timescale, most likely due to noise in the pump source.

Remarkably, the ‘‘strength’’ of the CEP artefact (red line in fig. 6.3 (d)), given by the integral over the CEP map difference plots in fig. 6.3 (b) for laser shot offsets N of the according correlation times (i.e. $N \cdot 100 \mu\text{s}$)², is in excellent agreement with the intensity autocorrelation trace after appropriate scaling. This is a strong evidence that the cause for the artefact is indeed correlated to the laser intensity, despite intensity filtering. What seems to be a contradiction can possibly be explained by laser parameters which depend on the peak intensity rather than the average intensity and are not monitored for every laser shot in this measurement scheme, such as the spectrum and the pulse duration. Since the linear photodiode used for intensity tagging produces a signal proportional to the pulse energy, which is a measure for

²Note that only offsets up to $N = 50\,000$ (i.e. a correlation time of 5 s) are shown, since larger offsets would reduce the available data within the 10-s chunks by more than 50%.

the average pulse intensity, it is impossible to distinguish between pulses with different peak intensities, if they have the same pulse energy (or average intensity), for example, if the pulse duration changes. The stereographic ATI phase meter is highly sensitive to the shape of the electric field of a laser pulse (see subsection 3.3.2), which is directly related to pulse duration and peak intensity, and can therefore produce different PAPs for the same average intensity, for instance, if the pulse duration fluctuates due to changes in dispersion. At the same time, the photoemission yield also strongly depends on the pulse duration or peak intensity rather than the average intensity, since it is a nonlinear process. Thus, the PAP generated only from tagged shots (i.e. photoelectron detection events) is likely biased towards pulses with higher peak intensity for a given average intensity, while the PAP generated from all shots is unbiased with respect to peak intensity. This argument is somewhat supported by the fact that the PAP generated from tagged shots resembles the PAP generated from all shots but filtered for a higher average intensity, as pointed out earlier. Despite not knowing the peak intensity for every shot, this observation can be used to possibly reduce or entirely eliminate this artefact by slightly adjusting the range of the intensity filter for the reference PAP generated from all shots.

6.1.3 Intensity-bias technique for artefact correction

Fig. 6.4 (a) illustrates the artefact correction by introducing an intensity bias. While the tagged laser shots (blue line) are filtered as before within a narrow intensity interval of 0.3% of I_0 close to I_0 (blue shaded area), the position of the intensity filter for the reference PAP obtained from all laser shots (black line) can be varied independently (dark gray shaded area) by an arbitrary amount, $\Delta I/I_0$. After creating the respective PAPs for all shots and for tagged shots only, the difference between the CEP maps obtained from them (see fig. 6.3 (b)) is shown in fig. 6.4 (b) for different values of the intensity bias $\Delta I/I_0$ at a laser shot offset of $N = 1$. For zero intensity bias, the CEP artefact is prominently visible (cf. second plot in fig. 6.3 (b)) but decreases for positive intensity bias until it is minimized at $\Delta I/I_0 = 0.0062$. For higher intensity bias values the artefact is inverted. A quantitative analysis is given in fig. 6.4 (c), which shows the residual artefact strength as a function of intensity bias for different laser shot offsets N . Here, the residue is obtained by integrating the square of the CEP map difference plots in fig. 6.4 (b). Notably, the optimal intensity bias value, which minimizes the residual artefact, moves from $\Delta I/I_0 = 0.0062$ for $N = 1$ to zero for $N \gtrsim 10\,000$ (or ~ 1 s of correlation time). This is in agreement with the correlation timescale for the laser intensity (cf. fig. 6.3 (c) and (d)) and thus the persistence time of the artefact (cf. fig. 6.3 (a) and (b)). Note that the systematically similar noise pattern for different values of N reflects the shape of

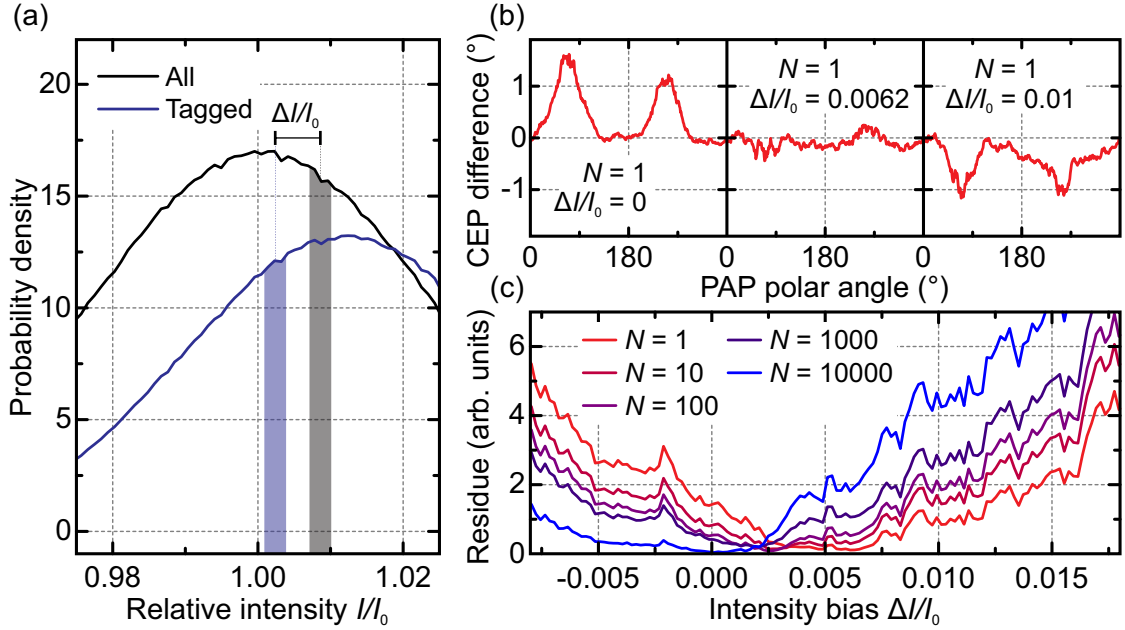


Figure 6.4: Artefact correction by introducing an intensity bias. (a) Laser intensity distribution for all (black) and only for tagged (blue) laser shots (zoom of fig. 6.2 (a)). The tagged laser shots are filtered as before within a narrow window (0.3% of I_0) close to I_0 , marked by the blue shaded area. The filtering window for all shots, however, is moved to slightly higher intensities by $\Delta I/I_0$, denoted by the dark gray shaded area, in order to compensate for the artefact. Here, an intensity bias of $\Delta I/I_0 = 0.0062$ is shown. (b) Difference between CEP maps from the PAPs obtained from the tagged laser shots and all laser shots, as in fig. 6.3 (b), for a laser shot offset of $N = 1$ but different values of intensity bias ($\Delta I/I_0 = 0$ corresponds to the second plot in fig. 6.3 (b)). An intensity bias of $\Delta I/I_0 = 0.0062$ minimizes the artefact. (c) Residual artefact strength (integral of the CEP map difference squared) as a function of the intensity bias for different laser shot offsets N .

the intensity distribution of all laser shots (black line in fig. 6.4 (a)), as the window of the intensity filter is moved along, while the intensity filter for the tagged shots stays at a constant position.

The successful elimination of the artefact by simply introducing an intensity bias, as demonstrated in this particular measurement, relies on the somewhat fortunate circumstance that the shape of the PAP is very regular and apparently exhibits a similar dependence on peak intensity as on average intensity. Thus, a balanced CEP retrieval is still possible, despite the preferential photoemission at higher peak intensities (for the same average intensity), by choosing an appropriate intensity range for the reference PAP. In general, however, the PAP at a higher peak intensity may not be approximated by a PAP at a higher average intensity. A change of the laser pulse's peak intensity at a given average intensity is usually accompanied by a non-trivial change of the spectral amplitude and phase and can result in an

unpredictable change of the PAP shape, especially for irregular or saturated PAPs resulting from non-ideal alignment of the stereographic ATI phase meter. Furthermore, the optimal intensity bias might depend on the position of the intensity filter window – although no significant intensity dependence was found in this measurement – and changes with the laser shot offset N , following the shape of the intensity autocorrelation. Since the optimal intensity bias at $N = 0$ cannot be determined directly due to the presence of the actual CEP modulation from the sample, it can only be approximated from adjacent N values. Still, the significant improvement of the data quality warrants using the intensity bias technique in this work (see subsection 6.2.2) to compensate for the lack of single-shot peak intensity monitoring during the measurements.

6.2 CEP dependence on bulk tungsten

Using bulk tungsten in this work for proof-of-principle CEP-dependence measurements has an advantage in comparison to minuscule nanotips or nanoparticles as the emission area is larger, resulting in more detectable signal. The W(110) crystal (MaTeck GmbH) was cleaned by flash heating via electron bombardment at 2000 °C for several tens of seconds to desorb oxides or contaminants in a portable sample preparation chamber at around $5 \cdot 10^{-8}$ mbar. This process can minimize photoelectron scattering on emission from the tungsten surface. The 10 kHz few-cycle laser system with a central wavelength of 670 nm described in subsection 3.3.1 was used for the experiments presented in this chapter.

6.2.1 Strong-field ATP

For the previous experiments described in chapter 5, the pulse duration of the NIR laser pulses was minimized at the sample in the PEEM chamber by maximizing the photoemission yield from hot spots at the sample upon NIR excitation via scanning the insertion of a fused silica wedge pair. However, it turned out to be difficult to determine the maximum multiphoton photoemission yield accurately in the PEEM while scanning the wedge insertion when a moderate laser peak intensity in the range of $10^8 \text{ W/cm}^2 - 10^9 \text{ W/cm}^2$ was used because the yield changes only weakly with the pulse duration around the maximum compared to the signal noise due to laser power fluctuations. In contrast, XUV generation is highly sensitive to the duration of the driving laser pulses and thus is well suitable as a means for optimizing the wedge scanning procedure. Therefore, HHG was first generated using the NIR laser pulses in a dedicated HHG beamline before the PEEM chamber which shares the laser source with the CEP-resolved PEEM experiment. The XUV yield from

the HHG was maximized by scanning the wedges to align for the shortest laser pulses at the HHG target. As a result, the NIR beam became more divergent due to a focusing mirror ($f = 40$ cm) used in the HHG chamber for generating the XUV. This unavoidably causes an uncertainty of $\pm 50\%$ in the estimation of the laser peak intensity at the sample in the PEEM because the divergent beam was clipped crudely by several apertures³ throughout the beamline. The p-polarized laser beam was focused onto the W(110) sample at an incidence angle of 65° with respect to the surface normal to a focal spot size of $\sim 30 \mu\text{m} \times 100 \mu\text{m}$ (FWHM) using a focusing mirror ($f = 25$ cm) and a pulse energy of ~ 323 nJ. This corresponds to a laser peak intensity I_0 of $(5.4 \pm 2.7) \cdot 10^{12}$ W/cm² at the sample. However, both the incoming as well as the reflected laser field contribute to the effective intensity at the sample surface where photoemission takes place [206]. The complex refractive index of tungsten at our central laser wavelength of 670 nm is $n = (3.93 + 3.01i)$ [207]. Using the Fresnel equation for the p-polarized electric field at our incidence angle of 65° yields the absolute value of the field reflectance coefficient as $|r| = 0.48$, or a field enhancement factor of $|r| + 1 = 1.48$. This corresponds to an intensity enhancement of 2.2 and hence a resulting effective laser peak intensity I_{eff} at the sample of $(1.2 \pm 0.6) \cdot 10^{13}$ W/cm². This effective intensity is about a factor of 2 – 3 smaller than the damage threshold intensity.

The very high count rate of photoelectrons generated from the W(110) surface due to illumination with high laser peak intensity had to be drastically reduced in order to avoid saturation of the detector. Therefore, the IEF option in the PEEM was used together with the ToF mode (see subsections 3.1.1 and 3.1.2 for the ToF mode in the PEEM) for the experiment described in this section. Note that it is not a common practice to use both the IEF and ToF at the same time because the IEF is designed to work with a regular non-dispersive camera (i.e. without a dispersive drift tube) for imaging spectroscopy in the PEEM [143]. A detailed description of an IEF and its functionality and applications can be found in literature [143, 208–210]. In our case, the IEF is used as a high-pass energy filter for allowing electrons above a certain kinetic energy to reach the DLD⁴. In order to investigate the intensity dependence of the CEP modulation from tungsten, two different laser intensities were used in the intensity-CEP-tagged PEEM measurements.

Fig. 6.5 (a) and (b) depict the CEP-averaged electron spectra measured by using the ToF mode at sample voltages (or bias voltages) U_{sample} of 30 V (at $I_{\text{eff}} =$

³A clipped beam results in a diffracted laser focal spot on the sample which complicates the calculation of the laser peak intensity, giving rise to an estimated systematic error of $\pm 50\%$ in the peak intensity.

⁴In the normal operation of the IEF mode the energy-filtered electrons are supposed to reach the fluorescence screen which is behind the DLD with the dispersive drift-tube disabled. See fig. 3.1 for the electron-optical design of the PEEM.

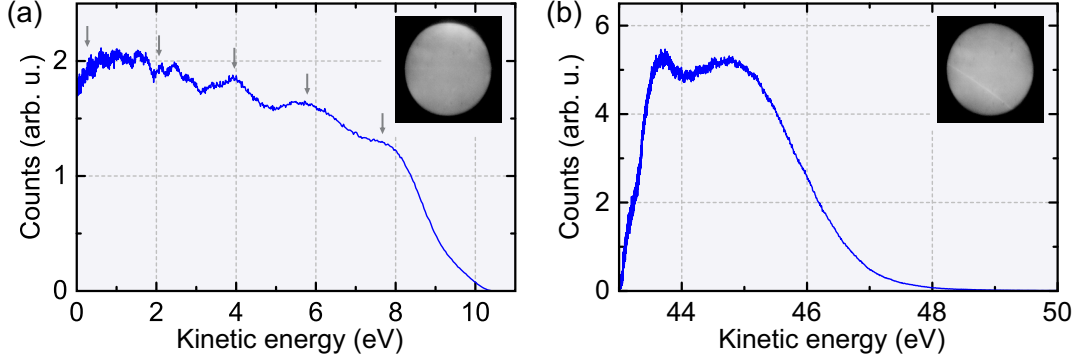


Figure 6.5: CEP-averaged photoemission spectra and their corresponding PEEM images at different laser intensities. (a) Kinetic energy spectrum integrated over the full W(110) area as shown in the inset, recorded at $I_{\text{eff}} = (1.6 \pm 0.8) \cdot 10^{12} \text{ W/cm}^2$ and $U_{\text{sample}} = 30 \text{ V}$. Gray arrows indicate the ATP peaks. Inset: PEEM image of W(110). The top part of the image appears brighter because of higher photoelectron yield, as the laser focus was moved off-center to the top of the image. (b) Kinetic energy spectrum integrated over the full sample area as shown in the inset, recorded at $I_{\text{eff}} = (1.2 \pm 0.6) \cdot 10^{13} \text{ W/cm}^2$ and $U_{\text{sample}} = 83.3 \text{ V}$. Inset: PEEM image of the sample area. A thin bright line is visible in the image and is possibly caused by an electrostatic lensing artefact due to a very high electron count rate and space charge effects in the PEEM. Both insets have a field of view of $\sim 40 \mu\text{m}$. See text for details.

($1.6 \pm 0.8) \cdot 10^{12} \text{ W/cm}^2$) and 83.3 V (at $I_{\text{eff}} = (1.2 \pm 0.6) \cdot 10^{13} \text{ W/cm}^2$), respectively. Note that for $U_{\text{sample}} = 30 \text{ V}$ the laser focal spot was moved away from the center of the image area for reducing the intensity impinging on the sample instead of using the IEF for high-pass filtering (as was done for $U_{\text{sample}} = 83.3 \text{ V}$) in order to record the full spectrum containing the ATP feature (see the inset in fig. 6.5 (a)). It is therefore not possible to estimate the laser peak intensity by using the minimum of the beam waist in this measurement. Rather, $I_{\text{eff}} = (1.2 \pm 0.6) \cdot 10^{12} \text{ W/cm}^2$ was estimated from another comparable measurement at similar experimental conditions. In principle, all photoelectrons with a starting kinetic energy $E_{\text{kin}} > eU_{\text{sample}} - eU_{\text{grid}}$, where U_{grid} is the retarding grid voltage of the IEF, can pass the grid and reach the detector [211]. Since the retractable DLD is inserted in the PEEM column and situated in front of the grid during the ToF operation, the grid has no retarding effect on the electrons arriving at the DLD. Instead, the DLD itself which is at the drift tube potential U_{drift} [212] acts as a retarder, thus the high-pass filtering condition can be rewritten as $E_{\text{kin}} > eU_{\text{sample}} - eU_{\text{drift}}$. U_{drift} was set to 40 V for achieving a decent time resolution by temporal dispersion inside the drift tube. The PEEM extractor voltage was set to 20 kV and the largest contrast aperture of $1500 \mu\text{m}$ was used in order to increase the transmission of high-energy electrons. For the electron spectrum obtained in fig. 6.5 (a), U_{sample} was set to 30 V , which is close to $U_{\text{drift}} = 40 \text{ V}$, in order to increase the time resolution. This therefore results in an artificial decrease

of the kinetic energy inside the drift tube to about 10 eV. By doing so, the ToF spectrum becomes stretched in time, resulting in an increased time/energy resolution. Note that the IEF does not function as a high-pass energy filter in this case because the passing energy ($eU_{\text{sample}} - eU_{\text{drift}}$) is still negative (i.e. electrons with all kinetic energies can pass). The energy axes shown in fig. 6.5 were appropriately shifted taking into account the effects from the IEF in order to depict the kinetic energies of photoelectrons leaving the W(110) surface.

Apparently, multiple peaks spaced by ~ 1.85 eV, corresponding to the photon energy of the laser pulses, are visible in the spectrum depicted in fig. 6.5 (a). The first and second peak are hardly distinguishable from the noise background because these low-energy electrons are moving slower than the high-energy electrons inside the drift tube, making them more susceptible to surrounding stray fields and loss, which explains why the first and second peak exhibit a lower yield in comparison to what has been reported [97, 99, 100, 104]. These equally spaced peaks have been observed in polycrystalline copper [97] and gold [99], Ag(100) [100], Pt(111) [98], Cu(001) [101] and a W(310) nanotip [104]. The work function of W(110) is 5.3 eV⁵ hence absorption of at least 3 photons is required for multiphoton photoemission, as evident by the commonly observed first or lowest-order peak at around 0.25 eV. Above the photon order of 3, absorption of additional photons gives rise to the ATP peaks observed in the spectrum. A maximum photon order of 7 and a cutoff energy range of 8 eV – 11 eV are observed in our case. The Keldysh parameter (see eqn 2.5 and subsection 5.2.1) is found to be $\gamma = 6.3 \pm 2.6$ at $I_{\text{eff}} = (1.6 \pm 0.8) \cdot 10^{12}$ W/cm², indicating that the emission process is close to the transition regime between multiphoton ($\gamma \gg 1$) and tunneling ionization ($\gamma \ll 1$). The majority of photoelectrons observed here are assumed to originate from a high density of d-band states just below the Fermi level [17]. In a semiclassical theoretical model, ATP peaks can be understood as spectral interference between at least two electron wave packets emitted from the metal surface during subsequent cycles of the laser pulse, which then rescatter elastically at the surface after a delay of approximately one optical cycle period T . This modulates the resulting kinetic energy spectrum at the optical frequency, $f = 1/T$, creating sidebands spaced by $\Delta E \approx h/T = h/2.23 \text{ fs} \approx 1.85$ eV [12, 214, 215]. Notably, a moderate space charge effect (≥ 1 electron per pulse) occurs at this laser peak intensity regime ($\sim 10^{12}$ W/cm²); however, this does not destroy the ATP feature albeit the modulation contrast is reduced due to broadening as compared to experiments done without space charge effects [99, 104].

The cutoff region increases from 8 eV – 11 eV to 45 eV – 49 eV when the peak intensity is increased from $(1.6 \pm 0.8) \cdot 10^{12}$ W/cm² to $(1.2 \pm 0.6) \cdot 10^{13}$ W/cm² (see

⁵This value was obtained from a private communication with Jürgen Schmidt, who derived it from photoelectron streaking spectroscopy experiments using XUV [213].

fig. 6.5 (b)). In the latter case, U_{sample} was set to 83.3 V, which only allows electrons with $E_{\text{kin}} > 43.3$ eV to pass the filter and reach the DLD. In fig. 6.5 (b), a kink at ~ 43.7 eV is believed to be an artefact introduced by the combined use of IEF and DLD in ToF mode, and is therefore not an actual energy peak. Although here the Keldysh parameter $\gamma = 2.3 \pm 0.9$ (at $I_{\text{eff}} = (1.2 \pm 0.6) \cdot 10^{13}$ W/cm²) is outside the tunneling regime ($\gamma \ll 1$), the emission process cannot be separated from strong-field effects when sub-cycle dynamics takes place [216]. The tunneling process has been successfully used to elucidate the strong-field signatures of a plateau and the cutoff observed from tungsten nanotips [12, 214, 217]. In those cases, $\gamma \approx 2$ could be reached via the assistance of field enhancement at the tips at a moderately low laser intensity of $\sim 10^{11}$ W/cm². Rescattered electrons in the tunneling process – which gain additional energy as they recollide with their parent ions and backscatter elastically into the continuum – are responsible for the plateau structure and high-energy cutoff in the photoelectron spectra. The rescattering effect has first been identified in atomic and molecular gases [103, 218] and has also been observed recently at dielectric nanospheres [199], metal nanotips [12, 43], gold nanoparticles [44] and silver clusters [202]. In our case, as depicted in fig. 6.5 (b), the high-energy cutoff region around 45 eV – 49 eV is also attributed to the sub-optical-cycle nature of the rescattering effect. Further details on CEP sensitivity of the rescattering effect are provided in subsection 6.2.2. In fact, ATP peaks from solids are also expected to arise in the tunneling regime as suggested by experimental evidence of ATI peaks already found in atomic gases [103] when moving from the plateau to the high-energy cutoff. However, it remains unclear why so far ATP peaks from solids have not been observed in the strong-field regime. Similarly, no ATP peaks are visible in the high-energy photoelectron spectrum displayed in fig. 6.5 (b) in contrast to the ATP structure appearing in the low-energy spectrum shown in fig. 6.5 (a). The space charge effect at the high peak intensity used here ($\sim 10^{13}$ W/cm²) is dominant ($\gg 1$ electron per pulse) and may have washed out the peak structure in the high-energy spectrum if there was any. Furthermore, the use of the IEF at a high-pass energy of 43.3 eV (to avoid saturation of the detector, as pointed out before) only allows electrons within a narrow kinetic energy range around the cutoff to reach the detector where ATP peaks may not be present anymore. It should be noted that an exponential decrease of the count rate is found at the cutoff energy in most published work from solids [104]. While this is also found in our case for the low-energy spectrum (see fig. 6.5 (a)), the cutoff region is more broadened and does not show a clear exponential decrease for the high-energy spectrum (see fig. 6.5 (b)), which is likely a consequence of the strong space charge broadening in that case.

6.2.2 Attosecond control of photoemission with CEP

In the following, CEP-resolved photoemission studies from a bulk W(110) surface utilizing the newly established intensity-CEP-tagged ToF-PEEM technique are presented for the first time. The experimental conditions for the results presented here have already been described before (see subsection 6.2.1). The laser pulse duration retrieved from the PAPs in these measurements is approximately 5.0 fs FWHM (data not shown), corresponding to 2.2 cycles at a 670 nm central wavelength. Fig. 6.6 shows the CEP spectrograms and CEP modulation analysis from the W(110) sample for $U_{\text{sample}} = 30 \text{ V}$ (at $I_{\text{eff}} = (1.6 \pm 0.8) \cdot 10^{12} \text{ W/cm}^2$) and $U_{\text{sample}} = 83.3 \text{ V}$ (at $I_{\text{eff}} = (1.2 \pm 0.6) \cdot 10^{13} \text{ W/cm}^2$), respectively. Here, a CEP bin size of 10° is chosen for plotting the CEP spectrograms, which results in 36 bins over the entire 2π range. The recorded data is extended to cover a CEP range from 0 to 4π (effectively repeating the $0 - 2\pi$ range) for better viewing. The typical rms phase noise of the CEP tagging technique lies within 210 mrad or $\sim 12^\circ$ [164, 166], which justifies the choice of the CEP bin size. The corresponding CEP-averaged electron spectra for these spectrograms are shown in fig. 6.5. To enhance the visibility of the CEP effect, the CEP spectrograms are obtained by normalizing the CEP-resolved photoelectron spectra to their respective CEP-averaged spectrum (see fig. 6.6 (a)-(c) and (f)-(h)). Since the absolute CEP cannot be measured by the phase tagging technique, the arbitrary CEP offset φ_0 (see subsection 3.3.2) in fig. 6.6 (f)-(h) is chosen such that the highest electron yield at the cutoff energy is located at CEP $\varphi = -\pi/4$, which is well-known from literature for the strong-field regime [12, 219]. Applying the same offset to the low-energy measurement ($U_{\text{sample}} = 30 \text{ V}$), the resulting CEP modulation in fig. 6.6 (a)-(c) is shifted by $\varphi \approx \pi/4$ with respect to the case of the high-energy measurement ($U_{\text{sample}} = 83.3 \text{ V}$). It cannot be excluded, however, that the relative CEP offset found between the two measurements originates from a change in the shape of the PAP as a result of laser drift despite being recorded at the same day without readjustments of the laser parameters other than the intensity on the PEEM sample.

As discussed in chapter 5 and section 6.1, a CEP artefact which originates from a laser-intensity-dependent CEP map is introduced when using the phase tagging technique. This artefact can be comparable in magnitude to a weak actual CEP effect (modulation depth of a few percent or less) and therefore can easily obscure it when not corrected. This is clearly demonstrated in fig. 6.6 (a), which depicts CEP retrieval without intensity tagging, i.e. using the intensity-averaged CEP map for all detected photoemission events. No actual CEP modulation with 2π periodicity is visible, as it is entirely buried underneath the strong artefact. After intensity-resolved CEP retrieval using intensity tagging (see subsection 6.1.1), the artefact is significantly reduced, partially revealing the underlying 2π CEP modulation (see

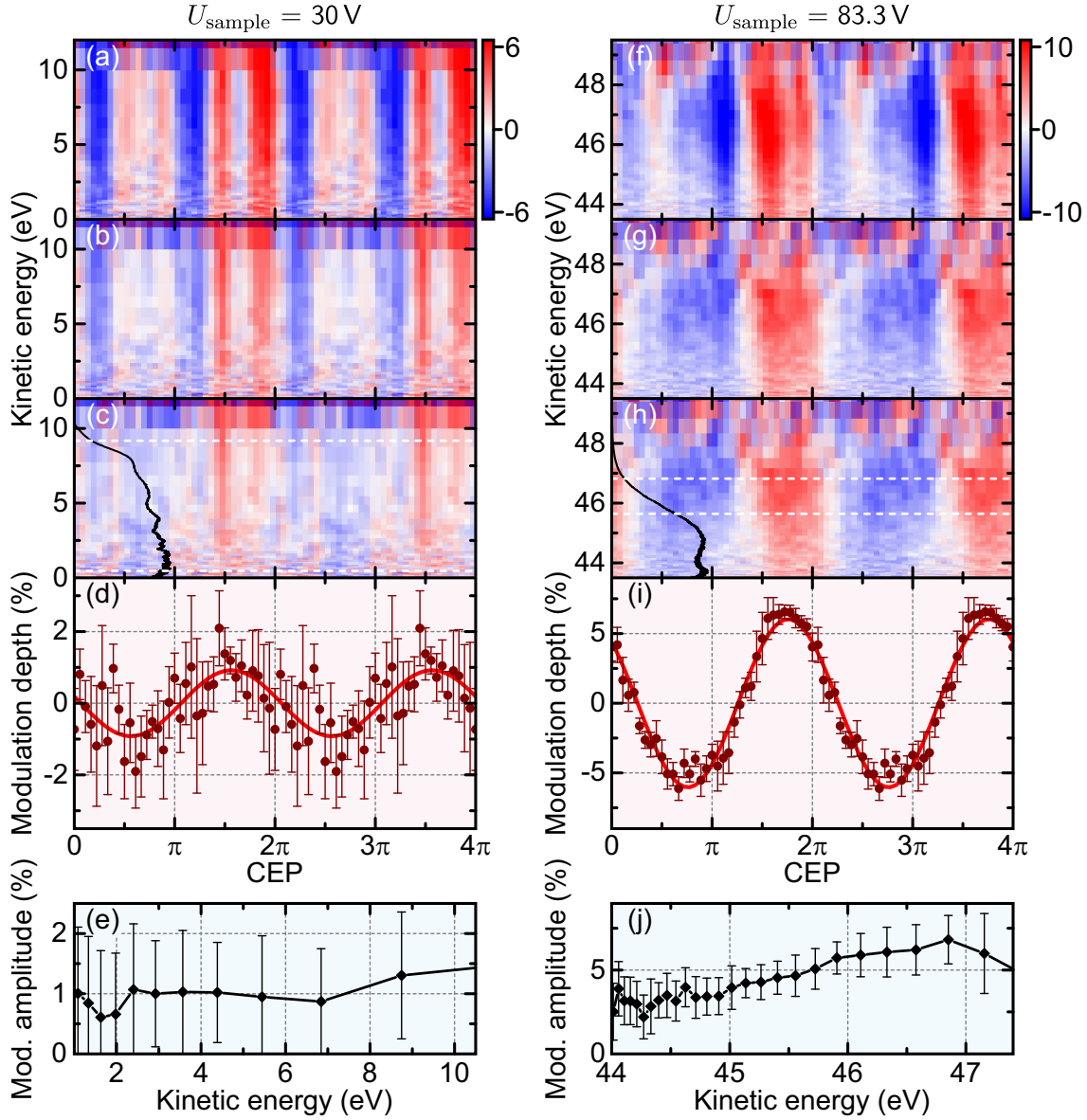


Figure 6.6: CEP-dependence of the photoemission from W(110) for $U_{\text{sample}} = 30 \text{ V}$ (a-e) and $U_{\text{sample}} = 83.3 \text{ V}$ (f-j). (a-c), (f-h) CEP-resolved photoelectron spectra normalized to the respective CEP-averaged spectrum; the color bars show the modulation depth in percent. The CEP retrieval is demonstrated without intensity tagging (a, f), with intensity tagging but without artefact correction (b, g) and after artefact correction by applying an appropriate intensity bias (c, h). The black curves in (c) and (h) show the respective CEP-averaged photoelectron spectra from fig. 6.5 as a guide to the eye (arbitrary scaling). (d, i) CEP modulation lineouts taken from (c) and (h), respectively, averaged over a kinetic energy interval denoted by the dashed white lines in (c) and (h). The error bars represent the combined systematic (artefact) and statistical (noise) error and the red solid lines are cosine fits. A 2π modulation with amplitudes of $\sim 0.9\%$ and $\sim 6.0\%$ is evident for $U_{\text{sample}} = 30 \text{ V}$ and $U_{\text{sample}} = 83.3 \text{ V}$, respectively. (e, j) Fitted CEP modulation amplitudes for different kinetic energies. The error bars represent standard deviations of the fitted amplitudes. See text for details.

fig. 6.6(b)). However, a residual artefact still remains, which is attributed to peak intensity dependence rather than average intensity (i.e. pulse energy) dependence, since only the latter was monitored by the intensity tagging technique. In the final step, an appropriate intensity bias is introduced (here, $\Delta I/I_0 = 0.0055$) in order to correct for the difference between average and peak intensity dependence, as has been explained in subsection 6.1.3. The result is shown in fig. 6.6(c) where the artefact is considerably reduced well below the magnitude of the actual CEP modulation from the sample. Fig. 6.6(d) shows a lineout of the CEP spectrogram, integrated over a kinetic energy range between 0.2 eV and 9.2 eV, as indicated by the white dashed lines in fig. 6.6(c). The error bars are calculated from the statistics of the CEP spectrogram lineouts for tag list offsets of $N = \{-9 \dots 9\}$ (except $N = 0$), since no actual CEP effect is present for tag list offsets other than $N = 0$ and any deviation from zero is therefore attributed to systematic (mean value for all N) and statistical (spread for all N) error, respectively. A cosine fit reveals a 2π periodicity of the photoemission yield with a modulation depth of $\sim 0.9\%$, demonstrating the high sensitivity of the phase tagging technique when applying intensity tagging and appropriate corrections. Despite the considerable noise of the data, the standard error of the fitted phase offset is only 155 mrad, which corresponds to a timing accuracy of 55 as at our central wavelength of 670 nm. The modulation amplitudes, i.e. the maxima of the fitted modulation depth curves for different kinetic energies, are displayed in fig. 6.6(e) with the error bars denoting rms errors of the fits. It can be seen that there is no significant change of the modulation amplitude with kinetic energy within the margin of error.

For the high-energy photoelectron spectrum, a CEP modulation of the same 2π periodicity is clearly visible when using intensity tagging, as shown in fig. 6.6(g), while it is overlaid with a strong artefact when no intensity tagging is applied (see fig. 6.6(f)). A small residual artefact can be further corrected by applying an appropriate intensity bias (here, $\Delta I/I_0 = 0.0062$), as shown in fig. 6.6(h). However, the improvement is not as significant as in fig. 6.6(c) since the CEP modulation depth is much bigger here in comparison to the residual artefact. The lineout of the CEP spectrogram integrated over a spectral range of 45.6 eV – 46.8 eV (cutoff region, denoted by the white dashed lines in fig. 6.6(h)) is shown in fig. 6.6(i) with the error bars calculated as explained above for $U_{\text{sample}} = 30$ V. A cosine fit (red line) reveals a modulation depth of 6.0%. Here, the standard error of the fitted phase offset is as low as 18 mrad, which implies a remarkable temporal precision of 6.4 as at our central wavelength. This is attributed to the excellent data quality in this measurement achieved by intensity tagging and additional artefact suppression by applying an intensity bias. Fig. 6.6(j) shows the CEP modulation amplitude at different kinetic energies. Interestingly, the modulation amplitude increases steadily

from $\sim 3.4\%$ at 44.7 eV to $\sim 6.8\%$ at 46.8 eV. It seems to decline after 46.8 eV as the cosine fitting becomes unreliable with the substantially reduced signal-to-noise ratio when approaching the cutoff limit.

Next, we discuss the interpretation of our experimental findings for these two intensities (at $U_{\text{sample}} = 30\text{ V}$ and $U_{\text{sample}} = 83.3\text{ V}$). In this work, moderately pronounced CEP effects with a period of 2π have been observed from a bulk tungsten surface, albeit the measurements were performed in a regime with significant space charge effects. In our case, a CEP modulation depth of $\sim 1\%$ was obtained at a peak intensity of $(1.6 \pm 0.8) \cdot 10^{12}\text{ W/cm}^2$ ($\gamma = 6.3 \pm 2.6$), falling within the multiphoton photoemission regime. Such a modulation depth is ~ 10 times higher than what had been detected from a gold surface⁶, where a comparable peak intensity was used at a grazing incidence angle [54, 198]. It is speculated that working in a moderate space charge regime might broaden the energy spectrum in fig. 6.5 (a) and fig. 6.6 (a)-(c) by approximately 0.3 eV – 2 eV [34]. M. Krüger *et al.* show an increase of CEP modulation depth with kinetic energy, remarkably as high as $\sim 100\%$ at the cutoff energy, using a tungsten nanotip [12]. However, we could not observe this in our ATP spectrum, probably because of a substantially larger emission site ($\sim 30\text{ }\mu\text{m} \times 100\text{ }\mu\text{m}$) with inhomogeneous local intensities as compared to a highly localized emission site at the tip's apex ($\sim 10\text{ nm}$ radius), which is well below the laser focal spot size. Secondly, the average surface roughness of our tungsten sample is $\sim 2\text{ nm}$ ⁷, which reduces the fraction of the effective area that is exposed to the normal component of the electric field and thus weakens the overall CEP sensitivity, since only the normal component of the electric field is responsible for CEP-dependent modulation of the photoemission yield [54]. Theoretical works [54, 219] suggest that CEP sensitivity in multiphoton photoemission tends to increase for pulse durations approaching a single laser cycle.

In the tunneling regime as depicted in fig. 6.6 (f)-(j), the effect of the CEP on the photoemission yield becomes much more pronounced, amounting to a maximum modulation depth of almost 7% at 46.8 eV, in comparison to only $\sim 1\%$ in the multiphoton photoemission regime (see fig. 6.6 (a)-(e)). As expected, we observe a stronger CEP dependence of the photoemission yield at higher intensities. This is in agreement with the CEP-dependent tungsten nanotip experiments [12], where the CEP modulation becomes stronger for higher kinetic energies. This is further corroborated by the observed gradual increase of modulation depth as a function of kinetic energy, reaching $\sim 7\%$ before the high-energy cutoff and transition into

⁶According to private communication with Alexander Apolonski, a CEP modulation depth of less than 0.1% was obtained in their case.

⁷This surface roughness value is based on the product specification. A surface characterization is needed to confirm the actual roughness.

background noise, as mentioned before (see fig. 6.6(j)). This behavior is also expected for the low-intensity case. However, since the CEP modulation depth is very small at that intensity, no energy dependence of the modulation could be observed reliably within the margin of error. As aforementioned, there is a phase difference of $\sim\pi/4$ between the CEP modulation for the two different intensities used (compare fig. 6.6(d) and (i)). This might indicate a transition from the multiphoton to the strong-field regime as the intensity is increased from $(1.6 \pm 0.8) \cdot 10^{12} \text{ W/cm}^2$ to $(1.2 \pm 0.6) \cdot 10^{13} \text{ W/cm}^2$. It has been predicted and shown that multiphoton photoemission has a phase shift of π compared to the tunneling regime in terms of CEP dependence [12, 219]. The discrepancy in our case might imply that the illumination conditions for one or both measurements lie within an intermediate regime between these two emission processes. However, as pointed out before, an instrument-related cause for this phase shift cannot be entirely excluded.

In the presence of space charge effects, concerns arise regarding the possible impact of electron-electron interaction on the measured photoelectron spectra and CEP modulation. We briefly discuss the space charge effects in this study. For low illumination intensities ($U_{\text{sample}} = 30 \text{ V}$), an estimated 1 – 3 electrons per pulse are emitted from the sample, indicated by the number of electrons per second detected at the DLD after considering the transmission losses inside the PEEM. As discussed above, such a moderate space charge effect is expected to introduce energy broadening of a few electronvolts at the low-energy cutoff as well as the high-energy cutoff of the photoelectron spectrum [34, 40, 188]. Despite this broadening, the ATP peak structure remains clearly visible (see fig. 6.5(a)). Quantifying the number of electrons per pulse for the high-energy measurement ($U_{\text{sample}} = 83.3 \text{ V}$) is not possible from the experimental data, as only electrons with $E_{\text{kin}} > 43.3 \text{ eV}$ can pass the filter and are detected by the DLD, while all other electrons are lost. As a rough estimation, based on a third-order nonlinear process and an increase in intensity by an order of magnitude as compared to the low-energy case, we expect a photoemission yield on the order of 10^3 electrons per pulse, most of which are filtered out by the IEF. The cutoff energy originating only from the rescattered electrons, E_{cutoff} , can be approximated by an analytical formula [220], which has been found very useful for nanotips [221, 222] and plasmonic nanostructures [201, 223]:

$$E_{\text{cutoff}} \approx 10.007U_p + 0.538\phi, \quad (6.2)$$

where U_p is the ponderomotive potential (see subsection 2.1.2) and ϕ the work function. At $(1.2 \pm 0.6) \cdot 10^{13} \text{ W/cm}^2$ ($U_{\text{sample}} = 83.3 \text{ V}$), we obtain a cutoff energy $E_{\text{cutoff}} \approx 8 \text{ eV}$, which is far below the observed cutoff at around 49 eV. Note that eqn 6.2 is strictly valid only for the tunneling regime where rescattering processes

are considered, therefore it cannot be used to justify the cutoff energy of the spectra in fig. 6.5(a) and fig. 6.6(a)-(c). It is noteworthy that a cutoff region of 7 eV – 10 eV has been reported in the ATP photoemission from flat metal surfaces for low intensities ($10^8 \text{ W/cm}^2 - 10^{10} \text{ W/cm}^2$) [97, 99, 101]. Therefore, the actual cutoff in the high-energy photoelectron spectrum in fig. 6.5(b) and fig. 6.6(f)-(h) can be significantly higher than $\sim 8 \text{ eV}$ since the intensity here is one order of magnitude higher than in the case of $U_{\text{sample}} = 30 \text{ V}$ (fig. 6.5(a)). Apparently, the cutoff law for the tunneling regime (eqn 6.2) alone cannot account for our experimental findings for a tungsten metal surface, hence, other causes have to be considered and remain to be investigated. It is very likely that the main cause for this high energy cutoff around 49 eV is a severe space charge broadening ($\gg 1$ electron per pulse), however, the exact number of electrons per pulse cannot be determined in this case. It has been theoretically shown that an emission of 30 electrons per pulse can extend the cutoff energy to $\sim 40 \text{ eV}$ in a gold nanotip [40]. Although space charge broadening is expected to have a stronger effect at a nanotip as compared to a bulk surface due to the high localization of the photoemission, we also expect to produce significantly more electrons per pulse ($\sim 10^3$, as estimated above) owing to the high nonlinearity of the photoemission process. A space charge broadening of the high-energy part in the spectrum is caused by Coulomb repulsion where the fast electrons are separated from the slow electrons and accelerated by the electric field of the electron cloud [40, 224], which results in an energy gain and thus a shift of the cutoff to higher energies. Despite a more severe space charge interaction in the case of $U_{\text{sample}} = 83.3 \text{ V}$, a stronger CEP modulation is observed, indicating that these CEP-sensitive rescattered electrons are not significantly perturbed by space charge, which confirms previous predictions [40]. Further theoretical and experimental analysis of these space charge effects is required to elucidate the nature of this CEP dependence.

6.3 CEP dependence on gold nanostructures

We extend this work using the CEP-intensity-tagged PEEM technique to study lithographically fabricated, supported gold nanostructures. Briefly, a series of gold nanotriangles with varying sizes were fabricated onto an ITO-coated glass substrate using EBL by the group of Hiroaki Misawa. An ultrathin 2-nm-thick titanium adhesion layer was added between the 40-nm-thick gold layer and ITO-coated glass substrate for improving the nanostructure quality. For fabrication details, see subsection 3.4.2. The same laser pulses as in the previous section with a central wavelength of 670 nm were used for sample illumination at an incidence angle of 65° with respect to the surface normal of the sample and the polarization of the laser was set parallel

to the nanotriangle axis. At this polarization, no normal component of the electric field is present at the sample plane and thus no CEP modulation is expected for electrons emitted from the bulk gold. Only electrons emitted from the tips of the triangles along the sample plane can experience an electric field component normal to the tip and thus a possible CEP modulation. The pulse length estimated from its corresponding PAP is approximately 5.4 fs (data not shown). A lower laser peak intensity on the order of $\sim 10^{10}$ W/cm² was used here in order to avoid sample damage and excessive space charge broadening of the PEEM image. The PEEM was operated in ToF mode utilizing the DLD without an IEF (cf. subsection 6.2.1). A high PEEM extractor voltage up to 22 kV was used to increase the spatial resolution. In addition, the largest contrast aperture of 1500 μm was used to allow the transmission of electrons with all kinetic energies.

Fig. 6.7 (a) shows the PEEM image of four identical arrays of nanotriangles with a vertex angle of $\sim 32.5^\circ$, starting from the smallest altitude of ~ 90 nm which is increasing in length by 20 nm per step, from the bottom to the top of the PEEM image. An Hg arc UV lamp was used for the sample illumination. Upon broadband few-cycle laser excitation, several hot spots (brighter spots compared to others) due to plasmonic resonance from the nanotriangles around the center of the PEEM image are observed (see fig. 6.7 (b)). These hot spots most likely originate from the apexes of the triangles since the laser's polarization is along the triangles' axes. We assume that the corners at the triangles' bases should not be resonantly excited because of this polarization direction. However, photoemission from the entire nanotriangle surface is also expected, albeit not enhanced by plasmon resonance, particularly around the top and bottom part of the image where the spots are less bright, as the triangles are not resonant due to their geometry. A very strong hot spot is spotted on one nanotriangle, located at the top right of the PEEM image, presumably caused by some surface defect which can result in surface roughness. It is widely known that surface roughness, an intrinsically nanoscale phenomenon, can exhibit a high local field enhancement [225, 226], leading to a very high photoemission yield upon light excitation (see subsection 5.2.1). Here, the laser illumination was homogenous over the entire sample area (~ 5 μm field of view) as the laser focal spot size was approximately ~ 30 $\mu\text{m} \times 100$ μm (FWHM). Therefore, each nanotriangle in the field of view was exposed to approximately the same and well-defined laser intensity. Note that the laser intensity used here was at the onset of the space charge regime in order to maximize the photoemission yield to achieve a reasonable acquisition time while maintaining a good enough spatial resolution to distinguish individual triangles despite some space charge blurring of the image.

As discussed in section 6.1, PAPs for different intensity intervals can be extracted from the intensity-tagged measurement. Several exemplary PAPs for different inten-

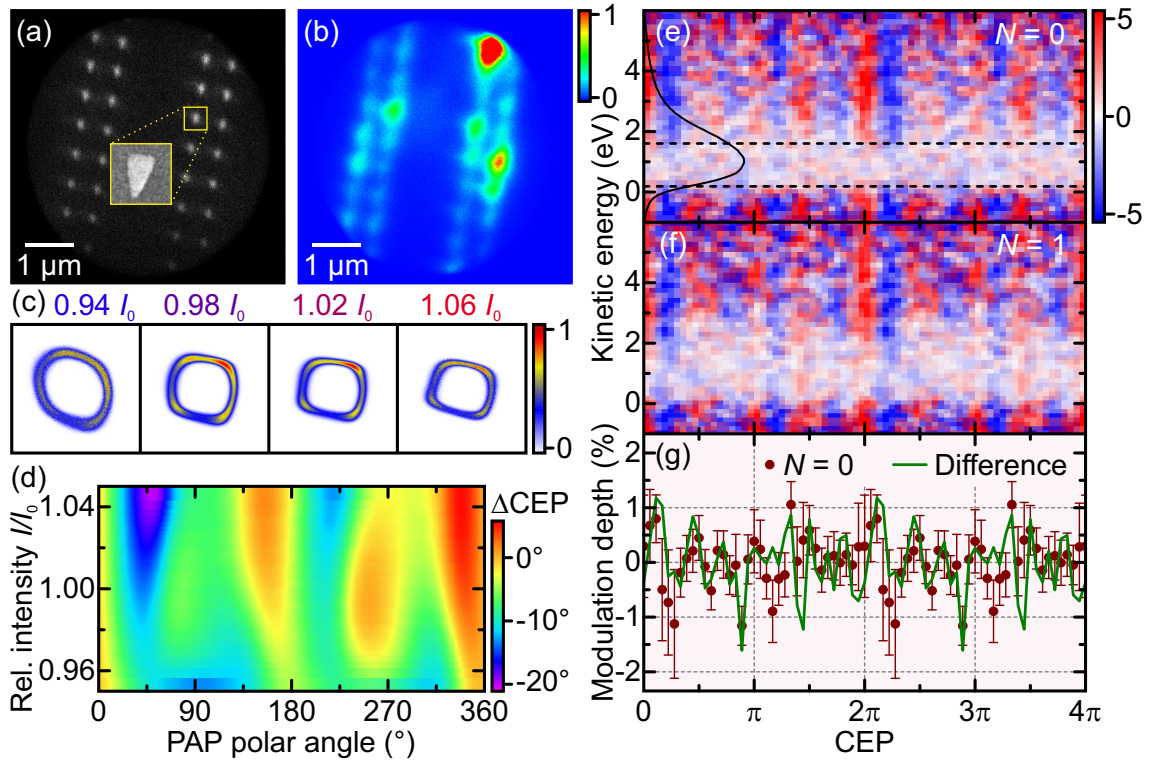


Figure 6.7: CEP-resolved ToF-PEEM results from supported gold nanotriangles using the CEP-intensity-tagging technique. (a) PEEM image of arrays of gold nanotriangles of different sizes using Hg lamp illumination. The inset (yellow box) shows a zoomed-in SEM image of one of the nanotriangles. See text for details of the nanostructure dimensions. (b) PEEM image of the same sample area as shown in (a), acquired with few-cycle laser illumination. Different photoemission yields are visible from different triangles as well as a reduced spatial resolution due to slight space charge effects. The colorbar shows the normalized counts. (c) Exemplary PAPs for this measurement filtered around different intensities with respect to the mean intensity I_0 within a window of $0.01I_0$ width each. The asymmetry axes are scaled from -1 to 1 as in fig. 6.1 (a). (d) Full two-dimensional CEP/intensity map, showing the difference from the ideal CEP map on the color scale, as illustrated in fig. 6.1 (d). Here, the CEP/intensity map is quite irregular and exhibits a complex and non-monotonous intensity dependence. (e) CEP-resolved spectrogram normalized to the CEP-averaged spectrum (intensity-resolved CEP retrieval as in fig. 6.6 (b) and (g)) of the whole sample area excluding the very strong hot spot in the top right; the color bar shows the modulation depth in percent. No intensity bias was applied here (cf. fig. 6.6 (c) and (h)), as it does not remove the residual artefact (sharp vertical stripes) due to the irregularity of the CEP/intensity map. The black curve shows the CEP-averaged photoelectron spectrum as a guide to the eye (arbitrary scaling). (f) CEP-resolved spectrogram as in (e) but with the tag list deliberately shifted by one laser shot ($N = 1$, see subsection 6.1.2). The persistence of the sharp vertical lines confirms their attribution to the residual artefact. (g) Lineout (red dots) taken from the CEP spectrogram in (e), averaged over a kinetic energy interval denoted by the dashed black lines in (e). The error bars represent the combined systematic (artefact) and statistical (noise) error. The green line shows the difference between the lineouts for $N = 0$ (e) and $N = 1$ (f), revealing no observable CEP modulation within the noise limit of $\sim 0.6\%$.

sities around the average intensity I_0 in this measurement are plotted in fig. 6.7 (c), each for an interval of $0.01I_0$ around the respective relative intensity. The shape of the PAPs as well as the polar distribution of counts (indicated by the color bar) change as a function of relative intensity. Additionally, the PAPs also rotate slightly and their size decreases with increasing intensity from $0.94I_0$ to $1.06I_0$. Such a significant and non-monotonous alteration of the PAP as a function of intensity therefore results in a highly irregular CEP/intensity map (see fig. 6.7 (d) and cf. fig. 6.1 (d)). This in turn prevents a successful correction of the residual artefact related to peak intensity dependence by applying an intensity bias, as introduced in subsection 6.1.3, since a PAP for higher peak intensities (as preferred by photoelectrons, i.e. tagged shots, see subsection 6.1.3) cannot be simply approximated by a PAP at higher average intensities in this case. The result can be seen in fig. 6.7 (e) where sharp vertical stripes originating from the artefact are visible in the CEP-resolved spectrogram after intensity-resolved CEP retrieval. No intensity bias was applied here, as it does not improve the residual artefact. Note that the strong hot spot in the top right of the image was excluded in the CEP-resolved data analysis since it most likely originates from surface roughness which does not have a well-defined shape. To confirm that the sharp vertical stripes in the spectrogram are indeed due to the residual artefact, the tag list was shifted by one event, $N = 1$, and the sharp vertical stripes still persist after the shift, as depicted in fig. 6.7 (f). No actual CEP modulation should be observed after shifting the tag list by one event, while the intensity-related artefact has been found to persist nearly unchanged after shifting by several events and only fades away after shifting by a number of events corresponding to several seconds (see subsection 6.1.2). In fig. 6.7 (g), a lineout (red dots) is taken from the CEP spectrogram in fig. 6.7 (e), integrated over a spectral range of $0.2\text{ eV} - 1.6\text{ eV}$, denoted by the dashed black lines in fig. 6.7 (e). Clearly, no CEP modulation with a periodicity of 2π is observed except for the artefact within the margin of error. The error bars were determined in the same way as described previously for the experiments on tungsten (see subsection 6.2.2). To confirm the absence of an observable CEP modulation, the difference between the lineouts for $N = 0$ and $N = 1$ (also from the same spectral range in fig. 6.7 (f)) is shown as the green line. The artefact is canceled out, since it is very similar in both cases; however, there is still no observable CEP modulation within the noise limit of $\sim 0.6\%$ (standard deviation of the lineout for $N = 1$).

It is possible that a small CEP modulation below $\sim 0.6\%$ is present but buried within the measurement noise and residual artefact. This number therefore represents an upper limit of the CEP effect from these nanotriangles at our experimental conditions. Our conclusion is supported by a similar work demonstrated by W. P. Putnam *et al.* in which a CEP modulation of $0.005\% - 0.1\%$ was observed

in the total photocurrent emitted from plasmonic nanotriangles with a resonance within and around the excitation wavelength [197]. Analyzing single nanotriangles for their CEP dependence by applying appropriate ROIs also does not reveal any CEP modulation (apart from the artefact) but only increases the noise level due to limited electron counts. In addition, the same CEP analysis was also carried out on the strong hot spot in the top right of the image but the same result as for the individual nanotriangles was obtained. The total photoelectron count for the entire PEEM image is about $6.6 \cdot 10^6$ over a measurement time of 142 min, and $4.2 \cdot 10^6$ if the strong hot spot is excluded. In order to reliably detect a CEP modulation depth of $\sim 0.1\%$, as W. P. Putnam *et al.* found for this type of structures, we need to improve the sensitivity of our system by about one order of magnitude. This would require collecting about 100 times more data from a statistical-error point of view. Furthermore, the residual artefact needs to be corrected either by adjusting the laser settings which produce a favorable PAP or by peak intensity tagging as suggested in subsections 6.1.2 and 6.1.3. A hundred-fold acquisition time (about 10 days) would stress the boundaries of feasibility, since a substantial drift in laser and environment parameters over such a long measurement time becomes increasingly challenging to compensate, although successful attempts have been demonstrated [171]. Using a higher intensity to increase the photoemission yield would lead to severe space charge broadening and loss of image resolution, since the intensity used here is already at the onset of space charge broadening. The most promising way to improve the intensity-CEP-tagged ToF-PEEM's sensitivity sufficiently to resolve such small CEP modulation depths is using a high-repetition-rate laser system in the range of hundred kilohertz to low-megahertz [227–229].

Conclusions and outlook

In summary, this work demonstrates the development of a ToF-PEEM as a versatile tool for studying photoemission from metal surfaces (unstructured and nanostructured samples) with attosecond temporal and nanometer spatial resolution. The first part of this work describes the experimental attempts of realizing the atto-PEEM concept based on the theoretical proposal by M. I. Stockman *et al.* [117] almost a decade ago. Static atto-PEEM experiments without a pump-probe scheme were carried out using a 1 kHz HHG source on lithographically fabricated gold nanostructures as a first step. The experimental results demonstrated an achievable spatial resolution of ~ 200 nm using ~ 350 as XUV pulses of 93 eV photon energy. Our spatial resolution with XUV imaging is comparable to another research group from Lund University, Sweden, who used 1 kHz attosecond XUV pulse trains with a lower photon energy of 30 eV [35]. In addition, we have performed microspectroscopy and were able to identify the core and valence band electronic states from the investigated sample. The most intriguing discovery that we found in the course of this experiment is that the primary valence band electrons, which carry the attosecond temporal information imprinted during the XUV excitation, are not influenced by space charge effects. This is essentially crucial for atto-PEEM as snapshots of the streaked photoelectrons in the instantaneous acceleration of attosecond nanoplasmonic fields can be recorded in an optical-pump/XUV-probe scheme. However, working with a 1 kHz XUV source has turned out to be very challenging as the measurements suffered greatly from space charge effects at such a low repetition rate. The spatial resolution can only be improved by avoiding space charge, which requires using less XUV intensity, thus further extending the data acquisition time for a pump-probe scan beyond feasibility.

As high-repetition-rate attosecond XUV sources are becoming more readily available [191–195], the aforementioned data acquisition time is expected to be vastly

reduced from some tens of hours down to several minutes, facilitating reasonably fast and reliable measurements. For instance, it has been shown that the image acquisition time was reduced by a factor of ~ 10 when the repetition rate was increased by a factor of ~ 200 while the spatial resolution was improved about 3-fold [133, 138]. Nevertheless, we foresee possible new challenges, which are not present in the case of PEEM experiments using femtosecond laser pulses. The first and foremost issue is chromatic aberrations caused by the large energy bandwidth of XUV-generated photoelectrons. Fortunately, this can be resolved by applying energy-filtering in our ToF-PEEM to particularly select the primary valence band electrons from the secondary electron background, which we have demonstrated in this work. The next steps towards the realization of atto-PEEM will encompass energy-filtered imaging of fast valence band electrons and a spatial resolution down to 100 nm or even lower when low-megahertz attosecond XUV sources are available. Alternatively, an aberration-corrected PEEM equipped with an energy analyzer [230] can be employed specifically for high-megahertz XUV sources since it does not depend on repetition rate. This type of PEEM has been proven to achieve a theoretical spatial resolution of ~ 4 nm [230], which will possibly enable energy-resolved imaging of the instantaneous electron acceleration in a highly localized nanoplasmonic field within a ~ 1 nm region, as originally proposed by M. I. Stockman *et al.* [117]. Recent theoretical [134, 135] and experimental studies [139] of nanoplasmonic streaking without a microscope suggest lowering the stringent requirement for probing plasmonic fields in the instantaneous regime as it was demonstrated that a reconstruction of the fields is still attainable in the classical oscillatory regime.

The second achievement in this work is a successful development and implementation of a novel CEP-tagged ToF-PEEM instrument for studying CEP-dependent processes from metal surfaces. A combination of a single-shot ATI phase meter with the ToF-PEEM offers a real-time measurement of the CEP for every single laser shot as well as parallel data acquisition, which is advantageous for minimizing possible dynamic changes during the measurement. First CEP-resolved experiments were performed on gold NPOP and gold surface roughness samples using a 10 kHz few-cycle NIR laser source with pulse durations of 4 fs – 6.5 fs. We discovered an apparent CEP modulation with a period of π in these preliminary measurements, attributed to an artefact in CEP retrieval. Detailed investigation of this CEP artefact revealed that it is correlated to our laser intensity fluctuations, arising from an intensity-dependent energy shift of the photoelectrons emitted from the sample in conjunction with an intensity-dependent disbalance of the PAP. Further analysis by simulation confirmed the observed modulation depth amounting to a few percent and the π periodicity of this artefact. Note that the artefact can easily outweigh a weak CEP modulation of 1% – 3% in these measurements. Such artefact went unnoticed in the

phase tagging community since most CEP tagged-experiments were performed on gas targets in which the CEP effect was found to be much higher, from 4% to some tens of percent [164, 171, 231]. To remediate this issue, we added intensity tagging to the current CEP-tagged ToF-PEEM technique by introducing another channel to record the laser power for every laser shot. As a result, a 2π CEP modulation as small as $\sim 1\%$ from a bulk tungsten surface could be successfully retrieved well above the artefact background after also applying an appropriate intensity bias, proving the high sensitivity of the intensity-phase-tagging technique. However, a slight residual CEP artefact could not be entirely eliminated, which we attribute to a peak-intensity (or pulse duration) dependence while the current intensity-tagging technique only allows correcting for the average-intensity dependence. We expect that the residual artefact can be further suppressed by implementing peak-intensity tagging instead of average-intensity tagging, e.g. by using a nonlinear photodiode or another multiphoton process, such as second-harmonic generation, as a detector.

Our experimental results demonstrated the ability to perform and measure CEP control on photocurrent from a metal surface with energy resolution. To the best of our knowledge, we reported the first observation of a relatively high CEP modulation of up to $\sim 7\%$ from a metal surface in the strong space charge regime, as compared to a previous CEP-dependent measurement from a gold surface with less than 0.1% modulation depth [54, 198]. With increasing laser intensity, we observed a transition from multiphoton photoemission to the light-induced tunneling regime, indicated by an increase of the CEP modulation depth from $\sim 1\%$ to $\sim 7\%$. It is well-known that rescattered electrons in the tunneling regime are sensitive to the CEP of the laser pulses [12, 50]. We also found that the CEP-sensitive rescattered electrons were not significantly disturbed by the space charge, confirming previous predictions [40]. Theoretical models are crucial for further understanding of the role of space charge effects in the motion of rescattered electrons and are the subject of current research. Finally, we also explored the CEP dependence on supported gold nanotriangles but no CEP modulation was observed within a noise limit of $\sim 0.6\%$ in the measurements. A recent publication of similar work indicated a CEP modulation in the range of $0.005\% - 0.1\%$ for this type of structures [13]. In order to detect a very low CEP modulation, e.g. $\sim 0.1\%$, the most promising approach for improving the sensitivity of our system is using a high-repetition-rate few-cycle laser source [227–229], which would dramatically increase the electron count rate, hence improving the detection statistics, without introducing additional space charge. In parallel, we can improve the sample quality by using ultrasmooth single-crystalline gold nanostructures, as it was shown that a surface roughness of $2\text{ nm} - 3\text{ nm}$ is sufficient to smear out the CEP modulation [232]. These improvements will enable the observation of CEP control of photoemission from nanostructures with PEEM in the near future.

Bibliography

- [1] E. Muybridge. *Animals in Motion*. Dover Anatomy for Artists (Dover Publications, 1957).
- [2] P. J. Pupalaikis, B. Yamrone, R. Delbue, A. S. Khanna, K. Doshi, B. Bhat, and A. Sureka. *Technologies for very high bandwidth real-time oscilloscopes*. In [2014 IEEE Bipolar/BiCMOS Circuits and Technology Meeting \(BCTM\)](#), 128–135 (Sept. 2014).
- [3] R. Ell, U. Morgner, F. X. Kärtner, J. G. Fujimoto, E. P. Ippen, V. Scheuer, G. Angelow, T. Tschudi, M. J. Lederer, A. Boiko, and B. Luther-Davies. *Generation of 5-fs pulses and octave-spanning spectra directly from a Ti:sapphire laser*. [Optics Letters](#) **26**, 373–375 (2001).
- [4] M. Schultze, T. Binhammer, A. Steinmann, G. Palmer, M. Emons, and U. Morgner. *Few-cycle OPCPA system at 143 kHz with more than 1 μ J of pulse energy*. [Optics Express](#) **18**, 2836–2841 (2010).
- [5] E. Goulielmakis, M. Schultze, M. Hofstetter, V. S. Yakovlev, J. Gagnon, M. Uiberacker, A. L. Aquila, E. M. Gullikson, D. T. Attwood, R. Kienberger, F. Krausz, and U. Kleineberg. *Single-cycle nonlinear optics*. [Science](#) **320**, 1614–1617 (2008).
- [6] K. Zhao, Q. Zhang, M. Chini, Y. Wu, X. Wang, and Z. Chang. *Tailoring a 67 attosecond pulse through advantageous phase-mismatch*. [Optics Letters](#) **37**, 3891–3893 (2012).
- [7] A. H. Zewail. *Chemistry at the Uncertainty Limit*. [Angewandte Chemie International Edition](#) **40**, 4371–4375 (2001).
- [8] P. Baum and A. H. Zewail. *4D attosecond imaging with free electrons: diffraction methods and potential applications*. [Chemical Physics](#) **366**, 2–8 (2009).
- [9] H. Iglev, M. K. Fischer, A. Gliserin, and A. Laubereau. *Ultrafast geminate recombination after photodetachment of aqueous hydroxide*. [Journal of the American Chemical Society](#) **133**, 790–795 (2011).
- [10] A. Wirth, R. Santra, and E. Goulielmakis. *Real time tracing of valence-shell electronic coherences with attosecond transient absorption spectroscopy*. [Chemical Physics](#) **414**, 149–159 (2013).
- [11] A. Rosspeintner, B. Lang, and E. Vauthey. *Ultrafast photochemistry in liquids*. [Annual Review of Physical Chemistry](#) **64**, 247–271 (2013).

- [12] M. Krüger, M. Schenk, and P. Hommelhoff. *Attosecond control of electrons emitted from a nanoscale metal tip*. *Nature* **475**, 78–81 (2011).
- [13] W.P. Putnam, R.G. Hobbs, P.D. Keathley, K.K. Berggren, and F.X. Kärtner. *Optical-field-controlled photoemission from plasmonic nanoparticles*. *Nature Physics* **13**, 335–339 (2016).
- [14] M.F. Kling, C. Siedschlag, A.J. Verhoef, J.I. Khan, M. Schultze, T. Uphues, Y. Ni, M. Uiberacker, M. Drescher, F. Krausz, and M.J.J. Vrakking. *Control of electron localization in molecular dissociation*. *Science* **312**, 246–248 (2006).
- [15] M. Kübel, C. Burger, N.G. Kling, T. Pischke, L. Beaufore, I. Ben-Itzhak, G.G. Paulus, J. Ullrich, T. Pfeifer, R. Moshhammer, M.F. Kling, and B. Bergues. *Complete characterization of single-cycle double ionization of argon from the nonsequential to the sequential ionization regime*. *Physical Review A* **93**, 053422 (2016).
- [16] M. Drescher, M. Hentschel, R. Kienberger, M. Uiberacker, V. Yakovlev, A. Scrinzi, T. Westerwalbesloh, U. Kleineberg, U. Heinzmann, and F. Krausz. *Time-resolved atomic inner-shell spectroscopy*. *Nature* **419**, 803–807 (2002).
- [17] A.L. Cavalieri, N. Müller, T. Uphues, V.S. Yakovlev, A. Baltuška, B. Horvath, B. Schmidt, L. Blümel, R. Holzwarth, S. Hendel, M. Drescher, U. Kleineberg, P.M. Echenique, R. Kienberger, F. Krausz, et al. *Attosecond spectroscopy in condensed matter*. *Nature* **449**, 1029–1032 (2007).
- [18] M. Schultze, M. Fieß, N. Karpowicz, J. Gagnon, M. Korbman, M. Hofstetter, S. Neppl, A.L. Cavalieri, Y. Komninos, T. Mercouris, C.A. Nicolaides, R. Pazourek, S. Nagele, J. Feist, J. Burgdörfer, et al. *Delay in Photoemission*. *Science* **328**, 1658–1662 (2010).
- [19] M. Uiberacker, T. Uphues, M. Schultze, A.J. Verhoef, V. Yakovlev, M.F. Kling, J. Rauschenberger, N.M. Kabachnik, H. Schröder, M. Lezius, K.L. Kompa, H.-G. Muller, M.J.J. Vrakking, S. Hendel, U. Kleineberg, et al. *Attosecond real-time observation of electron tunnelling in atoms*. *Nature* **446**, 627–632 (2007).
- [20] M. Wagner, Z. Fei, A.S. McLeod, A.S. Rodin, W. Bao, E.G. Iwinski, Z. Zhao, M. Goldflam, M. Liu, G. Dominguez, M. Thiemens, M.M. Fogler, A.H. Castro Neto, C.N. Lau, S. Amarie, et al. *Ultrafast and nanoscale plasmonic phenomena in exfoliated graphene revealed by infrared pump-probe nanoscopy*. *Nano Letters* **14**, 894–900 (2014).
- [21] D.J. Flannigan and A.H. Zewail. *4D electron microscopy: principles and applications*. *Accounts of Chemical Research* **45**, 1828–1839 (2012).
- [22] C. Rischel, A. Rousse, I. Uschmann, P.-A. Albouy, J.-P. Geindre, P. Audebert, J.-C. Gauthier, E. Fröster, J.-L. Martin, and A. Antonetti. *Femtosecond time-resolved X-ray diffraction from laser-heated organic films*. *Nature* **390**, 490–492 (1997).
- [23] M. Levantino, B.A. Yorke, D.C. Monteiro, M. Cammarata, and A.R. Pearson. *Using synchrotrons and XFELs for time-resolved X-ray crystallography and solution scattering experiments on biomolecules*. *Current Opinion in Structural Biology* **35**, 41–48 (2015).

- [24] G. Sciaini and R. J. D. Miller. *Femtosecond electron diffraction: heralding the era of atomically resolved dynamics*. *Reports on Progress in Physics* **74**, 096101 (2011).
- [25] A. Gliserin, M. Walbran, F. Krausz, and P. Baum. *Sub-phonon-period compression of electron pulses for atomic diffraction*. *Nature Communications* **6**, 8723 (2015).
- [26] A. Takaoka, K. Ura, H. Mori, T. Katsuta, I. Matsui, and S. Hayashi. *Development of a new 3 MV ultra-high voltage electron microscope at Osaka University*. *Journal of Electron Microscopy* **46**, 447–456 (1997).
- [27] A. H. Zewail. *Four-dimensional electron microscopy*. *Science* **328**, 187–193 (2010).
- [28] O. Schmidt, M. Bauer, C. Wiemann, R. Porath, M. Scharfe, O. Andreyev, G. Schönhense, and M. Aeschlimann. *Time-resolved two photon photoemission electron microscopy*. *Applied Physics B* **74**, 223–227 (2002).
- [29] A. Kubo, K. Onda, H. Petek, Z. Sun, Y. S. Jung, and H. K. Kim. *Femtosecond imaging of surface plasmon dynamics in a nanostructured silver film*. *Nano Letters* **5**, 1123–1127 (2005).
- [30] M. Aeschlimann, M. Bauer, D. Bayer, T. Brixner, S. Cunovic, F. Dimler, A. Fischer, W. Pfeiffer, M. Rohmer, C. Schneider, F. Steeb, C. Stüber, and D. V. Voronine. *Spatiotemporal control of nanooptical excitations*. *Proceedings of the National Academy of Sciences* **107**, 5329–5333 (2010).
- [31] J. Lin, N. Weber, A. Wirth, S. H. Chew, M. Escher, M. Merkel, M. F. Kling, M. I. Stockman, F. Krausz, and U. Kleineberg. *Time of flight-photoemission electron microscope for ultrahigh spatiotemporal probing of nanoplasmonic optical fields*. *Journal of Physics: Condensed Matter* **21**, 314005 (2009).
- [32] G. Spektor, D. Kilbane, A. K. Mahro, B. Frank, S. Ristok, L. Gal, P. Kahl, D. Podbiel, S. Mathias, H. Giessen, F.-J. Meyer zu Heringdorf, M. Orenstein, and M. Aeschlimann. *Revealing the subfemtosecond dynamics of orbital angular momentum in nanoplasmonic vortices*. *Science* **355**, 1187–1191 (2017).
- [33] M. zu Heringdorf F.-J., N. M. Buckanie, L. I. Chelaru, and N. Raß. In *Imaging of Surface Plasmon Waves in Nonlinear Photoemission Microscopy. EMC 2008 14th European Microscopy Congress 1–5 September 2008, Aachen, Germany: Volume 1: Instrumentation and Methods*, pp. 737–738. Edited by M. Luysberg, K. Tillmann, and T. Weirich (Springer Berlin Heidelberg, Berlin, Heidelberg, 2008).
- [34] S. H. Chew, F. Süßmann, C. Späth, A. Wirth, J. Schmidt, S. Zherebtsov, A. Guggenmos, A. Oelsner, N. Weber, J. Kapaldo, A. Gliserin, M. I. Stockman, M. F. Kling, and U. Kleineberg. *Time-of-flight-photoelectron emission microscopy on plasmonic structures using attosecond extreme ultraviolet pulses*. *Applied Physics Letters* **100**, 051904 (2012).
- [35] A. Mikkelsen, J. Schwenke, T. Fordell, G. Luo, K. Klünder, E. Hilner, N. Anttu, A. A. Zakharov, E. Lundgren, J. Mauritsson, J. N. Andersen, H. Q. Xu, and A. L’Huillier. *Photoemission electron microscopy using extreme ultraviolet attosecond pulse trains*. *Review of Scientific Instruments* **80**, 123703 (2009).

- [36] E. Mårzell, C.L. Arnold, E. Lorek, D. Guenot, T. Fordell, M. Miranda, J. Mauritsson, H. Xu, A. L’Huillier, and A. Mikkelsen. *Secondary electron imaging of nanostructures using Extreme Ultra-Violet attosecond pulse trains and Infra-Red femtosecond pulses*. *Annalen der Physik* **525**, 162–170 (2013).
- [37] A. Schiffrin, T. Paasch-Colberg, N. Karpowicz, V. Apalkov, D. Gerster, S. Muhlbrandt, M. Korbman, J. Reichert, M. Schultze, S. Holzner, J.V. Barth, R. Kienberger, R. Ernstorfer, V.S. Yakovlev, M.I. Stockman, et al. *Optical-field-induced current in dielectrics*. *Nature* **493**, 70–74 (2013).
- [38] R. Kienberger, E. Goulielmakis, M. Uiberacker, A. Baltuska, V. Yakovlev, F. Bammer, A. Scrinzi, T. Westerwalbesloh, U. Kleineberg, U. Heinzmann, M. Drescher, and F. Krausz. *Atomic transient recorder*. *Nature* **427**, 817–821 (2004).
- [39] P.B. Corkum and F. Krausz. *Attosecond science*. *Nature Physics* **3**, 381–387 (2007).
- [40] B. Piglosiewicz, S. Schmidt, D.J. Park, J. Vogelsang, P. Grosz, C. Manzoni, P. Farinello, G. Cerullo, and C. Lienau. *Carrier-envelope phase effects on the strong-field photoemission of electrons from metallic nanostructures*. *Nature Photonics* **8**, 37–42 (2014).
- [41] L. E. Hargrove, R. L. Fork, and M. A. Pollack. *Locking of He-Ne laser modes induced by synchronous intracavity modulation*. *Applied Physics Letters* **5**, 4–5 (1964).
- [42] J. Li, X. Ren, Y. Yin, K. Zhao, A. Chew, Y. Cheng, E. Cunningham, Y. Wang, S. Hu, Y. Wu, M. Chini, and Z. Chang. *53-attosecond X-ray pulses reach the carbon K-edge*. *Nature Communications* **8**, 186 (2017).
- [43] G. Herink, D.R. Solli, M. Gulde, and C. Ropers. *Field-driven photoemission from nanostructures quenches the quiver motion*. *Nature* **483**, 190–193 (2012).
- [44] P. Dombi, A. Hörl, P. Rácz, I. Márton, A. Trügler, J.R. Krenn, and U. Hohenester. *Ultrafast strong-field photoemission from plasmonic nanoparticles*. *Nano Letters* **13**, 674–678 (2013).
- [45] W. Putnam, R. Hobbs, Y. Yang, K.K. Berggren, and F. Kärtner. *Carrier-envelope phase sensitive strong-field photoemission from plasmonic nanoparticles*. In *CLEO: 2014*, FTu1D.5 (2014).
- [46] M. Fieß, M. Schultze, E. Goulielmakis, B. Dennhardt, J. Gagnon, M. Hofstetter, R. Kienberger, and F. Krausz. *Versatile apparatus for attosecond metrology and spectroscopy*. *Review of Scientific Instruments* **81**, 093103 (2010).
- [47] E. Magerl, S. Neppl, A.L. Cavalieri, E.M. Bothschafter, M. Stanislowski, T. Uphues, M. Hofstetter, U. Kleineberg, J.V. Barth, D. Menzel, F. Krausz, R. Ernstorfer, R. Kienberger, and P. Feulner. *A flexible apparatus for attosecond photoelectron spectroscopy of solids and surfaces*. *Review of Scientific Instruments* **82**, 063104 (2011).
- [48] S. Rausch, T. Binhammer, A. Harth, E. Schulz, M. Siegel, and U. Morgner. *Few-cycle oscillator pulse train with constant carrier-envelope-phase and 65 as jitter*. *Optics Express* **17**, 20282–20290 (2009).

- [49] S. Prinz, M. Haefner, C. Y. Teisset, R. Bessing, K. Michel, Y. Lee, X. T. Geng, S. Kim, D. E. Kim, T. Metzger, and M. Schultze. *CEP-stable, sub-6 fs, 300-kHz OPCPA system with more than 15 W of average power*. *Optics Express* **23**, 1388–1394 (2015).
- [50] G. G. Paulus, F. Grasbon, H. Walther, P. Villoresi, M. Nisoli, S. Stagira, E. Priori, and S. De Silvestri. *Absolute-phase phenomena in photoionization with few-cycle laser pulses*. *Nature* **414**, 182–184 (2001).
- [51] A. Baltuška, T. Udem, M. Uiberacker, M. Hentschel, E. Goulielmakis, C. Gohle, R. Holzwarth, V. S. Yakovlev, A. Scrinzi, T. W. Hänsch, and F. Krausz. *Attosecond control of electronic processes by intense light fields*. *Nature* **421**, 611–615 (2003).
- [52] A. Borot, A. Malvache, X. Chen, A. Jullien, J.-P. Geindre, P. Audebert, G. Mourou, F. Quéré, and R. Lopez-Martens. *Attosecond control of collective electron motion in plasmas*. *Nature Physics* **8**, 416 (2012).
- [53] L. Xu, T. W. Hänsch, C. Spielmann, A. Poppe, T. Brabec, and F. Krausz. *Route to phase control of ultrashort light pulses*. *Optics Letters* **21**, 2008–2010 (1996).
- [54] P. Dombi, A. Apolonski, C. Lemell, G. G. Paulus, M. Kakehata, R. Holzwarth, T. Udem, K. Torizuka, J. Burgdörfer, T. W. Hänsch, and F. Krausz. *Direct measurement and analysis of the carrier-envelope phase in light pulses approaching the single-cycle regime*. *New Journal of Physics* **6**, 39 (2004).
- [55] F. W. Helbing, G. Steinmeyer, U. Keller, R. S. Windeler, J. Stenger, and H. R. Telle. *Carrier-envelope offset dynamics of mode-locked lasers*. *Optics Letters* **27**, 194–196 (2002).
- [56] Y. S. Lee, J. H. Sung, C. H. Nam, T. J. Yu, and K.-H. Hong. *Novel method for carrier-envelope-phase stabilization of femtosecond laser pulses*. *Optics Express* **13**, 2969–2976 (2005).
- [57] T. J. Yu, K.-H. Hong, H.-G. Choi, J. H. Sung, I. W. Choi, D.-K. Ko, J. Lee, J. Kim, D. E. Kim, and C. H. Nam. *Precise and long-term stabilization of the carrier-envelope phase of femtosecond laser pulses using an enhanced direct locking technique*. *Optics Express* **15**, 8203–8211 (2007).
- [58] F. Lücking, A. Assion, A. Apolonski, F. Krausz, and G. Steinmeyer. *Long-term carrier-envelope-phase-stable few-cycle pulses by use of the feed-forward method*. *Optics Letters* **37**, 2076–2078 (2012).
- [59] Y. Fu, E. J. Takahashi, and K. Midorikawa. *Indirect high-bandwidth stabilization of carrier-envelope phase of a high-energy, low-repetition-rate laser*. *Optics Express* **24**, 13276–13287 (2016).
- [60] R. Szipöcs, K. Ferencz, C. Spielmann, and F. Krausz. *Chirped multilayer coatings for broadband dispersion control in femtosecond lasers*. *Optics Letters* **19**, 201–203 (1994).
- [61] P. Tournois. *Acousto-optic programmable dispersive filter for adaptive compensation of group delay time dispersion in laser systems*. *Optics Communications* **140**, 245–249 (1997).

- [62] A. McPherson, G. Gibson, H. Jara, U. Johann, T. S. Luk, I. A. McIntyre, K. Boyer, and C. K. Rhodes. *Studies of multiphoton production of vacuum-ultraviolet radiation in the rare gases*. *Journal of Physics B: Atomic, Molecular and Optical Physics* **4**, 595–601 (1987).
- [63] M. Ferray, A. L’Huillier, X. F. Li, L. A. Lompre, G. Mainfray, and C. Manus. *Multiple-harmonic conversion of 1064 nm radiation in rare gases*. *Journal of Physics B: Atomic, Molecular and Optical Physics* **21**, L31 (1988).
- [64] P. B. Corkum. *Plasma perspective on strong field multiphoton ionization*. *Physical Review Letters* **71**, 1994–1997 (1993).
- [65] J. L. Krause, K. J. Schafer, and K. C. Kulander. *High-order harmonic generation from atoms and ions in the high intensity regime*. *Physical Review Letters* **68**, 3535–3538 (1992).
- [66] L.-N. Li and F. He. *Ionization and high harmonic generation of two-dimensional quasiperiodic structures in arbitrarily polarized strong laser fields*. *Journal of the Optical Society of America B* **34**, 2707–2714 (2017).
- [67] M. Lewenstein, P. Balcou, M. Y. Ivanov, A. L’Huillier, and P. B. Corkum. *Theory of high-harmonic generation by low-frequency laser fields*. *Physical Review A* **49**, 2117–2132 (1994).
- [68] F. Krausz and M. Ivanov. *Attosecond physics*. *Review Modern Physics* **81**, 163–234 (2009).
- [69] A. Rundquist, C. G. Durfee, Z. Chang, C. Herne, S. Backus, M. M. Murnane, and H. C. Kapteyn. *Phase-matched generation of coherent soft X-rays*. *Science* **280**, 1412–1415 (1998).
- [70] E. Constant, D. Garzella, P. Breger, E. Mével, C. Dorrer, C. Le Blanc, F. Salin, and P. Agostini. *Optimizing high harmonic generation in absorbing gases: model and experiment*. *Physical Review Letters* **82**, 1668–1671 (1999).
- [71] A. Wirth. *Attosecond transient absorption spectroscopy*. PhD thesis, Ludwig Maximilian University of Munich (2011).
- [72] D. Attwood. *Soft X-Rays and Extreme Ultraviolet Radiation: Principles and Applications* (Cambridge University Press, New York, NY, USA, 2007).
- [73] M. Schnürer, Z. Cheng, M. Hentschel, F. Krausz, T. Wilhein, D. Hambach, G. Schmahl, M. Drescher, Y. Lim, and U. Heinzmann. *Few-cycle-driven XUV laser harmonics: generation and focusing*. *Applied Physics B* **70**, S227–S232 (2000).
- [74] T. Brabec and F. Krausz. *Intense few-cycle laser fields: frontiers of nonlinear optics*. *Review of Modern Physics* **72**, 545–591 (2000).
- [75] M. Schultze, E. Goulielmakis, M. Uiberacker, M. Hofstetter, J. Kim, D. Kim, F. Krausz, and U. Kleineberg. *Powerful 170-attosecond XUV pulses generated with few-cycle laser pulses and broadband multilayer optics*. *New Journal of Physics* **9**, 243 (2007).
- [76] E. M. Bothschafter, A. Schiffrin, V. Yakovlev, A. Azzeer, F. Krausz, R. Ernstorfer, and R. Kienberger. *Collinear generation of ultrashort UV and XUV pulses*. *Optics Express* **18**, 9173–9180 (2010).

- [77] K. Varjú, P. Johnsson, R. López, T. Remetter, E. Gustafsson, J. Mauritsson, M. Gaarde, K. Schafer, C. Erny, I. Sola, A. Zair, E. Constant, E. Cormier, E. Mevel, and A. L’Huillier. *Experimental studies of attosecond pulse trains*. *Laser Physics* **15**, 888–898 (2005).
- [78] M. Chini, K. Zhao, and Z. Chang. *The generation, characterization and applications of broadband isolated attosecond pulses*. *Nature Photonics* **8**, 178–186 (2014).
- [79] G. Sansone, E. Benedetti, F. Calegari, C. Vozzi, L. Avaldi, R. Flammini, L. Poletto, P. Villoresi, C. Altucci, R. Velotta, S. Stagira, S. De Silvestri, and M. Nisoli. *Isolated single-cycle attosecond pulses*. *Science* **314**, 443–446 (2006).
- [80] C. Altucci, J. Tisch, and R. Velotta. *Single attosecond light pulses from multi-cycle laser sources*. *Journal of Modern Optics* **58**, 1585–1610 (2011).
- [81] H. Mashiko, S. Gilbertson, C. Li, S. D. Khan, M. M. Shakya, E. Moon, and Z. Chang. *Double optical gating of high-order harmonic generation with carrier-envelope phase stabilized lasers*. *Physical Review Letters* **100**, 103906 (2008).
- [82] H. Hertz. *Ueber einen Einfluss des ultravioletten Lichtes auf die elektrische Entladung*. *Annalen der Physik* **267**, 983–1000 (1887).
- [83] A. Einstein. *Über einen die Erzeugung und Verwandlung des Lichtes betreffenden heuristischen Gesichtspunkt*. *Annalen der Physik* **322**, 132–148 (1905).
- [84] A. Kahn. *Fermi level, work function and vacuum level*. *Materials Horizons* **3**, 7–10 (2016).
- [85] B. F. B. Feuerbacher and R. F. Willis. *Photoemission and the electronic properties of surfaces*. *Journal of The Electrochemical Society* **126**, 393C (1979).
- [86] T.-C. Chiang and F. Seitz. *Photoemission spectroscopy in solids*. *Annalen der Physik* **10**, 61–74 (2001).
- [87] S. Hüfner. *Photoelectron Spectroscopy: Principles and Applications*. 3rd ed. (Springer-Verlag Berlin Heidelberg, 2003).
- [88] C. N. Berglund and W. E. Spicer. *Photoemission studies of copper and silver: theory*. *Physical Review* **136**, A1030–A1044 (1964).
- [89] C. N. Berglund and W. E. Spicer. *Photoemission studies of copper and silver: experiment*. *Physical Review* **136**, A1044–A1064 (1964).
- [90] D. W. Lynch and C. G. Olson. *Photoemission Studies of High-Temperature Superconductors* (Cambridge University Press, 2005).
- [91] A. Chtchelkanova, S. Wolf, and Y. Idzerda, eds. *Magnetic Interactions and Spin Transport* (Springer US, 2003).
- [92] M. Aeschlimann, C. A. Schmuttenmaer, H. E. Elsayed-Ali, R. J. D. Miller, J. Cao, Y. Gao, and D. A. Mantell. *Observation of surface enhanced multiphoton photoemission from metal surfaces in the short pulse limit*. *The Journal of Chemical Physics* **102**, 8606 (1995).
- [93] M. I. Stockman and P. Hewageegana. *Nanolocalized nonlinear electron photoemission under coherent control*. *Nano Letters* **5**, 2325–2329 (2005).

- [94] L. Keldysh. *Ionization in the field of a strong electromagnetic wave*. Journal of Experimental and Theoretical Physics **20**, 1307 (1965).
- [95] F. Bunkin and M. Fedorov. *Cold emission of electrons from the surface of a metal in a strong radiation field*. Journal of Experimental and Theoretical Physics **21**, 896 (1965).
- [96] H. Ueba and B. Gumhalter. *Theory of two-photon photoemission spectroscopy of surfaces*. Progress in Surface Science **82**, 193–223 (2007).
- [97] S. Luan, R. Hippler, H. Schwier, and H. O. Lutz. *Electron emission from polycrystalline copper surfaces by multi-photon absorption*. Europhysics Letters **9**, 489 (1989).
- [98] W. S. Fann, R. Storz, and J. Bokor. *Observation of above-threshold multiphoton photoelectric emission from image-potential surface states*. Physical Review B **44**, 10980–10982 (1991).
- [99] G. Farkas, C. Toth, and A. Kohazi-Kis. *Above-threshold multiphoton photoelectric effect of a gold surface*. Optical Engineering **32**, 2476–2480 (1993).
- [100] F. Banfi, C. Giannetti, G. Ferrini, G. Galimberti, S. Pagliara, D. Fausti, and F. Parmigiani. *Experimental evidence of above-threshold photoemission in solids*. Physical Review Letters **94**, 037601 (2005).
- [101] F. Bisio, M. Nývlt, J. Franta, H. Petek, and J. Kirschner. *Mechanisms of high-order perturbative photoemission from Cu(001)*. Physical Review Letters **96**, 087601 (2006).
- [102] J. Eberly, J. Javanainen, and K. Rzażewski. *Above-threshold ionization*. Physics Reports **204**, 331–383 (1991).
- [103] G. G. Paulus, W. Nicklich, H. Xu, P. Lambropoulos, and H. Walther. *Plateau in above threshold ionization spectra*. Physical Review Letters **72**, 2851–2854 (1994).
- [104] M. Schenk, M. Krüger, and P. Hommelhoff. *Strong-field above-threshold photoemission from sharp metal tips*. Physical Review Letters **105**, 257601 (2010).
- [105] C. Kern, M. Zürich, J. Petschulat, T. Pertsch, B. Kley, T. Käsebier, U. Hübner, and C. Spielmann. *Comparison of femtosecond laser-induced damage on unstructured vs. nano-structured Au-targets*. Applied Physics A **104**, 15 (2011).
- [106] B. Wang and L. Gallais. *A theoretical investigation of the laser damage threshold of metal multi-dielectric mirrors for high power ultrashort applications*. Optics Express **21**, 14698–14711 (2013).
- [107] F. Schertz, M. Schmelzeisen, M. Kreiter, H.-J. Elmers, and G. Schönhense. *Field emission of electrons generated by the near field of strongly coupled plasmons*. Physical Review Letters **108**, 237602 (2012).
- [108] A. Bartoli, G. Ferrini, L. Fini, G. Gabetta, F. Parmigiani, and F. T. Arecchi. *Non-linear photoemission from W and Cu investigated by total-yield correlation measurements*. Physical Review B **56**, 1107–1110 (1997).
- [109] C. Kealhofer, S. M. Foreman, S. Gerlich, and M. A. Kasevich. *Ultrafast laser-triggered emission from hafnium carbide tips*. Physical Review B **86**, 035405 (2012).

- [110] V. V. Temnov. *Ultrafast acousto-magneto-plasmonics*. *Nature Photonics* **6**, 728–736 (2012).
- [111] S. A. Maier. *Plasmonics: Fundamentals and Applications*. 1st ed. (Springer US, 2007).
- [112] Y. Fang and M. Sun. *Nanoplasmonic waveguides: towards applications in integrated nanophotonic circuits*. *Light: Science and Applications* **4**, e294 (2015).
- [113] C. F. Bohren and D. R. Huffman. *Absorption and Scattering of Light by Small Particles* (Wiley-VCH, 1998).
- [114] G. Mie. *Beiträge zur Optik trüber Medien, speziell kolloidaler Metallösungen*. *Annalen der Physik* **330**, 377–445 (1908).
- [115] S. Link and M. A. El-Sayed. *Spectral properties and relaxation dynamics of surface plasmon electronic oscillations in gold and silver nanodots and nanorods*. *The Journal of Physical Chemistry B* **103**, 8410–8426 (1999).
- [116] E. Boulais, R. Lachaine, A. Hatef, and M. Meunier. *Plasmonics for pulsed-laser cell nanosurgery: fundamentals and applications*. *Journal of Photochemistry and Photobiology C: Photochemistry Reviews* **17**, 26–49 (2013).
- [117] M. I. Stockman, M. F. Kling, U. Kleineberg, and F. Krausz. *Attosecond nanoplasmonic field microscope*. *Nature Photonics* **1**, 539–544 (2007).
- [118] E. G. Gamaly. *Femtosecond Laser-Matter Interaction: Theory, Experiments and Applications* (Pan Stanford, 2011).
- [119] J. Dorfmüller, R. Vogelgesang, R. T. Weitz, C. Rockstuhl, C. Etrich, T. Pertsch, F. Lederer, and K. Kern. *Fabry-Pérot resonances in one-dimensional plasmonic nanostructures*. *Nano Letters* **9**, 2372–2377 (2009).
- [120] M. Liu, T.-W. Lee, S. K. Gray, P. Guyot-Sionnest, and M. Pelton. *Excitation of dark plasmons in metal nanoparticles by a localized emitter*. *Physical Review Letters* **102**, 107401 (2009).
- [121] R. Guo, E. C. Kinzel, Y. Li, S. M. Uppuluri, A. Raman, and X. Xu. *Three-dimensional mapping of optical near field of a nanoscale bowtie antenna*. *Optics Express* **18**, 4961–4971 (2010).
- [122] P. Alonso-González, P. Albella, F. Golmar, L. Arzubiaga, F. Casanova, L. E. Hueso, J. Aizpurua, and R. Hillenbrand. *Visualizing the near-field coupling and interference of bonding and anti-bonding modes in infrared dimer nanoantennas*. *Optics Express* **21**, 1270–1280 (2013).
- [123] H. Cohen, T. Maniv, R. Tenne, Y. R. Hacoheh, O. Stephan, and C. Colliex. *Near-field electron energy loss spectroscopy of nanoparticles*. *Physical Review Letters* **80**, 782–785 (1998).
- [124] O. Nicoletti, F. de la Pena, R. K. Leary, D. J. Holland, C. Ducati, and P. A. Midgley. *Three-dimensional imaging of localized surface plasmon resonances of metal nanoparticles*. *Nature* **502**, 80–84 (2013).
- [125] B. Barwick, D. J. Flannigan, and A. H. Zewail. *Photon-induced near-field electron microscopy*. *Nature* **462**, 902–906 (2009).

- [126] S. T. Park, M. Lin, and A. H. Zewail. *Photon-induced near-field electron microscopy (PINEM): theoretical and experimental*. *New Journal of Physics* **12**, 123028 (2010).
- [127] F. Schertz, M. Schmelzeisen, R. Mohammadi, M. Kreiter, H.-J. Elmers, and G. Schönhense. *Near field of strongly coupled plasmons: uncovering dark modes*. *Nano Letters* **12**, 1885–1890 (2012).
- [128] H. Yu, Q. Sun, K. Ueno, T. Oshikiri, A. Kubo, Y. Matsuo, and H. Misawa. *Exploring coupled plasmonic nanostructures in the near field by photoemission electron microscopy*. *ACS Nano* **10**, 10373–10381 (2016).
- [129] F.-J. M. zu Heringdorf, L. Chelaru, S. Möllenbeck, D. Thien, and M. H.-v. Hoegen. *Femtosecond photoemission microscopy*. *Surface Science* **601**, 4700–4705 (2007).
- [130] D. Bayer, C. Wiemann, O. Gaier, M. Bauer, and M. Aeschlimann. *Time-resolved 2PPE and time-resolved PEEM as a probe of LSP's in silver nanoparticles*. *Journal of Nanomaterials* **2008**, 11 (2008).
- [131] M. Stockman and P. Hewageegana. *Absolute phase effect in ultrafast optical responses of metal nanostructures*. *Applied Physics A* **89**, 247–250 (2007).
- [132] E. Goulielmakis, M. Uiberacker, R. Kienberger, A. Baltuska, V. Yakovlev, A. Scrinzi, T. Westerwalbesloh, U. Kleineberg, U. Heinzmann, M. Drescher, and F. Krausz. *Direct measurement of light waves*. *Science* **305**, 1267–1269 (2004).
- [133] E. Mårzell. *Photoemission Electron Microscopy for Ultrafast Nano-Optics – Femtoseconds to Attoseconds*. PhD thesis, Lund University (2015).
- [134] E. Skopalová, D. Y. Lei, T. Witting, C. Arrell, F. Frank, Y. Sonnefraud, S. A. Maier, J. W. G. Tisch, and J. P. Marangos. *Numerical simulation of attosecond nanoplasmonic streaking*. *New Journal of Physics* **13**, 083003 (2011).
- [135] F. Süßmann and M. F. Kling. *Attosecond nanoplasmonic streaking of localized fields near metal nanospheres*. *Physical Review B* **84**, 121406 (2011).
- [136] F. Kelkensberg, A. F. Koenderink, and M. J. J. Vrakking. *Attosecond streaking in a nano-plasmonic field*. *New Journal of Physics* **14**, 093034 (2012).
- [137] J. Li, E. Saydanzad, and U. Thumm. *Retrieving plasmonic near-field information: a quantum-mechanical model for streaking photoelectron spectroscopy of gold nanospheres*. *Physical Review A* **94**, 051401 (2016).
- [138] S. H. Chew, K. Pearce, C. Späth, A. Guggenmos, J. Schmidt, F. Süßmann, M. F. Kling, U. Kleineberg, E. Mårzell, C. L. Arnold, E. Lorek, P. Rudawski, C. Guo, M. Miranda, F. Ardana, et al. In *Imaging Localized Surface Plasmons by Femtosecond to Attosecond Time-Resolved Photoelectron Emission Microscopy—“ATTO-PEEM”*. *Attosecond Nanophysics*, pp. 325–364 (Wiley-VCH Verlag GmbH & Co. KGaA, 2015).
- [139] B. Förg, J. Schötz, F. Süßmann, M. Förster, M. Krüger, B. Ahn, W. A. Okell, K. Wintersperger, S. Zherebtsov, A. Guggenmos, V. Pervak, A. Kessel, S. A. Trushin, A. M. Azzeer, M. I. Stockman, et al. *Attosecond nanoscale near-field sampling*. *Nature Communications* **7**, 11717 (2016).

- [140] E. Brüche. *Elektronenmikroskopische Abbildung mit lichtelektrischen Elektronen*. Zeitschrift für Physik **86**, 448–450 (1933).
- [141] A. Oelsner, O. Schmidt, M. Schicketanz, M. Klais, G. Schönhense, V. Mergel, O. Jagutzki, and H. Schmidt-Böcking. *Microspectroscopy and imaging using a delay line detector in time-of-flight photoemission microscopy*. *Review of Scientific Instruments* **72**, 3968–3974 (2001).
- [142] G. Schönhense, A. Oelsner, O. Schmidt, G. Fecher, V. Mergel, O. Jagutzki, and H. Schmidt-Böcking. *Time-of-flight photoemission electron microscopy – a new way to chemical surface analysis*. *Surface Science* **480**, 180–187 (2001).
- [143] N. B. Weber, M. Escher, M. Merkel, A. Oelsner, and G. Schönhense. *Energy- and time-resolved microscopy using PEEM: recent developments and state-of-the-art*. *Journal of Physics: Conference Series* **100**, 072031 (2008).
- [144] A. Oelsner, M. Rohmer, C. Schneider, D. Bayer, G. Schönhense, and M. Aeschlimann. *Time- and energy resolved photoemission electron microscopy-imaging of photoelectron time-of-flight analysis by means of pulsed excitations*. *Journal of Electron Spectroscopy and Related Phenomena* **178 – 179**, 317–330 (2010).
- [145] *Instruction Manual: ToF-Option for PEEM*. Omicron NanoTechnology GmbH / FOCUS GmbH. (2012).
- [146] C. Schneider. *Zeit- und energieaufgelöste Time-of-Flight-PEEM-Messungen an strukturierten Oberflächen*. Master’s thesis, Kaiserslautern University of Technology (2008).
- [147] A. Gliserin. *Towards attosecond 4D imaging of atomic-scale dynamics by single-electron diffraction*. PhD thesis, Ludwig Maximilian University of Munich (2014).
- [148] A. Gliserin, M. Walbran, and P. Baum. *A high-resolution time-of-flight energy analyzer for femtosecond electron pulses at 30 keV*. *Review of Scientific Instruments* **87**, 033302 (2016).
- [149] W. Steinmann and T. Fauster. In *Two-Photon Photoelectron Spectroscopy of Electronics States at Metal Surfaces*. Advanced Series in Physical Chemistry: Vol. 5. *Laser Spectroscopy and Photochemistry on Metal Surfaces*, pp. 184–242. Edited by H.-L. Dai and W. Ho (World Scientific, Singapore, 1995).
- [150] C. P. Poole. *The Physics Handbook: Fundamentals and Key Equations* (New York: John Wiley, 1998).
- [151] J. Kröger, T. Greber, T. Kreutz, and J. Osterwalder. *The photoemission Fermi edge as a sample thermometer?* *Journal of Electron Spectroscopy and Related Phenomena* **113**, 241–251 (2001).
- [152] Z. Major, S. A. Trushin, I. Ahmad, M. Siebold, C. Wandt, S. Klingebiel, T.-J. Wang, J. A. Fülöp, A. Henig, S. Kruber, R. Weingartner, A. Popp, J. Osterhoff, R. Hörlein, J. Hein, et al. *Basic concepts and current status of the Petawatt Field Synthesizer – a new approach to ultrahigh field generation*. *The Review of Laser Engineering* **37**, 431–436 (2009).

- [153] C. Wandt, S. Klingebiel, S. Keppler, M. Hornung, M. Loeser, M. Siebold, C. Skrobol, A. Kessel, S. A. Trushin, Z. Major, J. Hein, M. C. Kaluza, F. Krausz, and S. Karsch. *Development of a Joule-class Yb:YAG amplifier and its implementation in a CPA system generating 1 TW pulses*. *Laser and Photonics Reviews* **8**, 875–881 (2014).
- [154] F. Süßmann. *Attosecond dynamics of nano-localized fields probed by photoelectron spectroscopy*. PhD thesis, Ludwig Maximilian University of Munich (2013).
- [155] I. Ahmad, S. A. Trushin, Z. Major, C. Wandt, S. Klingebiel, T.-J. Wang, V. Pervak, A. Popp, M. Siebold, F. Krausz, and S. Karsch. *Frontend light source for short-pulse pumped OPCPA system*. *Applied Physics B* **97**, 529–536 (2009).
- [156] M. Nisoli, S. De Silvestri, and O. Svelto. *Generation of high energy 10 fs pulses by a new pulse compression technique*. *Applied Physics Letters* **68**, 2793–2795 (1996).
- [157] M. Nisoli, S. de Silvestri, O. Svelto, R. Szipöcs, K. Ferencz, C. Spielmann, S. Sartania, and F. Krausz. *Compression of high-energy laser pulses below 5 fs*. *Optics Letters* **22**, 522–524 (1997).
- [158] T. Brabec. *Strong Field Laser Physics*. Vol. 134. Springer Series in Optical Sciences (Springer, 2008).
- [159] M. Schnürer, Z. Cheng, M. Hentschel, G. Tempea, P. Kálmán, T. Brabec, and F. Krausz. *Absorption-limited generation of coherent ultrashort soft-X-ray pulses*. *Physical Review Letters* **83**, 722–725 (1999).
- [160] R. Holzwarth, T. Udem, T. W. Hänsch, J. C. Knight, W. J. Wadsworth, and P. S. J. Russell. *Optical frequency synthesizer for precision spectroscopy*. *Physics Review Letters* **85**, 2264–2267 (2000).
- [161] D. J. Jones, S. A. Diddams, J. K. Ranka, A. Stentz, R. S. Windeler, J. L. Hall, and S. T. Cundiff. *Carrier-envelope phase control of femtosecond mode-locked lasers and direct optical frequency synthesis*. *Science* **288**, 635–639 (2000).
- [162] C. Li, E. Moon, H. Wang, H. Mashiko, C. M. Nakamura, J. Tackett, and Z. Chang. *Determining the phase-energy coupling coefficient in carrier-envelope phase measurements*. *Optics Letters* **32**, 796–798 (2007).
- [163] S. Koke, C. Grebing, H. Frei, A. Anderson, A. Assion, and G. Steinmeyer. *Direct frequency comb synthesis with arbitrary offset and shot-noise-limited phase noise*. *Nature Photonics* **4**, 462–465 (2010).
- [164] N. G. Johnson, O. Herrwerth, A. Wirth, S. De, I. Ben-Itzhak, M. Lezius, B. Bergues, M. F. Kling, A. Senfleben, C. D. Schröter, R. Moshhammer, J. Ullrich, K. J. Betsch, R. R. Jones, A. M. Saylor, et al. *Single-shot carrier-envelope-phase-tagged ion-momentum imaging of nonsequential double ionization of argon in intense 4-fs laser fields*. *Physical Review A* **83**, 013412 (2011).
- [165] X. Liu, H. Rottke, E. Eremina, W. Sandner, E. Goulielmakis, K. O. Keeffe, M. Lezius, F. Krausz, F. Lindner, M. G. Schätzel, G. G. Paulus, and H. Walther. *Non-sequential double ionization at the single-optical-cycle limit*. *Physical Review Letters* **93**, 263001 (2004).

- [166] T. Wittmann, B. Horvath, W. Helml, M. G. Schätzel, X. Gu, A. L. Cavalieri, G. G. Paulus, and R. Kienberger. *Single-shot carrier-envelope phase measurement of few-cycle laser pulses*. *Nature Physics* **5**, 357–362 (2009).
- [167] A. M. Saylor, T. Rathje, W. Müller, C. Kürbis, K. Rühle, G. Stibenz, and G. G. Paulus. *Real-time pulse length measurement of few-cycle laser pulses using above-threshold ionization*. *Optics Express* **19**, 4464–4471 (2011).
- [168] T. Rathje, N. G. Johnson, M. Möller, F. Süßmann, D. Adolph, M. Kübel, R. Kienberger, M. F. Kling, G. G. Paulus, and A. M. Saylor. *Review of attosecond resolved measurement and control via carrier-envelope phase tagging with above-threshold ionization*. *Journal of Physics B: Atomic, Molecular and Optical Physics* **45**, 074003 (2012).
- [169] G. G. Paulus, F. Lindner, H. Walther, A. Baltuška, E. Goulielmakis, M. Lezius, and F. Krausz. *Measurement of the phase of few-cycle laser pulses*. *Physical Review Letters* **91**, 253004 (2003).
- [170] D. B. Milošević, G. G. Paulus, and W. Becker. *High-order above-threshold ionization with few-cycle pulse: a meter of the absolute phase*. *Optics Express* **11**, 1418–1429 (2003).
- [171] Kübel, K. J. Betsch, N. G. Johnson, U. Kleineberg, R. Moshhammer, J. Ullrich, G. G. Paulus, M. F. Kling, and B. Bergues. *Carrier-envelope-phase tagging in measurements with long acquisition times*. *New Journal of Physics* **14**, 093027 (2012).
- [172] S. H. Chew, A. Gliserin, J. Schmidt, H. Bian, S. Nobis, F. Schertz, M. Kübel, Y.-Y. Yang, B. Loitsch, T. Stettner, J. J. Finley, C. Späth, H. Ouacha, A. M. Azzeer, and U. Kleineberg. *Laser intensity effects in carrier-envelope phase-tagged time of flight-photoemission electron microscopy*. *Applied Physics B* **122**, 1–10 (2016).
- [173] A. M. Saylor, T. Rathje, W. Müller, K. Rühle, R. Kienberger, and G. G. Paulus. *Precise, real-time, every-single-shot, carrier-envelope phase measurement of ultrashort laser pulses*. *Optics Letters* **36**, 1–3 (2011).
- [174] P. Nordlander and E. Prodan. *Plasmon hybridization in nanoparticles near metallic surfaces*. *Nano Letters* **4**, 2209–2213 (2004).
- [175] M. Schmelzeisen, J. Austermann, and M. Kreiter. *Plasmon mediated confocal dark-field microscopy*. *Optics Express* **16**, 17826–17841 (2008).
- [176] A. Rueda, M. Stemmler, R. Bauer, K. Müllen, Y. Fogel, and M. Kreiter. *Optical resonances of gold nanoparticles on a gold surface: quantitative correlation of geometry and resonance wavelength*. *New Journal of Physics* **10**, 113001 (2008).
- [177] G. Frens. *Controlled nucleation for the regulation of the particle size in monodisperse gold suspensions*. *Nature Physical Science* **241**, 20–22 (1973).
- [178] S. H. Chew, K. Pearce, S. Nobis, C. Späth, A. Spreen, S. Radünz, Y. Yang, J. Schmidt, and U. Kleineberg. *Spatiotemporal characterization and control of lightfield nanolocalization on metallic nanostructures by nonlinear-PEEM*. In *SPIE Proceedings*. Vol. 8457, 84571C. Plasmonics: Metallic Nanostructures and Their Optical Properties X (2012).

- [179] K. Ueno and H. Misawa. *Spectral properties and electromagnetic field enhancement effects on nano-engineered metallic nanoparticles*. *Physical Chemistry Chemical Physics* **15**, 4093–4099 (2013).
- [180] F. Süßmann, S. L. Stebbings, S. Zherebtsov, S. H. Chew, M. I. Stockman, E. Rühl, U. Kleineberg, T. Fennel, and M. F. Kling. In *Attosecond Nanophysics. Attosecond and XUV Physics*, pp. 421–462 (Wiley-VCH Verlag GmbH & Co. KGaA, 2014).
- [181] B. Henke, E. Gullikson, and J. Davis. *X-ray interactions: photoabsorption, scattering, transmission, and reflection at $E = 50\text{--}30,000\text{ eV}$, $Z = 1\text{--}92$* . *Atomic Data and Nuclear Data Tables* **54**, 181–342 (1993).
- [182] M. Lorenzoni, A. Giugni, and B. Torre. *Oxidative and carbonaceous patterning of Si surface in an organic media by scanning probe lithography*. *Nanoscale Research Letters* **8**, 1–9 (2013).
- [183] W. Swiech, G. Fecher, C. Ziethen, O. Schmidt, G. Schönhense, K. Grzelakowski, C. M. Schneider, R. Frömter, H. Oepen, and J. Kirschner. *Recent progress in photoemission microscopy with emphasis on chemical and magnetic sensitivity*. *Journal of Electron Spectroscopy and Related Phenomena* **84**, 171–188 (1997).
- [184] W. Kuch, R. Frömter, J. Gilles, D. Hartmann, C. Ziethen, C. M. Schneider, G. Schönhense, W. Swiech, and J. Kirschner. *Element-selective magnetic imaging in exchange-coupled systems by magnetic photoemission microscopy*. *Surface Review and Letters* **5**, 1241–1248 (1998).
- [185] N. V. Smith, G. K. Wertheim, S. Hüfner, and M. M. Traum. *Photoemission spectra and band structures of d-band metals. IV. X-ray photoemission spectra and densities of states in Rh, Pd, Ag, Ir, Pt, and Au*. *Physical Review B* **10**, 3197–3206 (1974).
- [186] J. L. Alay, M. Fukuda, C. H. Bjorkman, K. Nakagawa, S. Yokoyama, S. Sasaki, and M. Hirose. *Determination of valence band alignment at ultrathin SiO_2 / Si interfaces by high-resolution X-ray photoelectron spectroscopy*. *Japanese Journal of Applied Physics* **34**, L653 (1995).
- [187] S. S. Nekrashevich and V. A. Gritsenko. *Electronic structure of silicon dioxide (a review)*. *Physics of the Solid State* **56**, 207–222 (2014).
- [188] N. M. Buckanie, J. Göhre, P. Zhou, D. von der Linde, M. H.-v. Hoegen, and F.-J. M. zu Heringdorf. *Space charge effects in photoemission electron microscopy using amplified femtosecond laser pulses*. *Journal of Physics: Condensed Matter* **21**, 314003 (2009).
- [189] S. Passlack, S. Mathias, O. Andreyev, D. Mittnacht, M. Aeschlimann, and M. Bauer. *Space charge effects in photoemission with a low repetition, high intensity femtosecond laser source*. *Journal of Applied Physics* **100**, 024912 (2006).
- [190] S. Collin, M. Merano, M. Gatri, S. Sonderegger, P. Renucci, J.-D. Ganière, and B. Deveaud. *Transverse and longitudinal space-charge-induced broadenings of ultrafast electron packets*. *Journal of Applied Physics* **98**, 094910 (2005).
- [191] A. Cabasse, G. Machinet, A. Dubrouil, E. Cormier, and E. Constant. *Optimization and phase matching of fiber-laser-driven high-order harmonic generation at high repetition rate*. *Optics Letters* **37**, 4618–4620 (2012).

- [192] M. Krebs, S. Hädrich, S. Demmler, J. Rothhardt, A. Zair, L. Chipperfield, J. Limpert, and A. Tünnermann. *Towards isolated attosecond pulses at megahertz repetition rates*. *Nature Photonics* **7**, 555–559 (2013).
- [193] I. Pupeza, S. Holzberger, T. Eidam, H. Carstens, D. Esser, J. Weitenberg, P. Rußbüldt, J. Rauschenberger, J. Limpert, T. Udem, A. Tünnermann, T. W. Hänsch, A. Apolonski, F. Krausz, and E. Fill. *Compact high-repetition-rate source of coherent 100 eV radiation*. *Nature Photonics* **7**, 608–612 (2013).
- [194] S. Hädrich, M. Krebs, A. Hoffmann, A. Klenke, J. Rothhardt, J. Limpert, and A. Tünnermann. *Exploring new avenues in high repetition rate table-top coherent extreme ultraviolet sources*. *Light: Science and Applications* **4**, e320 (2015).
- [195] A. Harth, C. Guo, Y.-C. Cheng, A. Losquin, M. Miranda, S. Mikaelsson, C. M. Heyl, O. Prochnow, J. Ahrens, U. Morgner, A. L’Huillier, and C. L. Arnold. *Compact 200 kHz HHG source driven by a few-cycle OPCPA*. *Journal of Optics* **20**, 014007 (2018).
- [196] J.-S. Huang, V. Callegari, P. Geisler, C. Brüning, J. Kern, J. C. Prangsma, X. Wu, T. Feichtner, J. Ziegler, P. Weinmann, M. Kamp, A. Forchel, P. Biagioni, U. Sennhauser, and B. Hecht. *Atomically flat single-crystalline gold nanostructures for plasmonic nanocircuitry*. *Nature Communications* **1**, 150 (2010).
- [197] W. P. Putnam. *Strong-field physics with ultrafast optical resonators*. PhD thesis, Massachusetts Institute of Technology (2015).
- [198] A. Apolonski, P. Dombi, G. G. Paulus, M. Kakehata, R. Holzwarth, T. Udem, C. Lemell, K. Torizuka, J. Burgdörfer, T. W. Hänsch, and F. Krausz. *Observation of light-phase-sensitive photoemission from a metal*. *Physical Review Letters* **92**, 073902 (2004).
- [199] S. Zherebtsov, T. Fennel, J. Plenge, E. Antonsson, I. Znakovskaya, A. Wirth, O. Herrwerth, F. Süßmann, C. Peltz, I. Ahmad, S. A. Trushin, V. Pervak, S. Karsch, M. J. J. Vrakking, B. Langer, et al. *Controlled near-field enhanced electron acceleration from dielectric nanospheres with intense few-cycle laser fields*. *Nature Physics* **7**, 656–662 (2011).
- [200] F. Süßmann, L. Seiffert, S. Zherebtsov, V. Mondes, J. Stierle, M. Arbeiter, J. Plenge, P. Rupp, C. Peltz, A. Kessel, S. A. Trushin, B. Ahn, D. Kim, C. Graf, E. Rühl, et al. *Field propagation-induced directionality of carrier-envelope phase-controlled photoemission from nanospheres*. *Nature Communications* **6**, 7944 (2015).
- [201] B. Ahn, J. Schötz, M. Kang, W. A. Okell, S. Mitra, B. Förg, S. Zherebtsov, F. Süßmann, C. Burger, M. Kübel, C. Liu, A. Wirth, E. D. Fabrizio, H. Yanagisawa, D. Kim, et al. *Attosecond-controlled photoemission from metal nanowire tips in the few-electron regime*. *APL Photonics* **2**, 036104 (2017).
- [202] J. Passig, S. Zherebtsov, R. Irsig, M. Arbeiter, C. Peltz, S. Göde, S. Skruszewicz, K.-H. Meiwes-Broer, J. Tiggesbäumker, M. F. Kling, and T. Fennel. *Nanoplasmonic electron acceleration by attosecond-controlled forward rescattering in silver clusters*. *Nature Communications* **8**, 1181 (2017).

- [203] C. Gong, J. Jiang, C. Li, L. Song, Z. Zeng, Y. Zheng, J. Miao, X. Ge, Y. Deng, R. Li, and Z. Xu. *Observation of CEP effect via filamentation in transparent solids*. *Optics Express* **21**, 24120–24128 (2013).
- [204] T. Paasch-Colberg, A. Schiffrin, N. Karpowicz, S. Kruchinin, S. Özge, S. Keiber, O. Razskazovskaya, S. Mühlbrandt, A. Alnaser, M. Kübel, V. Apalkov, D. Gerster, J. Reichert, T. Wittmann, J. V. Barth, et al. *Solid-state light-phase detector*. *Nature Photonics* **8**, 214–218 (2014).
- [205] H. Zeng. In *Ultrafast Nonlinear Optics. Advances in Nonlinear Optics*, Chapter: 3, pp. 191–226. Edited by X. Chen (De Gruyter, Berlin, Munich, Boston, 2015).
- [206] F. O. Kirchner, A. Gliserin, F. Krausz, and P. Baum. *Laser streaking of free electrons at 25 keV*. *Nature Photonics* **8**, 52 (2013).
- [207] W. S. M. Werner, K. Glantschnig, and C. Ambrosch-Draxl. *Optical constants and inelastic electron-scattering data for 17 elemental metals*. *Journal of Physical and Chemical Reference Data* **38**, 1013–1092 (2009).
- [208] M. Merkel, M. Escher, J. Settemeyer, D. Funnemann, A. Oelsner, C. Ziethen, O. Schmidt, M. Klais, and G. Schönhense. *Microspectroscopy and spectromicroscopy with photoemission electron microscopy using a new kind of imaging energy filter*. *Surface Science* **480**, 196–202 (2001).
- [209] M. Kotsugi, W. Kuch, F. Offi, L. I. Chelaru, and J. Kirschner. *Microspectroscopic two-dimensional Fermi surface mapping using a photoelectron emission microscope*. *Review of Scientific Instruments* **74**, 2754–2758 (2003).
- [210] O. Benka and P. Zeppenfeld. *Secondary electron images obtained with a standard photoelectron emission microscope set-up*. *Journal of Physics: Condensed Matter* **17**, S1311 (2005).
- [211] *Instruction Manual: IEF for FOCUS PEEM*. Omicron NanoTechnology GmbH / FOCUS GmbH. (2012).
- [212] *Delayline Detector DLD 3636 Manual*. Surface Concept. (2012).
- [213] J. Schmidt. *Development of an advanced 10 kHz high harmonic source and its application to angle- and phase-resolved photoelectron streaking spectroscopy*. PhD thesis, Ludwig Maximilian University of Munich (2017).
- [214] G. Wachter, C. Lemell, J. Burgdörfer, M. Schenk, M. Krüger, and P. Hommelhoff. *Electron rescattering at metal nanotips induced by ultrashort laser pulses*. *Physical Review B* **86**, 035402 (2012).
- [215] D. B. Milošević, G. G. Paulus, D. Bauer, and W. Becker. *Above-threshold ionization by few-cycle pulses*. *Journal of Physics B: Atomic, Molecular and Optical Physics* **39**, R203 (2006).
- [216] G. L. Yudin and M. Y. Ivanov. *Nonadiabatic tunnel ionization: looking inside a laser cycle*. *Physical Review A* **64**, 013409 (2001).
- [217] M. Krüger, M. Schenk, P. Hommelhoff, G. Wachter, C. Lemell, and J. Burgdörfer. *Interaction of ultrashort laser pulses with metal nanotips: a model system for strong-field phenomena*. *New Journal of Physics* **14**, 085019 (2012).

- [218] W. Becker, A. Lohr, and M. Kleber. *Effects of rescattering on above-threshold ionization*. *Journal of Physics B: Atomic, Molecular and Optical Physics* **27**, L325 (1994).
- [219] C. Lemell, X.-M. Tong, F. Krausz, and J. Burgdörfer. *Electron emission from metal surfaces by ultrashort pulses: determination of the carrier-envelope phase*. *Physical Review Letters* **90**, 076403 (2003).
- [220] M. Busuladžić, A. Gazibegović-Busuladžić, and D. B. Milošević. *High-order above-threshold ionization in a laser field: Influence of the ionization potential on the high-energy cutoff*. *Laser Physics* **16**, 289–293 (2006).
- [221] S. Thomas, M. Krüger, M. Förster, M. Schenk, and P. Hommelhoff. *Probing of optical near-fields by electron rescattering on the 1 nm scale*. *Nano Letters* **13**, 4790–4794 (2013).
- [222] M. Krüger, S. Thomas, M. Förster, and P. Hommelhoff. *Self-probing of metal nanotips by rescattered electrons reveals the nano-optical near-field*. *Journal of Physics B: Atomic, Molecular and Optical Physics* **47**, 124022 (2014).
- [223] P. Rácz, Z. Pápa, I. Márton, J. Budai, P. Wróbel, T. Stefaniuk, C. Prietl, J. R. Krenn, and P. Dombi. *Measurement of nanoplasmonic field enhancement with ultrafast photoemission*. *Nano Letters* **17**, 1181–1186 (2017).
- [224] H. Yanagisawa, S. Schnepf, C. Hafner, M. Hengsberger, D. E. Kim, M. F. Kling, A. Landsman, L. Gallmann, and J. Osterwalder. *Delayed electron emission in strong-field driven tunnelling from a metallic nanotip in the multi-electron regime*. *Scientific Reports* **6**, 35877 (2016).
- [225] J. Rodriguez-Fernandez, A. M. Funston, J. Perez-Juste, R. A. Alvarez-Puebla, L. M. Liz-Marzan, and P. Mulvaney. *The effect of surface roughness on the plasmonic response of individual sub-micron gold spheres*. *Physical Chemistry Chemical Physics* **11**, 5909–5914 (2009).
- [226] M. D’Acunto, F. Fuso, R. Micheletto, M. Naruse, F. Tantussi, and M. Allegrini. *Near-field surface plasmon field enhancement induced by rippled surfaces*. *Journal of Nanotechnology* **8**, 956–967 (2017).
- [227] A. Harth, C. Guo, E. Mårzell, A. Losquin, R. Svärd, E. Lorek, S. Lehmann, M. Miranda, K. A. Dick, P. Rudawski, C. M. Heyl, E. W. Larsen, J. Ahrens, O. Prochnow, T. Binhammer, et al. *Few-cycle high-repetition rate OPCPA for multiphoton PEEM towards Atto-PEEM*. In *International Conference on Ultrafast Phenomena*, UTu2B.4 (2016).
- [228] F. J. Furch, A. Giree, F. Morales, A. Anderson, Y. Wang, C. P. Schulz, and M. J. J. Vrakking. *Close to transform-limited, few-cycle 12 μ J pulses at 400 kHz for applications in ultrafast spectroscopy*. *Optics Express* **24**, 19293–19310 (2016).
- [229] X. Zhang, E. Schneider, G. Taft, H. Kapteyn, M. Murnane, and S. Backus. *Multi-microjoule, MHz repetition rate Ti:sapphire ultrafast regenerative amplifier system*. *Optics Express* **20**, 7015–7021 (2012).

- [230] R. Tromp, J. Hannon, A. Ellis, W. Wan, A. Berghaus, and O. Schaff. *A new aberration-corrected, energy-filtered LEEM/PEEM instrument. I. Principles and design.* *Ultramicroscopy* **110**, 852–861 (2010).
- [231] A. Alnaser, M. Kübel, R. Siemering, B. Bergues, N. G. Kling, K. Betsch, Y. Deng, J. Schmidt, Z. Alahmed, A. Azzeer, J. Ullrich, I. Ben-Itzhak, R. Moshhammer, U. Kleineberg, F. Krausz, et al. *Subfemtosecond steering of hydrocarbon deprotonation through superposition of vibrational modes.* *Nature Communications* **5**, 3800 (2014).
- [232] P. Rácz, S. E. Irvine, M. Lenner, A. Mitrofanov, A. Baltuška, A. Y. Elezzabi, and P. Dombi. *Strong-field plasmonic electron acceleration with few-cycle, phase-stabilized laser pulses.* *Applied Physics Letters* **98**, 111116 (2011).

Acknowledgments

This thesis would not have been accomplished without the contribution and the support from many people. First and foremost, I would like to thank my supervisor, Ulf Kleineberg, for giving me the opportunity to work in his group and on this challenging and yet exciting PhD topic. You have always been open and supportive to my ideas and suggestions regarding my projects and provided guidance. Most importantly, I am grateful for the freedom you gave me to work independently and take responsibilities in my research including the supervision of several Bachelor's and Master's students, which I enjoyed and benefited a lot from. Moreover, you always encouraged your students to attend local and international conferences by providing financial support, at which I could actively present my work and learn from numerous specialists in this field. Many thanks to Ferenc Krausz for providing an excellent working atmosphere, great research facilities as well as leading expertise in his Laboratory for Attosecond Physics; this added a unique and invaluable experience to my scientific career. I would also like to thank Jörg Schreiber for kindly reviewing my thesis.

My sincere appreciation goes out to Jürgen Schmidt for being the best colleague and friend, because you have been very supportive in various areas, both scientifically and personally. Your broad knowledge in laser physics and your work performance with meticulous care have taught me to pursue excellence. I must also acknowledge your great work as the main person who set up the whole 10 kHz XUV beamline in our laboratory. It was a great pleasure to have Sebastian Nobis, my favorite Bachelor's and later Master's student, working closely with me for the short 1.8 years. Thank you very much for your good cooperation and all the assistance. I also want to thank my group members: Kellie Pearce, Stephan Heinrich, Alexander Guggenmos, Huaihai Pan, Junwen Zou, Christian Späth, Michael Hofstetter, Stephan Radünz, Huanglei Bian, Jingquan Lin, Anika Spreen, Jeryl Tan, Ahsan Sabbir, Stefan Drexel and David Kronmüller. I truly appreciate the good time we have shared together and thank you for your support. Thanks also to Matthias Kübel, Hui Li, Sergey

Zherebtsov, Johannes Schötz, Nora Kling and Kelsie Betsch for sharing helpful advice on the phase tagging technique.

I am indebted to a number of people at the AS-5 beamline during the atto-PEEM campaign for their great teamwork. First, special thanks to Matthias Kling for demonstrating excellent leadership and for the fruitful discussions. I am deeply thankful to Frederik Süßmann for his outstanding collaboration as well as support on the laser alignment. Furthermore, I thank Adrian Wirth, Sergey Zherebtsov, Simon Watson, Sergey Trushin and James Kapaldo for their great effort in designing and implementing the AS-5 beamline. I absolutely enjoyed the company of Shao-Wei Chou, Annkatrin Sommer, Martin Schultze, Elisabeth Botschafter, Julia Mikhailova, Elisabeth Magerl, Tran Trung Luu, Xiaotao Geng, Minjie Zhan, Qingcao Liu, Guangjin Ma, Markus Fieß, Günther Leschhorn, Simon Holzner, Michael Jobst, Irina Znakovskaya, Christoph Skrobol, Patrick Heissler, Hanieh Fattahi, Nicholas Karpowicz, Yun Pei Deng, Wolfgang Schweinberger, Wolfram Helml and Stefan Neppl, particularly during the overnight measurements. Thank you also for all kinds of help you have given. I am very grateful to Adrian Cavalieri and Ralph Ernstorfer for first showing me how to troubleshoot vacuum leaks when I was new to vacuum technology. My thanks go also to Adrian Cavalieri for his helpful advice on electron count weighting in the ToF calibration. I also appreciate the initial effort Adrian Wirth and Jingquan Lin put into designing and manufacturing the PEEM chamber. Cordial thanks to Elisabeth Botschafter, Elisabeth Magerl and Adrian Wirth for being so helpful and patient in guiding me on the design of the HHG chamber and beamline.

People from the group of Martin Aeschlimann including Martin himself, Christian Schneider, Pascal Melchior, Cristian González and Michael Hartelt have generously helped me regarding PEEM. Thank you for sharing your profound expertise in PEEM and the interesting discussions at conferences or via email. Thanks to Anders Mikkelsen and Erik Mårsell for giving useful comments on the chromatic aberration in PEEM using attosecond XUV pulses. Many times Peter Baum and his group members (Alexander Gliserin, Bo-Han Chen, Friedrich Kirchner, Stefan Lahme, Thomas Ganz, Matthew Walbran, Waldemar Schneider, Yuya Morimoto and Andrey Ryabov) were willing to lend me their optics for a smooth experiment and I am definitely grateful for that. I would like to express my sincere appreciation to Peter Hommelhoff and Michael Förster for providing tungsten nanotips as well as to Michael Krüger, Dominik Ehberger and Catherine Kealhofer for very useful hints about handling nanotips. Various experimental samples were kindly provided by Christian Späth, Anika Spreen, Florian Schertz, Quan Sun, Han Yu, Hiroaki Misawa, Enno Krauss, Peter Geisler, Bert Hecht and Xiaoqing Zhou to whom I am thankful to.

Tokens of gratitude go to Seungchul Kim for your kind invitation to POSTECH to present my work and stimulating discussions about plasmonic nanostructures, Yingying Yang for helping on the numerical simulations and Peter Dombi for informative discussion. Thanks to Shaobo Fang for inviting me to Institute of Physics, Chinese Academy of Sciences. I enjoyed the fun discussion topics after my talk presentation. I must also acknowledge with great appreciation the good advice given by Andreas Oeslner and Pasqual Bernhard from Surface Concept GmbH regarding DLD operation and issues, especially Andreas who has impressed me so much with his professional replies with extensive explanations. Thanks a million to Nils Weber, Michael Merkel, Matthias Escher and Michael Schicketanz from FOCUS GmbH for the extensive technical support for our PEEM. Also thanks to all companies who have provided great support along with good instruments and equipments. Needless to say, I am indebted to the technicians from both LMU and MPQ workshops, in particular Rolf Oehm and his team, Alois Böswald, Anton Horn, Harald Hass, Dagmar Frischke, Johannes Wulz, Hans-Ulrich Friebel and Georg Brandl. Heartfelt thanks to Klaus Franke, Monika Wild, Katharina Adler, Susanne Endres, Ursula Schmitt, Oksana Zierer, Siegfried Herbst, Hans-Friedrich Wirth, Manfred Grote, Thorsten Naeser, Andreas Kramer and Felix Rauscher for administrative support. Furthermore, I want to thank the LMU folks such as Jinwei Zhang, Marcus Seidel, Olga Razskazovskaya, Ioachim Pupeza, Meilin Zhou, Jianhui Bin, Wenjun Ma, Klaus Allinger, Lauryna Lötscher, Ivan Angelov, Vladimir Pervak, Oleg Pronin, Nathaniel Kajumba and Peter Hilz for their collegueship and helping hand.

My deepest appreciation to Alexander Gliserin who has inspired me greatly in doing science but at the same time shown me the world outside academia. Words cannot describe how much I have gained from your exceptional guidance in many ways. I would also like to thank you for your great contribution in our successful collaboration on the phase-tagged PEEM as well as LabVIEW support. You have earned my admiration and respect. I am very grateful to Michael Krüger, a true friend and outstanding colleague who I can turn to for questions about strong-field physics. You have encouraged me greatly with your strong faith in Him and genuine enthusiasm for physics. I will always remember my mentor, Jan Stark, whom I had the honor to learn from during my two-month stay at CERN prior to my PhD studies. You have taught me the basic skills from preparing a talk presentation to communicating effectively in a scientific community.

For unconditional support during times of joy and frustration, I want to thank my good friends, they are Kong Nam Yong, Jane Chang, Yi Hua Lam, Joy Kim, Yu-Pei Tseng, Hoon Guan Choong, Hui Ching Cham, Danqing Lu, David Zhong, Binh Schmidt, Dimitris Sikoutris and Grace Tan. And most of all, I thank my beloved family, Choong Fat, Elsie, Macy and Jacky Chew, Nancy Ang as well as

Nuofugeluode Jiazhu for your fervent prayers, love and care throughout this journey. From the bottom of my heart, thank you everyone who has supported me on all occasions but whose name has not been mentioned here.

*I will praise thee, O LORD, with my whole heart;
I will shew forth all thy marvelous works.*

Psalms 9:1